PHOTO-THERMAL APPLICATION OF A POLYDIMETHYLSILOXANE FOAM EMBEDDED WITH CARBON NANOPARTICLES FOR INTERFACIAL SOLAR WATER EVAPORATION

SHUZHE WANG

A THESIS SUBMITTED TO THE FACULTY OF GRADUATE STUDIES

IN PARTIAL FULFILMENT OF THE REQUIREMENTS FOR THE DEGREE OF

MASTER OF APPLIED SCIENCE

GRADUATE PROGRAM IN

MECHANICAL ENGINEERING

YORK UNIVERSITY

TORONTO, ONTARIO

JUNE 2019

© SHUZHE WANG, 2019

Abstract

Freshwater scarcity is one of world biggest challenges and needs to be addressed urgently. The composites of polydimethylsiloxane (PDMS) and carbon-based materials have attracted intensive research interests over the past several decades owing to its stretchable, non-toxic features which can be applied in various fields such as flexible energy harvesting and storage devices. In this work, carbon nanoparticle (CNP) doped PDMS composite foams with an open-porous structure were fabricated via a facile salt-leaching technique to achieve excellent photo-thermal properties for solar desalination applications. The effect of different foam parameters on the photo-thermal performance of the CNP/PDMS foams was investigated and demonstrated in this thesis. The results showed that the addition of a small amount of the CNP dopants significantly improved the light absorptivity of the PDMS foams to about 97 % over the broad solar spectrum while causing little impact on the inherent low thermal conductivity of the foams. A modification using polyvinyl alcohol endowed improved surface wettability of the composite foams to provide continuous water supply to the evaporative layer. An enhanced water evaporation rate of 1.26 $kg/m^2 \cdot h$ (30.24 mm /day) with an overall energy conversion efficiency of 81 % was achieved using a relatively low solar energy input of 850 W/m^2. The findings in this work offer key insight for the development of photothermal composite films with high absorptivity, floatability and optimal porosity and thermal properties for the next generation of solar harvesting and seawater desalination technologies.

Acknowledgements

I would like to express my gratitude to Dr. Paul O'Brien for giving me the opportunity to be part of the AM-SET team. He has been a great supervisor and mentor supporting my research work. Without his guidance and supervision, I would not have learned so much throughout the entire two years. My special thanks to Dr. Sunny Leung and his students for helping me with the thermal conductivity measurement, Dr. Pouya Rezai for providing the plasma cleanser, and Dr. Alidad Amirfazli and his students for their help with the contact angle measurement. I also appreciated the great assistance of Dr. Nazir Kherani and Sara Almenabawy from University of Toronto, for the optical characterization of the samples. I would also like to thank my committee members Dr. Roger Kempers and Dr. Rashid Bashir for their review and valuable comments to make this thesis better.

I am grateful for my team members for giving a hand whenever I needed it. And all my friends and colleagues in Mechanical Engineering, your intelligence and diligence inspired me a lot. I will always remember the wonderful times we spent together. My great appreciations to my mom and dad, Cuiyan Zhang and Junling Wang, for their invaluable encouragement and care through good times and bad. Thank you both for being my rock. I love you so much. Also, many thanks to Xueling Luo who has been an amazing friend, always lending me a sympathetic ear and giving advice.

Shuzhe Wang

Toronto, June 14th, 2019

Table of Contents

List of Tables

List of Figures

List of Symbols

a	Surface area (m^2)
I	Intensity of the simulated solar radiation (W/m^2)
Δm_n	Net weight loss of the water in the evaporation tests (g)
Δm_t	Total weight loss of the water in the evaporation tests (g)
t	Duration of the evaporation tests
T_b	Temperature of the water at the lower surface of the CNP/PDMS samples (^oC)
T_f	Temperature of the photo-thermal film in the numerical model (K)
T_l	Temperature of the bulk of water (^oC)
T_t	Temperature of the top surface of the CNP/PDMS samples (^oC)
η	Overall energy conversion efficiency
ρ	Density (g/cm^3)
τ	Thickness of CNP/PDMS samples (mm)
ϵ	Theoretical porosity of the CNP/PDMS foams

List of Acronyms

ACA	Advancing contact angle
NP	Nanoparticle
BWRO	Brackish water reverse osmosis
CA	Contact angle
CAM	Citric acid monohydrate
CNP	Carbon nanoparticle
CNT	Carbon nanotube
DI water	De-ionized water
ED	Electrodialysis
GO	Graphene oxide
IR	Infrared
LSPR	Local surface plasmon resonance
MED	Multiple effect distillation
MSF	Multistage flash distillation
MWCNT	Multiwall carbon nanotube
RCA	Receding contact angle
rGO	Reduced graphene oxide
RO	Reverse osmosis
SEM	Scanning electron microscopy
SWCNT	Single-walled carbon nanotube
SWRO	Seawater reverse osmosis

TC	Thermocouple
TDS	Total dissolved salt
VC	Vapor compression
WCA	Water contact angle

1. Introduction

Living on an overpopulated planet, human society has been struggling with resource poverty and environment deterioration, among which the lack of freshwater is a most vital challenge.

1.1. World water status

Freshwater is one of the key elements for most activities happening on the planet from the basic functioning of tiny biological cells to the development of the entire human society. However, the reservation of water resources has been overlooked for too long and we finally stepped into the corner where inadequate access to clean water has become a big challenge since the late 1980s [1]. Based on global water footprint investigation and assessment, International Water Management (IWMI) announced that around 2.8 billion people already resided in areas of potential water scarcity in 2013 considering monthly variability, and this figure reached 3.6 billion (about 50 % of the population) five years later. Yet the number of people being affected is projected to continuously increase to 4.8 – 5.7 billion by the year 2050, half of whom will live under the threats of severe water shortage [2]–[4].

The endangered freshwater status does not only influence potable water and daily use but is also reflected in the declined capability for food production. The fact is, although not realized by the majority, almost 800 million people were already reported to starve in 2017 Still the world population is prescribed to increase up to a peak of around 10 billion by 2090, and experts are highly concerned about the competence of the planet to support such a sizeable demand [5]–[7].

1.1.1. Water scarcity assessment

Are we really in the situation of water scarcity? Restricted by a lack of knowledge, most people are likely to be biased and make their own estimation based merely on drinking water availability, which is the most intuitive information to them. Generally, water scarcity can be described as a mismatch between the huge demand and inadequate supply in terms of quantity and/or quality [1]. Although it is widely accepted that the world is currently and will be under a water crisis for a long time, it has been a challenge to quantify this status due to the complexity of the causes. A variety of models have been developed in water accounting and auditing to demonstrate water status and provide future projections [8]–[11].

One of the earliest assessments is the Falkenmark indicator, also called water stress index (WSI), calculated using population and the volume of available blue water (surface water and groundwater) within a given district [12], [13]. Countries are considered to be water-stressed when water availability is lower than 1,700 m^3 per year per person and will experience "scarcity" and "absolute scarcity" as the availability drops below the 1,000 and 500 m^3 per year per person thresholds, respectively. As a rough estimation based on the supply-side data [1], WSI is a pioneer indicator that provides for a quick grasp of the water resource state and is still widely used nowadays [14], [15]. A modified indicator is the criticality ratio that integrates demand-driven shortage into the model by water withdrawal analysis [16], [17]. However, these classic approaches are still considered to be insufficient because of their oversimplification.

To achieve a better comprehension of the water scarcity problem, continuous efforts have been made to incorporate more interdisciplinary elements, especially socio-economic factors including water management, institutional capability for providing water services and related policies, which are gradually combined into global water shortage analysis to provide practical tools for policy

and decision makers [18]–[20]. IWMI, for example, introduced the concept of physical and economic water scarcity in 1998 considering the adaptive capacity of a society in terms of infrastructure development and water planning at a country level and these concepts have been widely adopted since then. In this model countries that are unable to fulfill the estimated water demands, even if all the potential technological and strategical advances were to be implemented, are classified as being part of the "physical water scarcity" category, while countries that fail to make use of sufficient water resources due to reasons including under-invested infrastructure are classified into the "economic water scarcity" category [21]. A couple of years later, Sullivan et al. accounted for water sanitation in addition to socio-economic variables and formulated a water poverty index (WPI) [22], [23]. WPI also brings the assessment down to a household and community scale and is widely accepted as one of the most holistic measurement nowadays [24].

There are still a large number of metrics and analytical tools besides the main methods mentioned above [2], [25]–[27]. Consequently, more factors are carefully weighed and integrated into water scarcity modelling such as virtue water flow analysis, which focuses on water trading and long-distance transfer in addition to local resources [14], [28], [29], and analysis of green water (soil moisture in unsaturated zones) which provides for 90 % of the total agricultural demand and 60 % of the global food production [30]–[33]. Progress in analytical procedures are made with high spatial resolution considering geographic variability and diverse demands [34]–[36], as well as high temporal resolution, on a monthly rather than annual basis [37]–[39]. The results of water scarcity assessment depend highly on the models being employed and data collected from different levels, but most of the evaluations of the authority organizations (such as the United Nations, IWMI and the World Resource Institution) come to a similar conclusion that Asia, Africa and the west coastline of America are more threatened by water stress than other areas in the world. The

the UN investigation also indicates that the majority of physically scarce areas are located in the mid to low latitude zone of Asia and Africa, and the areas identified to have economic water scarcity is reported to be mostly Southeast Asia, Central Africa and South America in 2012 [40]. Furthermore, the latest version of the water scarcity map shows a noteworthy expansion and exacerbation of these areas in the last six years [41].

1.1.2. Driving factors

Driven by the collective effect of population growth, urbanization, industrialization, agriculture intensification, climate change, poverty, and even unbalanced power relations [4], [42], [43], an increasing number of regions are likely to confront severe groundwater overexploitation and depletion in their attempt to meet the ever-growing water demand and deliver reliable water services.

Natural water resources are never infinite – on the contrary, these resources are in fact quite limited. Freshwater resources represents around 3.3 % of the total water resources (1.2×10^7 km^3) on the planet, most of which is frozen in the glaciers and only 0.7 % can be utilized directly [44]. Groundwater is the main freshwater source representing 97 % of the accessible reserve worldwide, and thus has been expansively extracted in many districts, but one third of the world's most important groundwater systems were already on the verge of scarceness by 2015 [45]. In addition, great reductions in well-drilling costs, due to technological advancements, worsens this situation, resulting in an enormous groundwater withdrawal rate reaching a level three times as much as fifty years ago [46]. Global freshwater demand increased dramatically in the past century owing not only to population growth but also the combined effects of rapid urbanization, economic development and evolving consumption patterns. This pressure has continued without mitigation

at a steady rate of 1 % per year, projected to cause a 20 – 30 % escalation by 2050 compared with the present demand level [41], [47], [48].

The rapid development of human society contributes overwhelmingly to water scarcity by intensifying water usage without limitation. Despite some discrepancies, the general conclusions from various investigations on water consumption are unanimous as shown in Figure 1-1, which shows that the agriculture sector including irrigation, livestock and aquaculture is identified as the principal water consumer accounting for 69 % of the annual global freshwater withdrawal. Industry and municipality sectors take up 19 % and 12 %, respectively, according to the database of the Food and Agriculture Organization of the UN global information system on water resources and agricultural water management [41]. Predictions for the following decades suggest a slight shrinkage of the agricultural consumption rate as a result of rapidly growing industrial and domestic usage (a surge of 400 % and 130 % separately), although the agricultural sector will continue to withdraw the largest amount of water [49]–[51].

Another factor worth noting is climate change induced by the notorious global warming. The recent assessment by Intergovernmental Panel on Climate Change (IPCC) shows that the Earth

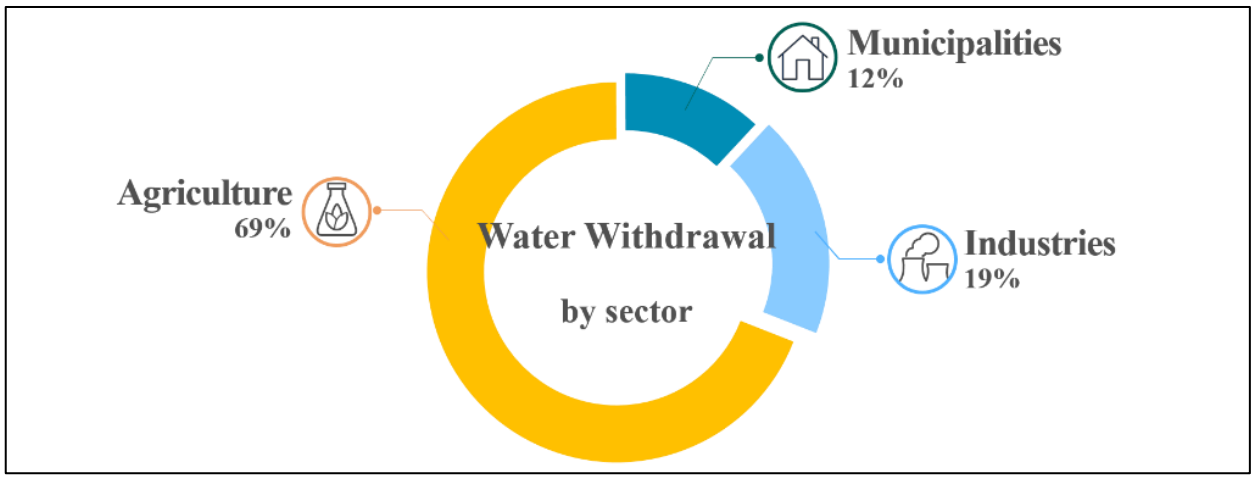

Figure 1-1 Worldwide annual water withdrawal by sector [41].

has experienced a rise of approximately 1 °C in its mean surface temperature relative to pre-industrial times (1850 – 1899) over the past century caused by greenhouse gas (GHG) emissions of human activities. Moreover, this number will reach 1.5 °C in 2040 with a current rate of growth of 0.2 ± 0.1 °C per decade [52]. Arctic melting and island dipping, which are predicted to occur when the human-induced global warming reaches 2.7 °C above the pre-industrial level, are expected to further amplify both regional and global water scarcity pressures in addition to that already expected from a 40 % population growth [5].

1.2. World energy status

Apart from the water crisis, the current generation is unfortunately faced with the additional dilemma of energy famine. With analogous root causes to freshwater scarcity, namely population-induced industrial expansion and urbanization, human society experienced an imbalance between energy provisions and consumption in the 1970s when significant petroleum shortage occurred in many industrial countries [53]. Many countries are now witnessing an enormous surge in energy demands in all end-use sectors including residential, commercial, industrial and transportation, especially in regions with rapid economic development. The estimations from the US Energy Information Administration (EIA) indicate that the growth of global energy consumption will grow by 49 % compared with the 2007 baseline in the next 20 years [54]. The industrial sector is currently leading the ascending trend, with an energy consumption increment from 211 quadrillion Btu[1] in 2011 to 276 quadrillion Btu in 2040 and will account for more than half of the total energy consumption by then.

[1] Btu: British thermal unit, the quantity of heat required to raise the temperature of one pound of liquid water by 1 °F at the temperature that water has its greatest density (approximately 39 °F) [341].

In terms of energy sources, conventional fossil fuel sources are still the major contributors, especially petroleum which will continue to be the top energy provider for the next 30 years. Taking the world's top economies for example, the US had to import 40 % of the petroleum it consumed in 2016 according to the International Energy Statistics database, and China used 4×10^9 metric tonnes of coal (nearly 30 times as much as its domestic reserve) in 2015 to support nationwide development in a parallel case [55]. Investigations also show a preference for natural gas over other fossil fuels because of the price reduction and recent crude oil shortage in many regions which will cause a natural gas production intensification all the way through 2050. The overuse of combustible fossil-fuel based energy sources not only causes irreversible damage to the natural topography of the Earth due to extraction activities, but also changes the atmospheric composition by emitting excessive CO_2 (39 % above the pre-industrial level in 2010), and therefore has accelerated global warming dramatically, which definitely aggravates the water status as discussed above [56]. Thus, insufficient energy and water are apparently related topics that merit close attention and urgent priority.

With the aim to attenuate the energy crisis, low-GHG energy sources have been explored on a global scale, which gives impetus to rapid scientific and technological progress. Nuclear energy was once a promising alternative for power generation, eliminating 64 billion tonnes of CO_2-equivalent GHG emissions that otherwise would have resulted from fossil fuels combustion since the commercialization of nuclear energy in the 1970s [57]. However, only a limited number of countries use this technique because of the international nuclear regulations, and notably, others might be further discouraged by the consequences of the famous nuclear accident in Japan [40]. Fortunately, the emergence of renewable energy has casted light on future energy solutions. In contrast to the non-ecofriendly nature of conventional energy sources, renewable energy in the

form of biomass, wind, direct solar, hydropower and geothermal energy is the key to a safe, clean and sustainable world to offer "benefits to a reduction of negative impacts of energy supply on the environment and human health as well as a large potential to mitigate climate change [58]" if employed properly to produce direct thermal/mechanical power, generate electricity, or be stored in secondary fuels and other chemicals.

The outcome of the international effort turns out to be encouraging. In 2008, about 12.9 % of the primary energy supply was produced from renewable energy sources [58]. For instance, the EIA declared that the gradual switch from carbon-intensive fossil fuels to zero-carbon renewables, principally wind and solar in the electric power sector, has payed off with a one fourth decline in domestic CO_2 concentration thus far, which could incite growing interest in more renewable energy adoption [59]. The alteration of the universal energy distribution towards renewables indicates a lessened reliance on conventional sources will be observed, specifically a joint share of petroleum and coal is projected to drop by 7 %, and the latter will be surpassed by natural gases in the same time frame (see Figure 1-2). Meanwhile a 56 % increase (taking up 129 out of the overall 734 quadrillion Btu consumption) in renewable sources by the 2040s will mark an exciting accomplishment towards the realization of the ambitious goal of holding atmospheric CO_2 concentrations below 440 ppm by 2050 [60].

1.3. Water – energy nexus and desalination

Neither energy shortage nor water stress is independent, as they are apparently related issues sharing the similar causes and comparable importance. Thus, the entire world needs to come up with an all-inclusive solution to overcome the unprecedented crises in solidarity. So far, many relevant protocols and agreements have been reached and adopted on a multinational scale to speed

up the process. The UN has announced the Sustainable Development Goals (SDGs) to emphasize universal and equitable access to clean water together with affordable and clean energy to call for immediate action against climate change (Goal 6, 7 and 13). Other organizations and institutions such as the World Water Council (WWC), International Water Association (IWA), International Energy Agency (IEA) and IPCC are also making efforts to monitor international data, generate reports and raise public awareness in the long journey of overcoming these challenges.

Covering most of the Earth's surface, seawater is a sustainable source of water, especially for ground and surface water in coastal areas. It has inherently high salinity (33,000 – 35,000 ppm on average), containing mainly sodium and chloride and minor elements such as calcium, sulphur, magnesium, potassium and bromide [61]. Only with desalination processes, the proper treatments to remove the excessive mineral components, can seawater reach the standard required for various human uses. According to the report of the International Desalination Association and Global Water Intelligence, the world cumulated desalination capacity increased by over 100 % (from 57.9

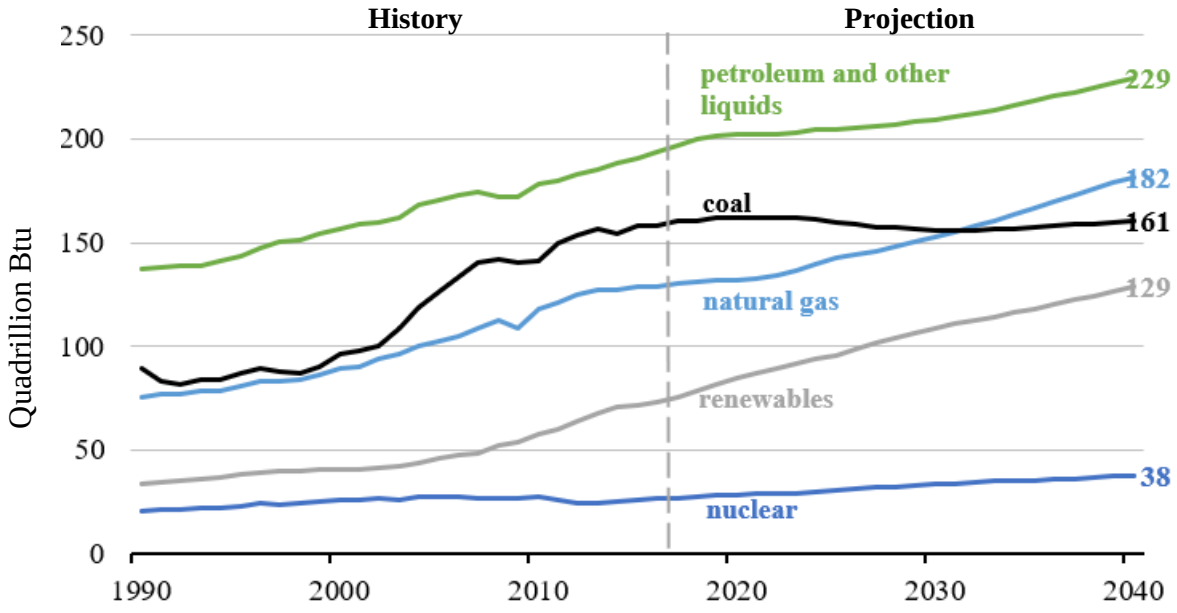

Figure 1-2 Historical and projected worldwide energy consumption by sources [59]. Source: U.S. Energy Information Administration (July 2018).

to 118 million m^3/day) during the period from 2009 – 2017, from which the huge future development potential of desalination can be foreseen [2], [62]. Desalination plants have been adopted in many places, for example the Middle East, Australia, Spain, Singapore and the United States, and 14 % of the global population is estimated to rely on desalinated water by 2025 [63], [64].

1.3.1. Traditional seawater desalination

According to separation mechanisms, traditional seawater and brackish water desalination can be classified roughly into two catalogs: thermal- and membrane-based processes. Thermal-based desalination technologies refer to those procedures where salty water is heated using direct thermal energy and freshwater can be collected following a scenario of evaporation and condensation. The most classic thermal methods are multistage flash distillation (MSF), multiple effect distillation (MED) and vapor compression (VC). These methods are normally suitable for large scale water treatment with high production quality and reliable long-time service (see Table 1-1) [65], [66]. The membrane-based process generally include seawater or brackish water reverse osmosis (SWRO/BWRO), electrodialysis (ED) and some filtration methods [67]. Most of these systems carry semipermeable membranes as the core unit that is driven by dynamic or electrical power to overcome osmotic pressure of the saline solution and let H_2O molecules (rather than other bigger molecules or ions) pass through the membranes freely [68], [69]. Nevertheless, the total dissolved salt (TDS) of the product is commonly up to 500 ppm, significantly higher than that of the thermal processes (also see Table 1-1).

Theoretically, around 0.77 kWh/m^3 of energy is the minimum required to desalinate salty water (33,000 ppm at 25 ^oC) based on the van't Hoff formula from a thermodynamic perspective [70].

Despite the relatively low product quality, membrane processes have become increasingly popular and gradually surpassed the thermal-based facilities, taking the main market share owing to less energy consumption (mostly less than 5 kWh/m^3) and a wide range of capacities, yet both types consume 5 – 26 times as much energy as the minimum leading to a universal mission to develop less energy-intensive approaches, a requirement on the path towards sustainability [66].

Table 1-1 Main operation data of conventional desalination units [66], [71]–[79].

Type	Typical Daily Capacity (m^3)	Equivalent Total Energy Consumption (kWh/m^3)	Product Water Quality (ppm)	Cost (USD/m^3)
MSF	50,000 – 70,000	19.58 – 23.5	≈10	0.56 – 1.75
MED	12,000 – 320,000	14.45 – 21.35	≈10	0.52 – 8
VC	1000 – 30,000	7 – 16.26	≈10	0.87 – 2.6
SWRO	~ 128,000	4 – 6	400 – 500	0.45 – 1.72
BWRO	~ 98,000	1.5 – 2.5	200 – 500	0.26 – 12.99
ED	~ 145,000	2.5 – 5.5	150 – 500	0.6 – 1.05

1.3.2. The integration of solar energy into desalination systems

To achieve the goal of providing reliable freshwater access to all with reduced GHG emissions and less impact on the environment, extensive integration of renewable energy in desalination industries is imperative. Many of the renewable energy technologies can be easily adapted to feed a centralized electric grid and delivered with modern energy transmission methods mostly for electricity generation, or designed as a standalone supply for both electricity and thermal/mechanical energy for the end user even in autonomous buildings thanks to their modular features and desirable flexibility [58]. In the renewable energy family, solar stands out and is considered to be one of the "holy grails" in the scientific field of the 21st century because of zero GHG emissions and inexhaustible availability [80]. The energy potential of solar irradiance

impinging on the Earth's surface per year is reported to be theoretically more than enough to satisfy the world's annual demand [58], [81]. Thus, solar energy appears to be a good match with the energy-intensive seawater desalting technologies. Fortunately, those areas mentioned previously suffering the most from water poverty such as Africa, Asia and south America are actually endowed with plenty of sunlight to support solar distillation according to the World Bank (red regions shown in Figure 1-3 [82]), encouraging massive research work on this solution to the ongoing crises.

In short, to lessen the pressure on the limited freshwater resources, seawater desalination is a promising approach to meet the growing water demand. Furthermore, by integrating the renewable solar energy into the existing desalination systems, the production of freshwater can be less energy intensive with lower GHG emissions. Solar desalination reflects a concept of water-energy nexus and is worth extensive development which will be discussed in detail in Chapter 2.

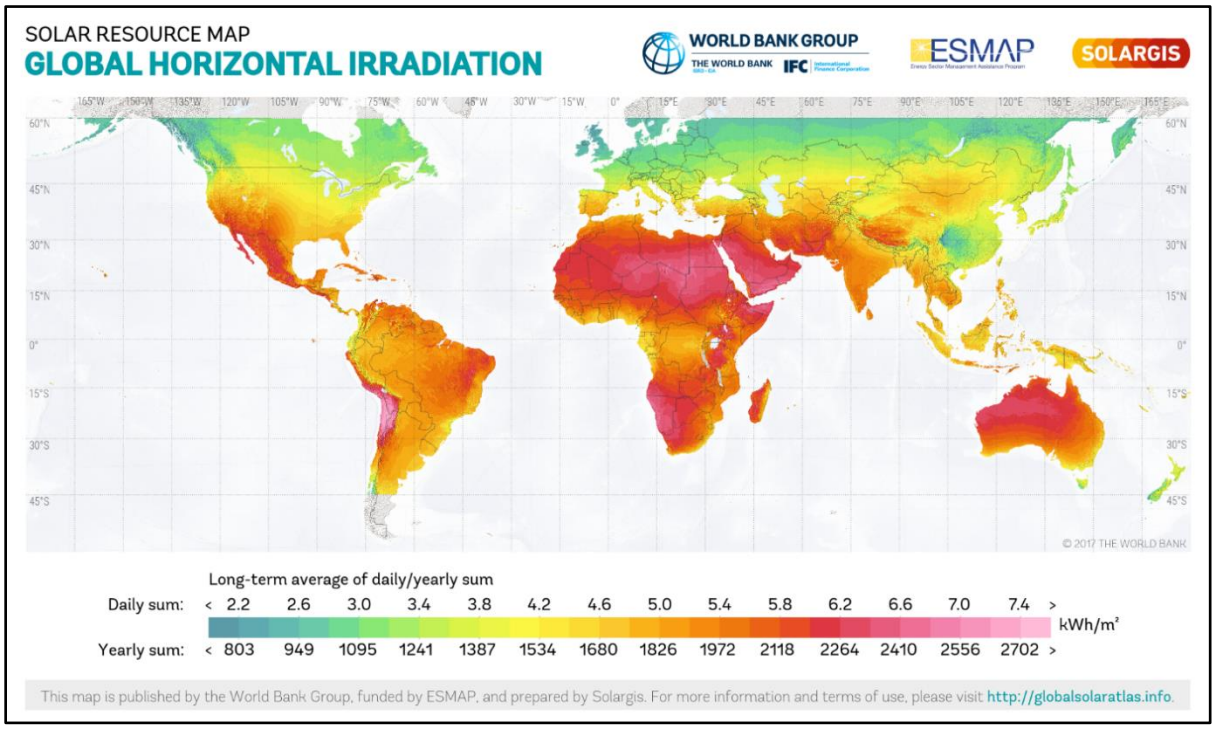

Figure 1-3 Global horizontal irradiation colormap [73], Copyright 2017. Reproduced with the permission from The World Bank, Solar resource data: Solargis.

2. Background and Literature Review

Solar desalination denotes a technique whereby the inexhaustible solar irradiance is used to evaporate water at a temperature below its boiling point through a direct or indirect manner to replace conventional energy sources used for seawater desalination [83]–[85]. Solar desalination is not a new concept, in fact it emerged as early as the 4th century B.C., and was firstly recorded in a document about perfume production in the 16th century [86], [87]. However, solar desalination did not arouse massive research passion until lately in an urgent reaction to the threats of energy and water shortage as discussed in Chapter 1. Nowadays the significance of solar-driven seawater desalination is better understood than ever before, which greatly motivates academic research and exertion towards scaling-up practical water supply service in the hope that this promising alternative will alleviate or even eliminate the heavy dependence on fossil resources.

2.1. Traditional solar desalination

The earliest solar desalination plants comprised a rather straightforward single-slope structure wherein salty water was fed into a reservoir and heated under natural sunlight. The generated vapor condensed onto a tilted transparent ceiling on top of the plant and the run-off was collected.

From a microscale perspective, the incoming solar irradiance increases the thermodynamic energy in liquid water and the intrinsic vibration of the hydrogen bonds between H_2O molecules is consequently intensified. If the vibration is significant enough to break the intermolecular connections, water molecules will be released into the gaseous phase as vapor. Otherwise the extra energy will be stored in the dynamic vibration of the water bonds and/or dissipated to the environment without causing water to evaporate. In the first case, the received solar energy is converted into the so-called “latent heat” as the evaporation process occurs, while in the other case

solar energy is accumulated in the system as “sensible heat” which merely causes a temperature rise in the liquid.

From this point of view, the primitive direct-heating approaches with different ceiling designs (single slope, double slope, V-shape and hemisphere, see Figure 2-1) ends up wasting a large portion of the absorbed solar-thermal energy to heat up the bulk water in a huge reservoir as opposed to generating steam [88], [89]. Hence, direct heating approaches exhibit a very limited overall efficiency (30 – 40 % for a single basin solar still) and low distillation output (roughly 2.8 – 7 L/m^2 per day for a typical single slope construction [90]–[96]). The performance can be slightly improved by blackening the basin and preheating the bulk water with the condensation energy released, but this technology is still more suitable for a household or small community and is not economically viable for large-scale commercialization [97].

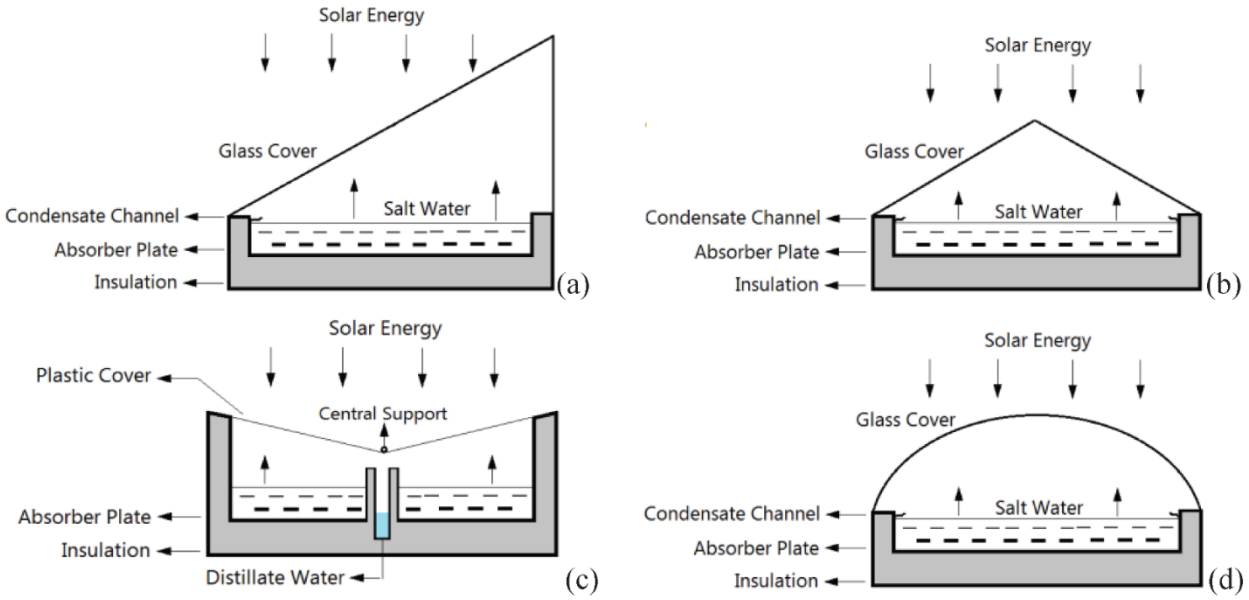

Figure 2-1 Common designs of traditional solar stills: (a) single-slope basin still, (b) double-slope basin still, (c) V-type solar still and (d) hemispherical type solar still [79], [80], Copyright 2015. Reproduced with Creative Commons Attribution 3.0 License.

For indirect solar distillation processes, solar harvesting modules are integrated into existing direct desalination systems. The collected solar energy can be concentrated and converted into heat for thermal-based desalination plants (MSF, MED and VC), or converted into electricity by a photovoltaic unit to power membrane-based processes such as RO [85], [87], [98], [99]. Even though both solar powered thermal and electric processes have proven to be beneficial to control the energy footprint, it is still difficult to completely substitute conventional fossil fuel-based power with solar as the primary energy source to support an entire system due to the technical restriction on photo-thermal/electrical energy conversion efficiencies and dependence on the uncertain climate. The commercially available silicon-based photovoltaic solar panels and cells, as an example, can only reach an efficiency lower than 30 %, apparently adding negative impact to the productivity of solar desalination systems [100].

2.2. Modification of solar desalination design and localized solar heating

To make better use of the abundant and clean solar energy, advanced technologies need to be developed indisputably to make desalination processes more energy efficient to achieve future sustainability. Many investigations have been reported in the literature, focusing on several factors to upgrade the efficiency of present-day solar distillation systems.

(1) Concentration of solar radiation

The energy carried by the natural solar irradiance at air mass 1.5 is ~ 1 kW/m^2 (1 sun), which is inadequate to vaporize water at a high rate, inspiring the idea to concentrate the incident light for an intensified power supply. Optical concentrators with different geometries such as parabolic trough/dish [101]–[105] and Fresnel lenses [106], [107] have been explored for their ability to focus sunlight onto solar receivers that utilize absorbed solar energy to evaporate water [108]. In

a study carried out in Egypt during summer by Omara *et al*., it was indicated that the employment of a parabolic dish solar concentrator increased the daily freshwater production rate with a notable upsurge of 244 % in comparison to a conventional single slope still [102]. Conversely, these concentrators also display drawbacks of manufacturing complexity and expensive cost.

(2) Improvement upon solar absorptivity and energy conversion

To capture more solar radiation, assistive photo-thermal materials, namely solar absorbers or receivers, with broadband solar absorptivity and outstanding solar-thermal transformation ability should be introduced into the desalting systems. Thermal energy is generated at, or within a small region close to the surface of the materials, which is defined as a "localized heating" phenomenon. Absorbers used for solar-driven water desalination fall into three main groups based on their position: those located near the bottom of the water being desalinated, those dispersed in the water being desalinated, and those located at the air-water interface (see Figure 2-2 [109]). Metals and semiconductors are commonly bottom-seated solar receivers because of their high density. When using these materials, a large portion of the incident solar irradiance is transferred to the entire reservoir, resulting in large sensible heat losses. By bringing their dimensions down to the micro- or nanoscale, these heavy materials can be suspended in water to function as volumetric receivers. Volumetric absorbers have been proven to be beneficial to enhance vaporization which will be further discussed in Sections 2.3.1 and 2.3.2, but it is challenging to find reliable dispersion methods and the solution to the potential pollution issues associated with these materials. For the third type of absorber, light-weight materials such as carbon are able to stay at the air-water interface and are thus called interfacial solar receivers. Interfacial solar receivers were reported to give superior overall evaporation efficiencies with little side-effects. A detailed review of interfacial solar receivers will be discussed in Section 2.3.3.

(3) Reduction of unnecessary losses

Except for the employment of advanced materials, it is of equal significance to optimize system parameters including basin size, proper insulation and pay attention to climatic factors such as ambient temperature since these affect the heat loss mechanisms [110]. For example, the efficiency of the system will drop dramatically in a reservoir of a larger volume [111] and details will be discussed in Chapter 3.

Among these concepts, points (2) and (3) were explored more in this work for the design, fabrication and evaluation of solar receivers to achieve efficient localized heat generation in water evaporation systems. To provide the relevant background information pertaining to point (2), recently reported photothermal materials used for enhanced solar desalination are reviewed in the next section.

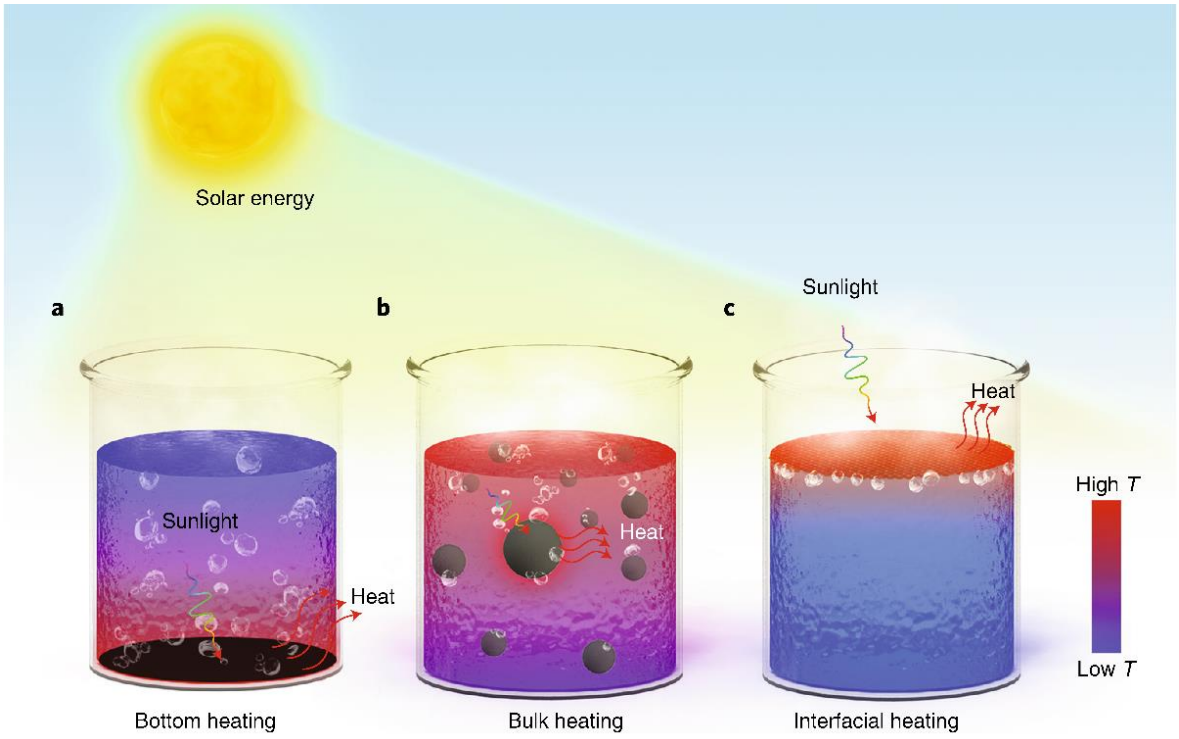

Figure 2-2 Illustration of three types of solar receivers (from left to right): bottom-seated, volumetric and interfacial [100], Copyright 2018. Reproduced with permission from SpringerNature.

2.3. Photo-thermal materials for localized heating

According to the description of Cao *et al.*, ideal solar receivers normally display "contrasting properties of high solar absorbance and low thermal emittance, which can be achieved through high reflectivity in the long-wavelength infrared region (2.5 – 25 μm)" [112]. In this regard, photo-thermal materials used in localized heating applications should meet the basic standards: highly absorptive over the broad solar spectrum, while being capable of producing and delivering thermal energy to a limited volume of the surrounding salty water. By manipulating morphologies, bulk structures and chemical components, various photo-thermal materials have been investigated for their performance of light trapping and heat generation in solar distillation with tailored properties to promote photo-thermal conversion efficiency and thereby system productivity [111], [113]–[115].

2.3.1. Metals

Localized surface plasmons (LSPs) refer to constrained charge oscillations which are mostly observed in metallic nanostructures or tiny clusters [116]. LSPs show intense absorption bands at one or more particular wavelengths due to the coherent interaction of the electrons in the conduction band with the electromagnetic field in the incident solar irradiance. This phenomenon is defined as local surface plasmon resonance (LSPR) and is highly tunable by altering the size, shape and assembly status of the metallic nanostructures [117]–[120]. Common strategies of expanding absorption bands include decreasing the shape symmetry and integrating voids in the structure [121]–[124].

Noble metals and their cermet, such as gold (Au) [125]–[131], silver (Ag) [132]–[134], aluminum and alumina [135]–[137], copper (Cu) and copper sulfide [138]–[140] and nitrides [141], [142] or

a combination of them, have been widely investigated as LSP materials for localized heat generation.

Au nanoparticles (AuNPs) are famous for strong resonant interactions with the visible-NIR (near infrared region) portion of the solar spectrum [143], which is the spectral region where solar energy is concentrated, and consequently AuNPs are exploited the most frequently. Jin *et al.*, for example, dispersed AuNPs with an average diameter of 20 nm in water, achieving a peak temperature of 100 ^{o}C within 90 s under 220 suns illumination [125]. This work reached a high level of solar-thermal conversion efficiency of 80.3 %, which is the ratio of the amount of thermal energy used for evaporation and the total incident solar energy but was rather demanding in the energy input.

In another case a delicate construction of mesoporous plasmonic nanoshells was prepared using an Ag/Au alloy by Zielinski *et al.* [124]. SiO_2 beads were used to mask Ag cores before the surface deposition of Au. After removing the beads and cores, Ag/Au nanoshells with pinholes were attained to enable fast vapor diffusion and heat transfer (see Figure 2-3). The shell thickness and pinhole size of the nanoshells were controllable by adjusting synthetic parameters. The best solar-

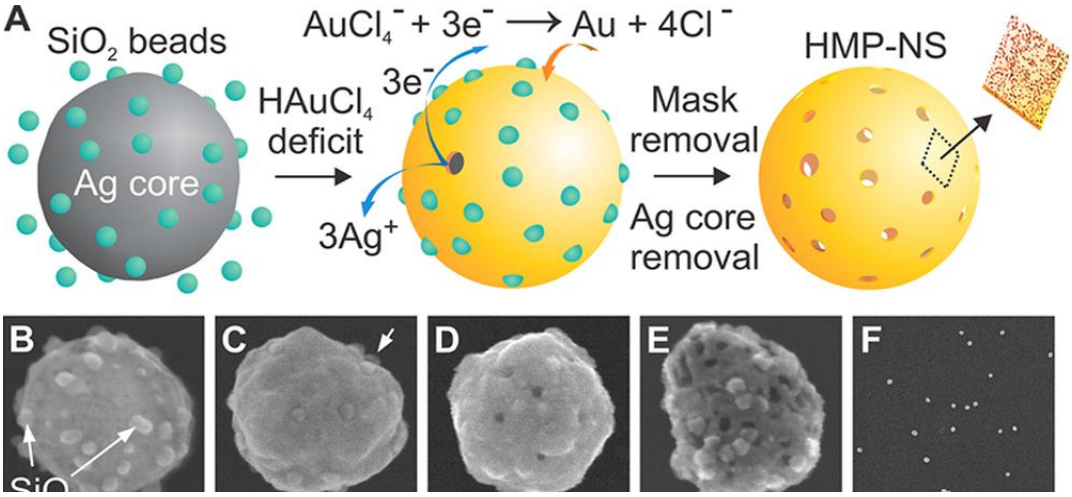

Figure 2-3 Schematic illustration of the fabrication process of the Ag/Au hollow mesoporous plasmonic and SEM micrographs showing the evolution of nanoparticle morphology during fabrication (scale bar: 1 μm) [115], Copyright 2016. Reproduced with permission from American Chemical Society.

to-vapor conversion efficiency achieved was 69 %, more than two times higher than that achieved with the common Au colloids.

Notably, in a very recent research report, a rarely used metallic compound, tungsten carbide was manufactured into a nano-array film which effectively reduced the light reflection at the water surface, and led to an outstanding solar-to-vapor efficiency of 90.8 % when tested with salty water at the rate of (1.06 ± 0.10) $kg/m^2 \cdot h$ [2] [144].

2.3.2. Semiconductors

Semiconductors are another important branch of solar-energy harvesting material that absorb photons carrying an amount of energy that is greater than their bandgap. Electrons in the valance band within semiconductors absorb incident electromagnetic waves and become excited and jump to conduction band states, initiating electron-hole pair generation and free charge carriers so that electrical or photo-thermal conversion of solar radiation occurs. The extent of light absorption can be governed by bandgap engineering such as the control of material dimensions and introduction of dopants [145], [146].

Titanium oxides, as typical semiconducting materials, have been studied for photo-thermal translation of their active responsive behavior in electromagnetic fields [147]–[149]. Wang *et al.* prepared black Ti_2O_3 nanoparticles with an ultra-narrow bandgap using a ball-milling process to introduce oxygen vacancies, which were proven to absorb ~ 92.5 % of the total energy across the entire solar spectrum [147]. After a vacuum deposition onto cellulose films, the floating samples showed hot spots on their surface under 5 kW/m^2 illumination reaching about 50 ^oC and an

[2] $kg/m^2 \cdot h$ = 24 mm/day.

evaporation rate of 5.03 kg/m^2·h was achieved. Meanwhile the bulk water beneath these floating films stayed cool with a temperature 23 ^{o}C lower than that of the films after 15 min of light exposure, suggesting effective thermal insulation was provided by the underlying cellulose membrane [150]. Zhu *et al*. synthesized an interesting self-assembled nanocage structure of black Titania offering strong internal scattering to trap light [149]. The nanocage film was able to produce water vapor with a solar-thermal efficiency of 70.9 % under 1 sun and showed a surface temperature of 80 ^{o}C, which is higher than most temperatures reported in the literature for 1 sun power input.

Other than Titania, Ishii *et al*. reported the preparation of a silicon nanofluid to improve the solar evaporation rate by 60 % compared with pure water with a concentration as low as 0.01 vol% using 0.8 kW/m^2 (0.8 sun) irradiation [151]. However, this method is still subjected to a difficult recycling problem, which is as a common drawback of volumetric solar receivers. Although the typical working temperature of solar desalination devices is below the boiling temperature (100 ^{o}C), future steam generation processes may require extreme high-temperature environments to improve desalination rates, especially those integrated with concentrating solar power modules. In this regard, a potential problem already pointed out by the thermoelectric industry, where a similar setup and operating conditions are engaged, is that the system will suffer from thermal aging of the materials [152]–[155]. To address this degradation issue, Kim *et al.* developed a spectrally selective coating (SSC) by creating silicon boride on the silicon surface using a molten salt-assisted reaction to prevent Si oxidation effectually in a harsh situation (850 ^{o}C in the air, see Figure 2-4) [156]. This structure also displayed a reduced reflectivity and superior absorptivity in the visible range compared to the primitive silicon NPs.

2.3.3. Carbon-based materials

Investigations of Carbon-based materials has gained a reputation as one of the cutting-edge research fields, and has become even more fascinating when nanotechnologies were introduced into this field. Carbon-based materials are now invasive options in almost every domain on account of their unique mechanical, electrical and photo-thermal features [157]–[162]. Specifically, with their robustness, low density, chemical stability, superior thermal and electrical conductivity, wide accessibility and ecofriendly trait, carbon-based materials offer clear advantages over the commonly used metals and semiconductors as receivers in solar desalination applications [163].

The diverse exploration of carbon-based materials for localized heating applications is summarized in the following categories: graphite/carbon black [164]–[167], graphene [168]–[172], graphene oxide (GO)/reduced graphene oxide (rGO) [173]–[179], singlewall/multiwall carbon nanotubes (SWCNTs, MWCNTs) [180]–[184], bio-based carbon materials [185]–[187], and other composites [188]–[197]. Two main carbon-based structures have been reported to be highly applicable for interfacial solar-driven desalination, namely 3D carbon aerogels/sponges [164],

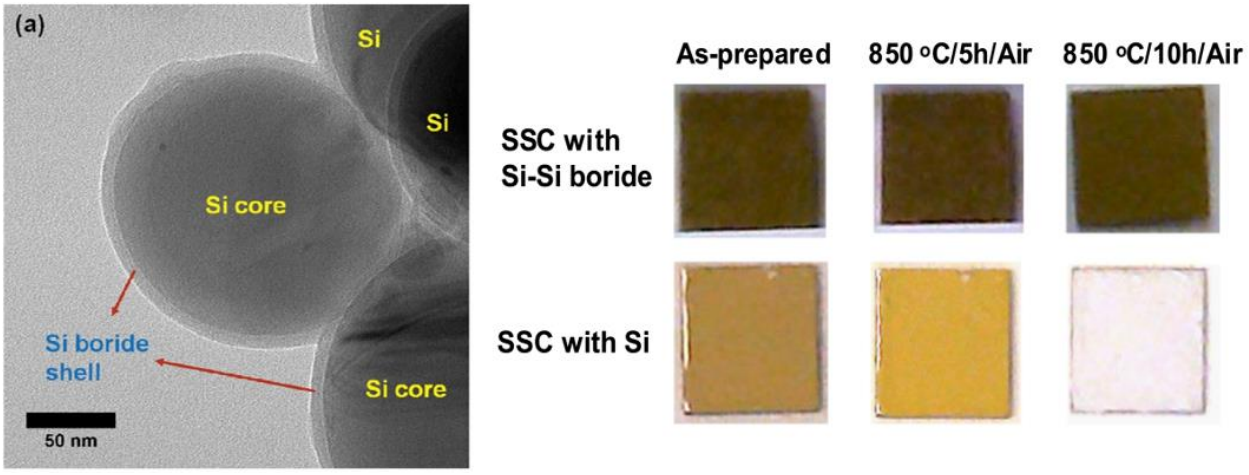

Figure 2-4 TEM image showing the 10 – 20 nm thick silicon boride shell on the surface of the silicon nanoparticle. surface color change of the spectrally selective coating (SSC) annealed at 850 °C for 10 h [147], Copyright 2014. Reproduced with permission from Elsevier.

[171], [172], [177], [179], [198] and 2D thin film structures [166]–[170], [174]–[176], [178], [181], [182], [184], [190]–[196], [199] because of their robustness and fabrication feasibility.

Carbon aerogels and sponges can be considered as a mixture of a photo-thermal part (carbon) and an insulating part (air voids). These carbon-based materials exhibit high solar absorptivity, low thermal conductivity, efficient water supply pathways and good floatability. Their 3D porous construction is thus capable of outstanding heat localization at the air-water interface due to the inherent resistance to convective heat loss to the water below. Fu *et al.* fabricated a hydrophilic rGO aerogel by a hydrothermal method and plasma treatment that induced an evaporation efficiency of 76.9 % under one sun radiation [179]. The hydrophilic modification helped pump small amounts of water constantly to the evaporative surface to avoid heating the water in the whole beaker. Similarly, Hu *et al.* modified a freeze-dried rGO aerogel using MWCNTs and sodium alginate, which improved its solar absorptivity from 82 % to 92 % and reduced its static water contact angle (WCA) from 115 ^{o} to 74 ^{o} [177]. An evaporation rate of 1.622 kg/m^2·h was achieved, ranking first to date in the published works for testing with 1 sun illumination. Y. Ito *et al.* found that a nitrogen doped nano-porous graphene structure at the air-water interface could be heated to 100 ^{o}C under concentrated solar irradiance (9 suns) with the bulk water remaining at 35 ^{o}C, converting 80 % of the received solar energy to the latent heat of water [169]. Instead of artificial synthesis, natural 3D carbon-based structures have also been investigated [185]–[187]. For example, carbonized mushrooms were used directly due to their stem-pileus configuration and interior pores [185]. Wood was employed as a matrix to benefit from its hierarchical micro- and nanochannels for water transport and demonstrated an 81 % efficiency when CNTs were coated on their top surface [186].

Carbon-based 2D thin films have also been extensively studied. Unlike the all-in-one design of aerogels, thin films with thicknesses on the order of millimeter scale or even thinner are usually combined with an insulation layer, normally polymers, to confine heat losses. Li and co-workers added a polystyrene foam (thermal conductivity 0.04 W/m·K) at the bottom of a black GO film as an insulation structure to realize heat localization around the film. A cellulose paper was wrapped over the foam to provide capillary pumping for water replenishment [174]. Another relatively complicated design was composed of a hydrophilic carbon black/polyacrylonitrile composite layer and a hydrophobic polyvinylidene fluoride layer carrying aligned vertical channels. Both layers were made of nanofibers to build a highly porous material, and exhibited an energy conversion efficiency of 82 % in solar evaporation tests [196]. Samples comprised of carbon-based ink coated on top of paper, polypropylene and wood substrates using atomic layer deposition were also attested to be rather effective interfacial solar absorbers [170].

Based on this investigation of a wide range of photo-thermal materials, carbon-based material, specifically carbon nanoparticle (CNP) was selected in this study to act as the solar receiver due to its minimal environmental impact. To obtain an interfacial structure, CNP was incorporated with a polymer substrate to achieve floatability. The polymer used here was polydimethylsiloxane (PDMS), which is discussed in the next section below.

2.4. Polydimethylsiloxane (PDMS)

Polydimethylsiloxane (PDMS) is a type of organosilicon polymer and can be described using the formula $CH_3[Si(CH_3)_2O]_nSi(CH_3)_3$ wherein n represents the number of monomer repetitions [200]. This silicon-based organic material is elastic, optically transparent, chemically inert, thermally stable, biocompatible and easy to manipulate, and most of these benefits are the results of the

strong chemical bonding between silicon and oxygen atoms in the siloxane backbone [201]. The past two decades have witnessed the rapid development in academic and industrial applications to use pristine PDMS as well as its derivatives with versatile modification in structure and chemical component.

2.4.1. Pristine PDMS

PDMS has been the most favored material as a substitute for conventional silicon in microchip fabrication for the prevailing study of microelectromechanical systems (MEMS) and microfluidic devices. Through cast molding and soft lithography of PDMS, these devices can be produced without cutting-edge tools which reduces the costs significantly yet with a decent quality down to submicron or nanometer scales [202], [203].

Another main application of pristine PDMS makes use of its unique surface properties. Due to the inertness and stability of its polymer surface, PDMS shows high potential to be used as a protective coating against flame, environmental contaminations, and corrosion/oxidation [204]–[209]. The silanol groups in PDMS tend to form metallo-siloxane (Si-O-metal) covalent bonds with metallic surfaces to achieve robust adhesion at the interface, making it attractive in corrosion control, especially for, but not restricted to, metals and alloys [210]–[213]. Considering its inherent hydrophobicity, PDMS can be also used as a self-cleaning and anti-icing agent for buildings and car surfaces [214]–[217], and anti-reflection coatings if integrated with optical gridding and patterning [218]–[220]. Remarkably, the hydrophobicity also endows PDMS with floatability on water even though it has a density which is slightly higher (1.03 g/cm^3). However, this floating behavior is unstable and PDMS will sink after several hours' contact with water which does not meet the requirement of air-water interfacial heating applications. The solution to address the

floating issue is to reduce the density of the polymer and this will be discussed subsequently in Section 2.4.3.

2.4.2. PDMS composites – component modification

Exploration of composites is a major branch in material science nowadays, aiming to take advantage of each component in a singe structure and create new properties and therefore broader applicability. A variety of modification strategies of PDMS have also been developed for this purpose, which consist of mainly two types: bulk modification (solution mixing, filtration, percolation [221], [222]) and surface modification (coating, printing, infusion, grafting [223]–[226]) techniques. The most commonly studied compound elements are low-dimensional carbon-based (graphite [227], graphene [228], rGO [229], CNTs [226], [230], [231], carbon fibres [232], carbon black [233], [234]) and metallic materials (Ag [235]–[237], Au [238]–[241]) which are often used to introduce electronic and capacitive features to elastic PDMS substrates [242].

One of the biggest markets for carbon/PDMS and metal/PDMS composites turns out to be medical diagnostics, specifically for human-machine interfaces in physiological data acquisition devices. For example these composite are competitive candidates for dry surface electrodes which are safe and reliable for long-term monitoring in ubiquitous health care applications [243]–[247]. Moreover, another important application of PDMS-based composites is more relevant to their mechanical stretchability [248]. Relative changes in resistance or capacitance of the materials will be induced by the structural deformation of the PDMS matrix as a result of piezoresistance, piezocapacitance, tunneling effects and cracking mechanisms [249], making them fully compliant with the requirements for real-time strain, pressure and motion detection devices, such as soft robots, flexible, wearable, and skin mountable strain sensors and E-skin (electronic skin) [221],

[223], [250]–[254]. The bulk linear thermal expansion coefficient of the PDMS substrate, which is more than ten times higher than that of most metallic materials [229], [233], enables optical ultrasound signal generation in response to the local temperature rise created by the carbon or metal fillers upon laser excitation which is good for invasive imaging techniques such as intravascular photoacoustic imaging [234], [242], [248], [255]–[258].

2.4.3. PDMS sponge/scaffold – structure modification

In addition to adding another component to PDMS substrates, processing methods, often inspired by porous organisms in nature, have also been developed to modify the structure of pristine PDMS [172], [259], [260]. Open and closed pores can be introduced into the bulk of PDMS to fabricate new structures such as PDMS sponges and scaffolds. To date, many different approaches have been developed to fabricate PDMS sponges including direct or emulsion templating, gas forming, phase separation and 3D printing techniques [261]. Direct templating is the most commonly employed method among all the fabrication processes, where sacrificial templates (particles, crystals, beads, foams) are mixed with PDMS to create voids in the bulk after dissolution in proper solvents. Salt particles [262], sugar [263], [264] and soluble organics such as citric acid monohydrate (CAM) [265] are often used in this process as they withstand the curing conditions of PDMS and can be easily leached without hazardous chemicals. Morphological parameters essential to the properties of the products comprising pore size distribution and porosity are controllable by altering particle size and concentration of the template [261].

Many of the original advantages of pristine PDMS are further amplified by making it porous. The existence of the air voids inside the PDMS material results in lower density, higher surface area and better flexibility compared with the bulk material. These enhanced properties successfully

broaden the application of porous PDMS into the fields of catalysis [266], [267] and molecular separation [260], [268]–[270]. Yu and co-workers reported PDMS sponges prepared using CAM templates and centrifugation method with a porosity up to 85 % [265]. The PDMS samples showed an impressive water-oil separation efficiency of > 99.8 % with no degradation after 25 absorption cycles due to its superoleophilic nature. Similarly, Choi *et al.* fabricated porous PDMS using sugar particles with different sizes and concluded that increasing non-uniformity of the template crystals could result in better absorptivity of organics [263].

PDMS composite sponges can be synthesized by loading the polymer sponges with carbon and metallic particles mentioned in Section 2.3. These sponges also have potential applications in elastic electronics [271]–[278] and energy storage [279]–[282] . As an example of one PDMS-metal composite, Liang and coworkers recently fabricated metal-coated 3D interconnected Ag/Cu-PDMS sponges using an electroless deposition method [277]. The as-prepared samples turned out to have outstanding electrical conductivity to support LED lightings as stretchable circuits (Figure 2-5). Park et al. infiltrated eutectic GaIn alloy into porous PDMS skeletons to form a composite that exhibited a conductivity of 2.4×10^4 S/cm with a huge stretchability beyond 200 % strain [276].

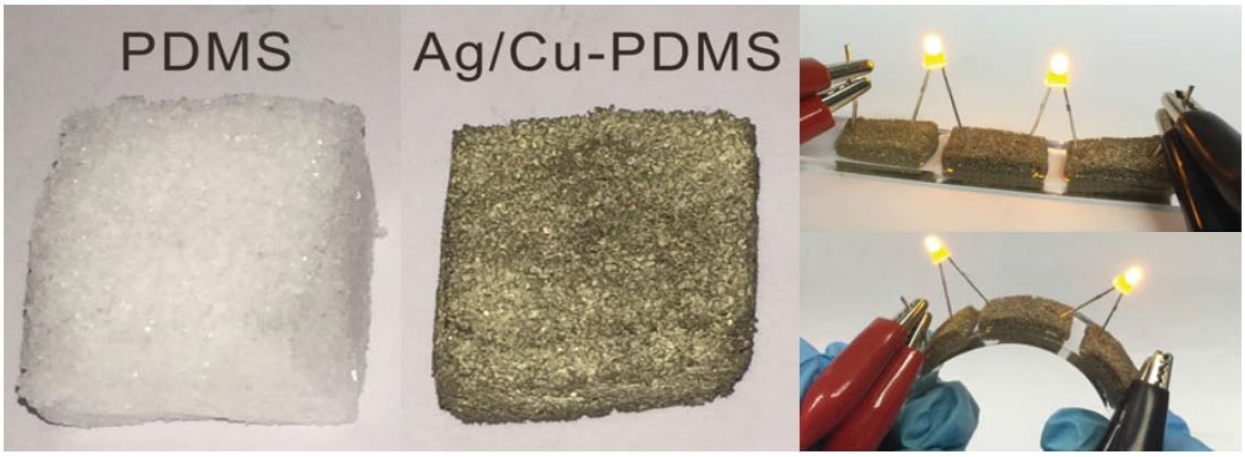

Figure 2-5 Optical images of the original PDMS sponge and Ag/Cu-PDMS sponge, and the LED circuits built with the Ag/Cu-PDMS sponge when bended [268], Copyright 2014. Reproduced with permission from John Wiley and Sons.

Another group loaded liquid GaInSn into the pores of PDMS sponges and achieved a high conductivity of 1.62×10^4 S/cm, which is as good as that of bulk GaInSn [275]. Although the performance of this composite did not surpass the work done by Park and co-workers, they introduced a more feasible synthesis process.

In a parallel scenario, carbon-based materials are also studied as fillers in PDMS scaffolds. On the one hand, the carbon (graphene, CNT and graphite)/PDMS sponges exhibited better mechanical compressibility and tolerance of large strains in comparison to pure PDMS, and can be used as a shape memory viscoelastic damper and buffer [283]–[287]. On the other hand, the inclusion of the active carbon additive brings about better electron transfer and can be applied in analogous electronic adoptions to those of the bulk composites as discussed previously [278], [288], [289].

Chen *et al.* developed a synthetic process wherein graphene sheets were anchored via chemical vapor deposition onto a PDMS foam prepared by the replication of a Ni template [290]. The resulting samples were ultra-light with a density 20 times lower than that of the solid polymer and with an improved electrical conductivity 3 orders of magnitude higher than previous results reported in literature. This light, highly conductive foam was suitable for electromagnetic interference. Moreover, in order to further increase the conductivity, Chen *et al.* assembled a blend of CNTs and rGO on the Ni-foam-derived PDMS scaffold through simple solution impregnation and subsequent incubation [291]. The interaction between graphene sheets and CNTs enabled well-dispersed distributions of each other in the structure by preventing π-π restacking, achieving continuous networks and higher conductivity than those with the same concentration of a single filler [292], [293].

Porous carbon/PMDS are also in high demand as a substantial component for secondary batteries and soft conductors. For example in the work of Li and co-workers, GO/PDMS sponges were

engineered via sugar leaching, graphene oxide infiltration and hydroiodic acid reduction [281]. Vanadium phosphate ($VOPO_4$) and hard carbon were then bonded to the interior surface of the sponges to form cathodes and anodes for sodium-ion batteries. The resultant batteries displayed good reversible capacity of 103 mA·h/g when no force was applied, and > 89 % of this capacity was maintained after 100 cycles of deformation loads. Although the main trend is still focusing on wearable, flexible sensors, the application of PDMS in the thriving new generation of energy storage and harvesting devices is an inevitable prospect of PDMS employment that can be foreseen.

In this work, PDMS was tailored in the form of an open-porous foam structure to dramatically reduce its density. These open-porous PDMS foams exhibited perfect floatability, addressing the problem wherein PDMS would sink. As a result, by introducing the open-porous structure, the PDMS foams became suitable candidates to be used as floating substrates for interfacial solar heating, once they had been loaded with photo-thermal CNP solar receivers.

2.4.4. Special surface treatment of PDMS-based materials

The innate hydrophobicity of PDMS-based materials is an asset in oil extraction, corrosion protection and self-cleaning applications, but will lead to severe contamination due to a strong affinity towards non-polar organics and thus causes safety problems [294]–[296]. To overcome this limitation, chemical treatments of have been developed to make PDMS surfaces more repellent to organics and consequently less resistive to polar molecules such as water [297].

Oxygen plasma functionalization is a classic method for reducing the hydrophobicity of surfaces, whereby extra oxygen atoms are introduced to the molecular chains to generate polar hydroxyl groups (-OH) at the expense of -CH bonding, resulting in improved chemical activity and bondability at the exposed PDMS surface [298], [299]. The resultant hydrophilic activation of the

surface is confined within a depth of a few hundred nanometers from the surface, creating no changes in the bulk properties, and the surface undergoes a hydrophobic recovery within several hours when stored in air [300]–[302].

To achieve long-lasting hydrophilicity, other strategies can be implemented to functionalize the PDMS surface via reliable assembly of selected chemical groups [303]. For example, polyethylene glycol (PEG) is a commonly used agent to achieve a hydrophilic coating. Poly(L-lysine)-*graft*-poly(ethylene glycol) copolymers, namely PLL-*g*-PEG, can be absorbed onto a plasma-treated PDMS surface in a water solution through hydroxyl/carboxylic connections [304]. In this structure PLL acts as the link in direct contact with PDMS while PEG chains formed a hydrophilic exterior which enabled impressive resistance to proteins. In another published work, Makamba *et al.* mounted PEG molecules by covalent bonding via crosslinking polyelectrolyte multilayers on top of PDMS substrates, and attained permanent suppression against biofouling [301]. However, modifying processes involving PEG are likely to produce harmful wastes, and an improved method was reported using PEG-NH_2 and 3-glycidoxypropyltrimethoxysilane and caused no damage to the ecosystem [225].

Zwitterionic polymers, representing a class of organic molecules that carry moieties with both positive and negative charges separately and appear electrically neutral on a molecular scale, have recently emerged as prospective antifouling reagents [303], [305], [306]. The stability of the hydrophilic treatment is guaranteed by (1) the covalent bonds between the chemical coating and the substrate, coupled with (2) a strong, interconnected ionic network generated by the highly polar radicals within the coated polymeric chains. In a particular study by Shiou-Bang Yeh *et al.*, the pristine PDMS was exposed to oxygen plasma and dipped into a zwitterionic sulfobetaine silane solution for silanization treatment. The testing results of the original and modified samples

indicated a reduction in surface contact angle from 103 º to around 20 º with a perfect resistance (> 99.7 %) to two kinds of bacteria, and, remarkably, could retain the hydrophilic property for over 5,000 h [307].

Quaternary ammonium polymers have been adopted in many reports as antimicrobial surfactants for lab-on-chip and cell cultivation devices. Tu *et al*. developed a quaternized poly(dimethylaminoethyl methacrylate)-PDMS surface via a surface-initiated atom transfer radical polymerization method. Instead of the regular plasma activation, the hydroxyl groups were inserted in the native PDMS chains by the immersion in piranha solution, where sulfuric acid and hydrogen peroxide provided a harsh oxidizing environment [308]. Then the cationic quaternized poly(dimethylaminoethyl methacrylate) monomers were transplanted onto the activated surfaces to create a barrier against protein/bacteria adsorption. Contact angle measurement revealed an improvement in hydrophilicity to about 47 º and experienced an increase to 30 º after undergoing hydrophobic recovery in air for two days.

Folic acid (FA) was explored as well in an attempt to combine physical and chemical approaches for PDMS hydrophilic modification by Hu and co-workers [309]. Notably, PDMS films underwent a nanoimprinting pretreatment using anodized aluminum oxide templates, followed by a salinization step to aminate the films, and finally reaction with FA to add hydroxyl, amino and carboxyl polar groups. The WCA of the FA-nano-PDMS surface decreased from approximately 110 º to 20 º but experienced a rise to 72 º in one week. This was the first time that small molecules were applied with grafting techniques to benefit microsystem analysis.

Polyvinyl alcohol, or PVA, is well-known for its affinity with water, and hence a prevalent modifier to render surfaces hydrophilic. For example, PVA was mixed with PDMS to add good hydration capability to the elastomer to imitate human skin as an epidermal skin equivalent design

[310]. With regard to surface treatment, it can be traced back to 1994 when Gilges *et al.* converted the inner wall of fused silica capillaries into hydrophilic surfaces by simply depositing PVA via thermal immobilization at 140 ^{o}C in flowing nitrogen [311]. The coating proved to be permanent, insoluble, and resistive to pH changes, as it was secured by the existence of pseudo-crystalline domains even in the absence of tight covalent coupling [312]. Subsequent studies investigated the influence of the degree of hydrolysis of polyvinyl acetate, the monomer of PVA compounds, on coating quality, and the characterization suggested that an incomplete hydrolysis of 75 % – 88 % produced stronger interactions with the surface material being coated including PDMS and polystyrene [313], [314]. Zhou led a team working on both structural and surface manipulation to fabricate a durable hydrophilic PDMS sponge using the sugar cube leaching method with a five-layer PVA coating to facilitate continuous water transportation in microchannels [315].

Due to the large surface area of the open-porous PDMS foams, it was assumed that the surface hydrophobicity/hydrophilicity would be highly influential to the properties of the foams especially in an application related to water such as in this work. To attain practical evidence to this hypothesis, part of the CNP/PDMS composite foams prepared in the experiments were treated with hydrophilic modification and compared with the original hydrophobic ones by material properties and photo-thermal performance. PVA deposition was chosen as the treatment step to induce hydrophilicity because of the non-toxicity of the chemical, stable coating quality and simple procedure.

2.5. Objective and approaches

Although mathematical analysis has been conducted for traditional solar stills in the literature, analytical studies on interfacial solar heating systems are lacking. The employment of thermal-insulating structures together with solar receivers has become a popular pattern to improve energy

conversion efficiency of interfacial solar heating, however most of these studies were reported without mentioning the underlying reasons, and quantitative analysis has not yet been reported. The work presented in this thesis addresses this research gap by offering heat transfer analysis of the effects of integrating an insulation layer into interfacial solar heating systems. Furthermore, the exploration of carbon-PDMS composites has been restricted to mainly electronic and biomedical applications. In this work the ability of carbon-PDMS composites to function as photo-thermal materials are investigated for the first time.

Numerous carbon-based interfacial solar receivers have been reported in the literature with high efficiencies between 70 % – 90 %, although there is still room for improvement. Most of the materials are highly demanding in terms of the fabrication methods, for example the requirement of low temperature conditions when fabricating carbon aerogels using freeze-drying [176], [178], [316], high temperatures needed during carbonization of mushrooms [185] and wood [187], and the use of concentrated acids to prepare GO [176], [287]. Additional structures such as cellulose and polystyrene, polyurethane are also needed in many researches to assist the solar receiver to float, wick water and reduce unwanted heat losses, resulting in complex device configurations [174], [178], [185], [195], [316]. Apparently more facile synthetic routes need to be developed and the structures providing different functions need to be integrated for the feasibility of interfacial solar heating technologies in practical desalination applications.

The work presented in this thesis focuses on the enhancement of solar desalination efficiencies using localized heating technologies. To achieve the goal of advancing the photo-thermal conversion efficiency of air-water interfacial solar heating systems to 80 % or higher, an all-in one CNP/PDMS composite foam was designed and fabricated using a facile salt-leaching method with suitable properties to enhance water evaporation. According to the literature review, the

composites should exhibit exceptional light absorptivity to capture solar energy and convert it into thermal energy effectively, suitable thermal properties to control heat losses, good floatability to ensure the proper air-water interfacial position, and an environmental-friendly nature for sustainable considerations. These requirements are fulfilled by carefully tailoring the chemical composition and physical structure of CNP/PDMS photo-thermal composite foams. Moreover, characterization and evaporation tests are carried out on these foams to optimize and support the validity of the design at a laboratory level, and eventually provide insights for practical desalting applications.

The analysis was first conducted to provide a theoretical basis and insight for the design of photo-thermal films for interfacial solar heating systems. This analysis will be elucidated in Chapter 3 from a heat transfer perspective to investigate the effect of an insulation structure on the energy distribution in interfacial solar heating systems during the solar heating process. Chapter 4 describes the fabrication of various CNP/PDMS composite foams, including all the synthetic parameters for each sample. Chapter 5 presents the characterization of the morphologies, optical properties, thermal properties and wettability of the as-prepared CNP/PDMS foams. The photo-thermal performance of CNP/PDMS foams, determined from solar-driven evaporation tests, are presented in Chapter 6. During the evaporation tests foams were situated at the air-water interface and subjected to simulated solar illumination while the mass change of the water and temperature at three representative locations in the system were monitored. Data from the experiments was collected and analyzed to derive the average vapor generation rate, overall energy conversion efficiency and the temperature profile of the solar heating system over the duration of the tests. In Chapter 7 the key findings of this work are summarized, and future directions are proposed.

3. Numerical Analysis of Interfacial Solar Heating

Water evaporation is never a simple procedure related only to the heat source and vapor flux. It is an outcome of the interaction of many parameters including water depth, salinity, basin material, energy intensity, wind, humidity, ambient temperature and other relevant factors when talking about practical cases. To date, plenty of simulations and mathematical analysis of heat and mass transfer in traditional solar distillation plants [317]–[320], thermodynamic analysis of irreversible processes in a symmetric structure [321]–[323] and molecular modeling for general water evaporation [324], [325] have been reported in published work. However, few studies have paid attention to heat loss mechanisms in interfacial solar receivers used for air-water solar heating from a heat transfer perspective to seek quantitative explanations for their superior performance.

This chapter provides a heat transfer analysis to examine some of the influential factors in solar-driven air-water interfacial steam generation systems aiming to comprehend the general interrelation among input power, surface temperature of the interfacial solar receiver and vaporization rate as the first step of the project. The solar receiver was assumed to be a film with a negligible thickness made of a high-performance photo-thermal material (e.g. carbon-based) exhibiting high absorptivity towards solar radiation such that its temperature was sufficiently increased to facilitate water evaporation. The analysis was conducted for two configurations:

(1) the photo-thermal receiver at the air-water interface;
(2) the photo-thermal receiver at the air-water interface with an insulation layer inserted between its lower surface and the bulk of the water.

Heat transfer processes, including convection and radiation from the film to its surrounding environment (water and air) have been evaluated for a given range of film temperatures to

determine the relative share of each heat loss mechanism as well as the energy contributed to water evaporation for the two configurations above. The effect of the added insulation layer on the systematic energy distribution can thus be inferred from the loss analysis. Details will be described in the following three sections.

3.1. General assumptions

To simplify the heat transfer analysis, assumptions are made in the interfacial heating system as listed below.

(1) Solar radiation is incident onto a planar solar receiver from the normal direction. The light coming from the environment is not considered.

(2) In practice the photo-thermal receiver would be porous to allow vapor to escape from the reservoir. However, an assumption is made that the photo-thermal film is flat on both its upper and lower surfaces and has zero thickness for simplification.

(3) The temperature of the photo-thermal film T_f is given in a range from 300 to 340 K in the calculation, which are typical evaporation temperatures according to the literature. It is reasonable to assume that the film is heated isothermally with the solar energyT_f considering its high absorptivity and high thermal conductivity and negligible thickness.

(4) The physical and chemical properties of the film are assumed to be independent of temperature and its heat capacity is negligible.

(5) The analysis presented here is a quasi-steady state case. Hence horizontal heat diffusion along the planar direction of the film is not considered.

(6) Small turbulence induced by mass transfer from the bulk water to the zone that is heated directly below the film is not considered.

(7) Edge effects are not considered in the calculation.

(8) The material of the reservoir holding the water (both sidewalls and bottom) are perfect thermal-insulators with negligible thermal capacity.

(9) The reservoir is deep enough such that the temperature of the water T_{w0} far beneath the air-water interface maintains a constant value (288 K).

(10) The air is quiescent and remains at an unaffected temperature, T_a = 296 K, at distances far above the film receiver.

(11) Both the air and water vapor behave as ideal gases with unchanged thermal properties in the given temperature range.

The parameters considered in the analysis as well as the dimensions and related physical properties are provided in Table 3-1.

Table 3-1 Symbols and values of related parameters and physical properties in the heat transfer analysis of the two interfacial solar heating configurations.

A	Surface area of the photo-thermal film (m^2)
C	Specific heat capacity of water (4.2 kJ/kg·K)
g	Acceleration due to gravity (9.8 N/m^2·s)
$\bar{h}$	Heat transfer coefficient of natural convection (W/m^2·K)
$\overline{h_a}$	Heat transfer coefficient of natural convection to the air (W/m^2·K)
h_{fg}	Latent heat of water (2,400 kJ/kg at 45 °C)
$\overline{h_w}$	Heat transfer coefficient of natural convection to the bulk water (W/m^2·K)
k	Thermal conductivity (W/m·K)
k_i	Thermal conductivity of the insulation layer (0.05 W/m·K)
L	Side length of the photo-thermal film (0.09 – 2.5 m)
L_c	Characteristic length of the photo-thermal film (= L/4 m)
m	Weight (g)
$\dot{m}$	Evaporation rate or vapor flux from water to the air (kg/m^2·h)
$\overline{Nu_L}$	Nusselt number
Q_{ci}	Conductive heat transfer from the photo-thermal film to the insulation layer (J/m^2·s)

Q_{evap}	Heat use for water evaporation (J/m^2·s)
Q_{ra}	Radiative heat transfer to the air (J/m^2·s)
Q_{rw}	Radiative heat transfer to the bulk water (J/m^2·s)
Q_{va}	Convective heat transfer to the air (J/m^2·s)
Q_{vw}	Convective heat transfer to the bulk water (J/m^2·s)
R	Thermal resistance (K/W)
Ra_L	Rayleigh number
T_a	Temperature of the air (296 K)
T_f	Temperature of the photo-thermal film (300 – 340 K)
T_w	Temperature at the interface of the photo-thermal film and the underlying water (K)
T_{w0}	Initial temperature of the water (288 K)
ΔT	Temperature difference between relevant locations (K)
α	Thermal diffusivity (m^2/s)
β	Volume thermal expansion coefficient (/K)
γ	Kinetic viscosity (m^2/s)
δ	Thickness of the insulation layer (m)
ε	Emissivity of the photo-thermal film (0.9)
σ	Stefan-Boltzmann constant (5.67×10^{-8} W/m^2·K^4)

3.2. Calculation

Natural convection. Within the given T_f (300 – 340 K), convective heat losses from the film to the air and water are calculated using Newton's Law of cooling:

$$Q_{va} = A\overline{h_a}\left(T_f - T_a\right) \tag{1}$$

$$Q_{vw} = A\overline{h_w}\left(T_f - T_{w0}\right) \tag{2}$$

where the heat transfer coefficients are calculated using the following empirical correlations [326]:

$$Ra_L = \frac{g\beta\Delta T{L_c}^3}{\alpha\gamma} \tag{3}$$

$$\overline{Nu_L} = \begin{cases} 0.54 Ra_L^{\frac{1}{4}} \, (air, 10^4 \le Ra_L \le 10^7) \\ 0.27 Ra_L^{\frac{1}{4}} \, (water, 10^5 \le Ra_L \le 10^{10}) \end{cases} \quad (4)$$

$$\bar{h} = \frac{k\overline{Nu_L}}{L_c} \quad (5)$$

This estimation process is valid when the side length of the square photo-thermal film, L, is between 0.09 – 2.5 m, which sets the Ra_L value within the required range for equation (4).

Radiation. Radiative heat losses from the film surface to the air and water are calculated using the Stefan-Boltzmann Law:

$$Q_{ra} = A\varepsilon\sigma\left({T_f}^4 - {T_a}^4\right) \quad (6)$$

$$Q_{rw} = A\varepsilon\sigma\left({T_f}^4 - {T_{w0}}^4\right) \quad (7)$$

Conduction. Conductive losses across the insulation layer in configuration 2 are calculated by the following equation:

$$Q_{ci} = \frac{\mathrm{A}k_i\left(T_f - T_w\right)}{\delta} \quad (8)$$

where T_w denotes the temperature at the lower surface of the insulation layer.

Energy for evaporation. Thermal energy transferred from the film receiver to the evaporative layer consists of two parts. One is the latent heat (h_{fg}), or the driving energy of the liquid-gas phase change process. The other one is the sensible heat calculated using the heat capacity of water (C) and the increase of the water temperature from the initial temperature, T_{w0}, to the final temperature, T_f, because the temperature of the vapor is assumed to be the same as that of the film. Thus, the energy used for water evaporation is given by the following formula, which accounts for contributions from both latent and sensible heating:

$$Q_{evap} = A\dot{m}\left[h_{fg} + C\left(T_f - T_{w0}\right)\right] \tag{9}$$

To determine the mass flux of the vapor at the air-water interface $\dot{m}$, an empirical description as a function of the surface temperature of the interfacial receiver T_f has been derived based on experimental data in the literature as shown in Figure 3-1 [146], [175], [327]–[329]. That is, by reviewing the experimental results in the reported air-water interfacial solar heating systems with various photo-thermal sheet-like carbon materials such as graphene, rGO and graphite, an exponential curve fitting of the evaporation rate versus surface temperature of the employed material has been applied and the resultant correlation is

$$\dot{m} = 4 \times 10^{-7} \exp\left(0.0474 T_f\right) \tag{10}$$

The evaporation rates achieved are between 0.92 kg/m^2·h and 3.5 kg/m^2·h in most studies.

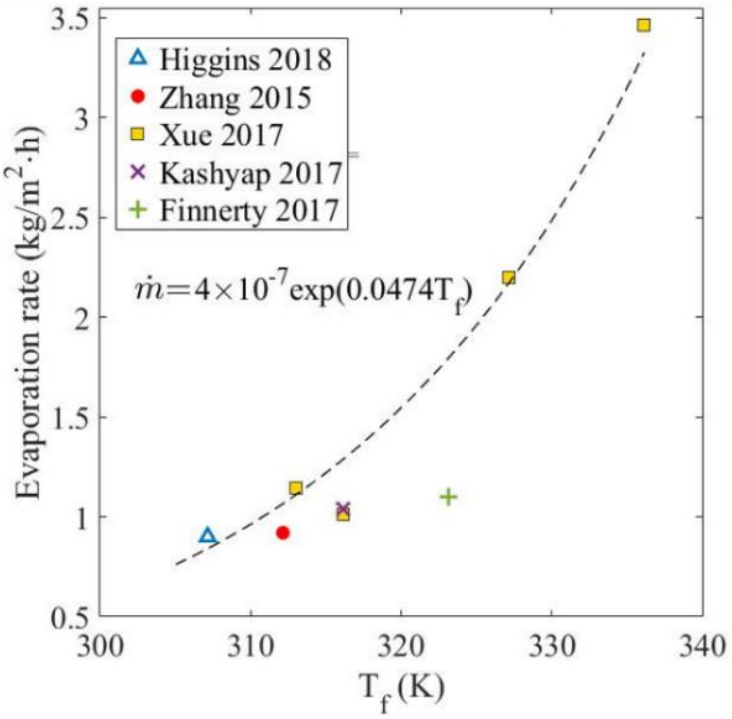

Figure 3-1 Exponential fitting of the evaporation rate using carbon-based interfacial solar receivers reported in the literature ($R^2 = 0.8415$) [146], [175], [327]–[329].

The calculated amount of thermal energy of natural convection, radiation, conduction and evaporation are compared to determine the major heat loss mechanisms and the effect of the insulation layer in Section 3.3.

3.3. Interfacial solar heating model

As mentioned previously, the interfacial solar heating system was modeled with two configurations. In configuration 1, the interfacial receiver floats at the air-water interface and is in direct contact with the water (as shown in Figure 3-2 (a)). The thermal resistance circuit of the heat transferred from the solar receiver is shown in Figure 3-2 (b), which is consistent with the assumption that vaporization takes place in an ultra-thin layer (evaporative layer) at the same location where the receiver resides. Except for the latent heat of evaporating water, heat is dissipated from the hot film by means of convection to the air (Q_{va})$^{Q_{va}}$, radiation to the air (Q_{ra}) Q_{ra}, convection to the bulk water (Q_{vw}), and radiation to the bulk water (Q_{rw})$^{Q_{rw}}$.

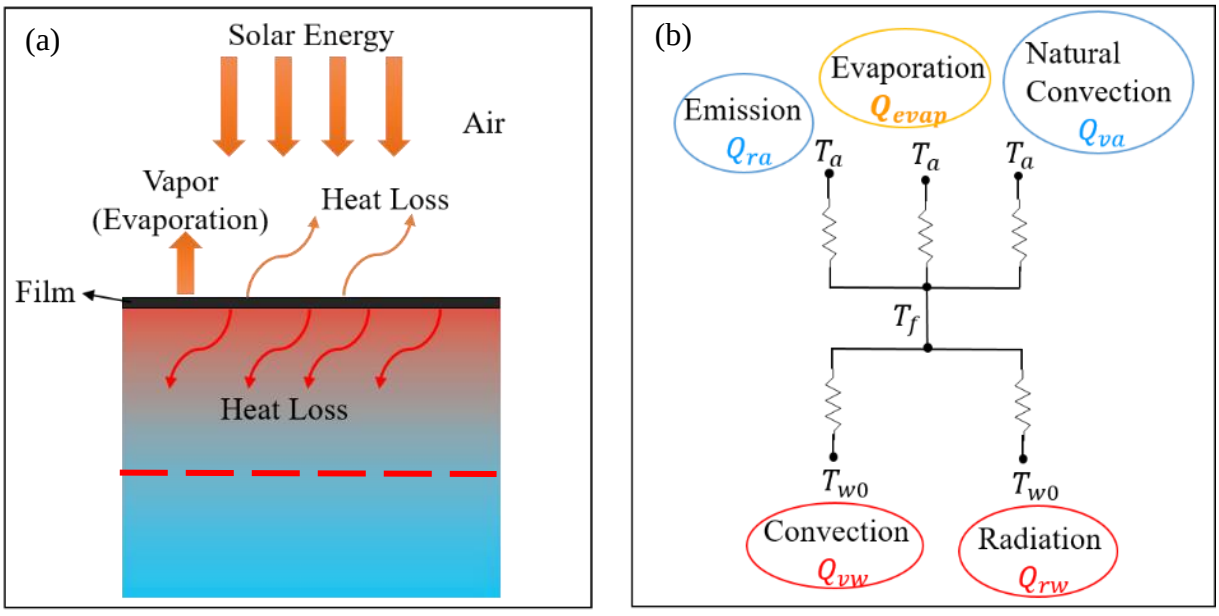

Figure 3-2 (a) Schematic illustration and (b) thermal resistance network of configuration 1 photo-thermal film without the insulation layer.

In configuration 2, the air-water interfacial solar heating configuration, an insulation layer (such as a polystyrene foam with a low thermal conductivity of 0.05 W/m·K) is inserted below the solar receiver to reduce convective loss to the bulk of the water, with a small spacing in between as a confined preheating region (see Figure 3-3). The insulation layer is wrapped with a cellulose paper to provide capillary force to continuously drive water up to the evaporative layer for replenishment. The influence of this structure on evaporation processes is assumed to be negligible. In other words, water is driven by capillary forces from the bulk to the heat-up zone between the film receiver and the insulation layer. The thin water layer formed to fill the preheating region, herein referred to as the "heat-up zone" in Figure 3-3 (a), is maintained with a thickness of ~ 0.1 mm during the entire evaporation process and is assumed to be at a temperature equal to that of the film (T_f) based on its small volume. The amount of thermal energy transferred from the film downwards through the insulator is equivalent to the sum of the convective and radiative heat losses from the bottom of the insulation layer to the bulk water, and can be written as

$$Q_{ci} = Q_{vw} + Q_{rw} \tag{11}$$

Thus, the total heat loss from the photo-thermal film is estimated to be the sum of three mechanisms: radiation and convection to the air, together with conduction to the insulation layer. In this configuration the temperature at the insulating layer-bulk water interface, T_w, is used to calculate the radiative and convective heat losses to the bulk of water and is determined using equation (11).

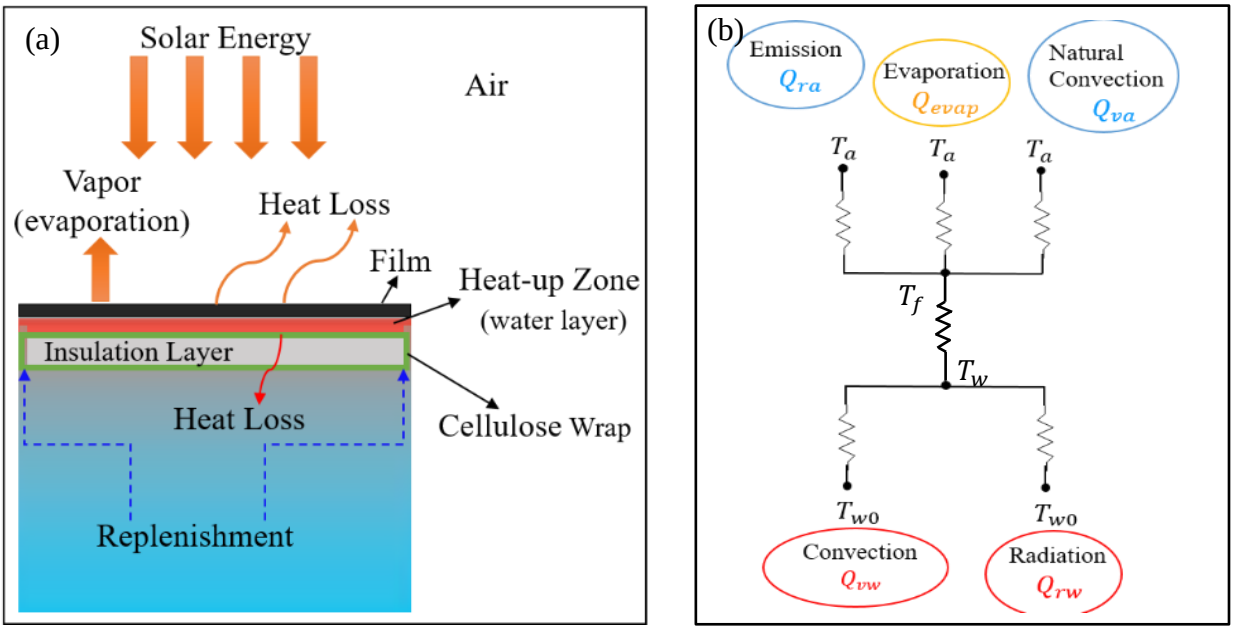

Figure 3-3 (a) Schematic illustration and (b) thermal resistance network of configuration 2. An insulation layer with a thermal conductivity of 0.05 W/m·k was placed underneath the photo-thermal film in the solar interfacial heating system.

3.4. Results

The analysis is performed for interfacial solar heating models using different film dimensions (L = 0.09 – 2.5 m) and L = 0.3 m will be described as an example here. The amount of the energy carried by different heat transfer paths are obtained and plotted as a function of film temperature T_f in Figure 3-4.

For configuration 1, with no insulation layer in the setup, the thermal energy transferred through all the pathways steadily increases with T_f since the root driving forces, namely the temperature difference between the film and its surrounding environments, are amplified because of the unchanged temperature in the bulk water and the air (see Figure 3-4 (a)). When the film receiver reaches a temperature of 340 K, the sum of the heat lost to the air (Q_{ra} and Q_{va}) and radiation to

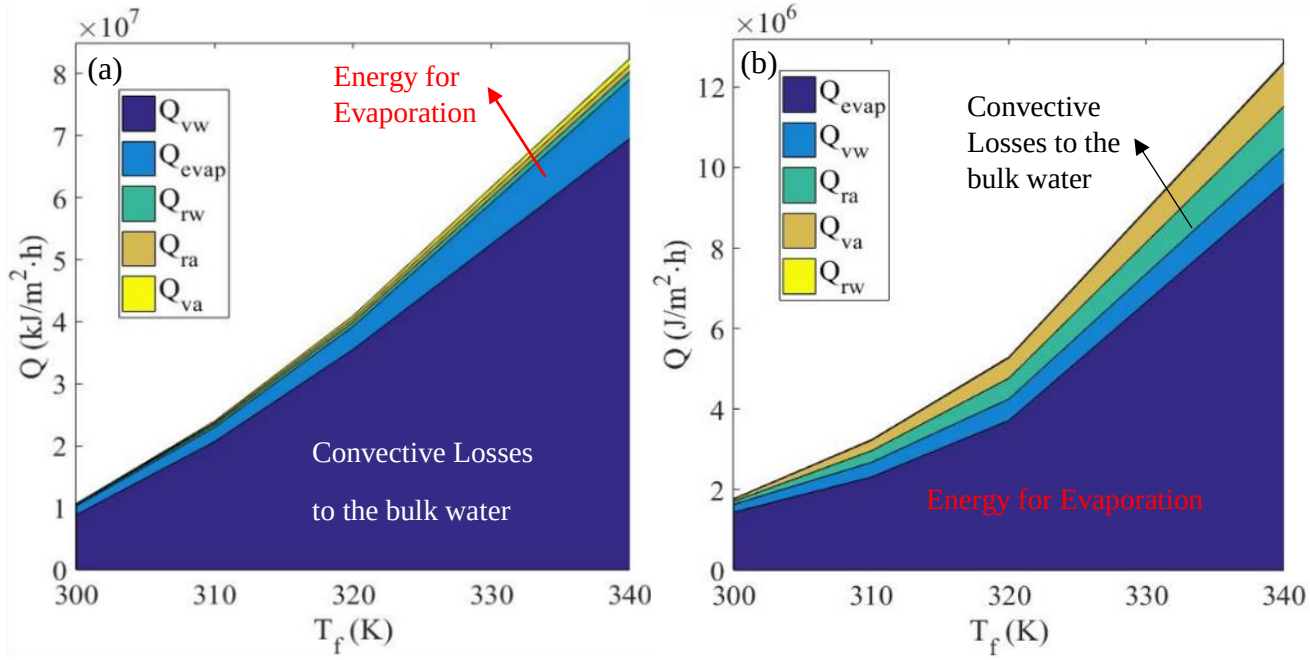

Figure 3-4 Results of the heat transfer analysis for both configurations with the photo-thermal film (L = 0.3 m) in the system. Thermal energy transferred from the photo-thermal film due to water evaporation, convection and radiation to the water, and convection and radiation to ambient air as a function of T_f in (a) configuration 1 without the insulation layer, and (b) configuration 2 with an insulation layer (δ = 0.001 m).

the bulk water Q_{rw} is merely 4 %. In the meantime, the amount of energy used to evaporate water, Q_{evap}, is predicted to be ~ 9.6 × 10^6 J/m^2·h, whereas the convective loss to the bulk water, Q_{vw} (), is almost 7 times higher than Q_{evap} (≈ 80 % and 10 % of the energy input respectively) dominating over other heat transfer processes. It can be concluded that natural convection to the bulk water is the fundamental loss mechanism which suppresses the efficiency of air-water interfacial solar heating evaporation systems. The heat transfer coefficient of this convective loss $\overline{h_w}$ is estimated to be between 205 – 370 W/m^2·K.

In configuration 2, the influence of the insertion of an insulation layer beneath the photo-thermal film receiver to mitigate convective heat losses from the film to the bulk water is analyzed and the results are shown in Figure 3-4 (b). The results indicate that the addition of an insulation layer

significantly alters the thermal energy distribution greatly. By using a tiny insulation layer (δ = 0.001 m), an extra resistance is added to the heat flow, resulting in a low T_w at the film-water interface. The convective loss Q_{vw} is thus reduced dramatically in that the temperature difference between the insulation layer and the bulk of water is decreases by about 90 % and the value of $\overline{h_w}$ decreased to a range of 95 – 155 W/m^2·K when 300 K < T_f < 340 K. Q_{vw} is calculated to be 8.77 × 10^5 J/m^2·h at a film receiver temperature of T_f = 340 K, which is only 1.26 % of its former value of 6.95 ×10^7 J/m^2·h in configuration 1 where the insulating material is absent. Consequently, the percentage of heat used in evaporating water, Q_{evap}, is promoted from 11 % to 76 % of the total energy received by the film receiver in the system. Moreover, the influence of the insulation layer thickness on Q_{vw} is also shown in the inset in Figure 3-5. As the insulation layer becomes thicker, the convective heat losses to the bulk water are further decreased. For the thickest insulation layer

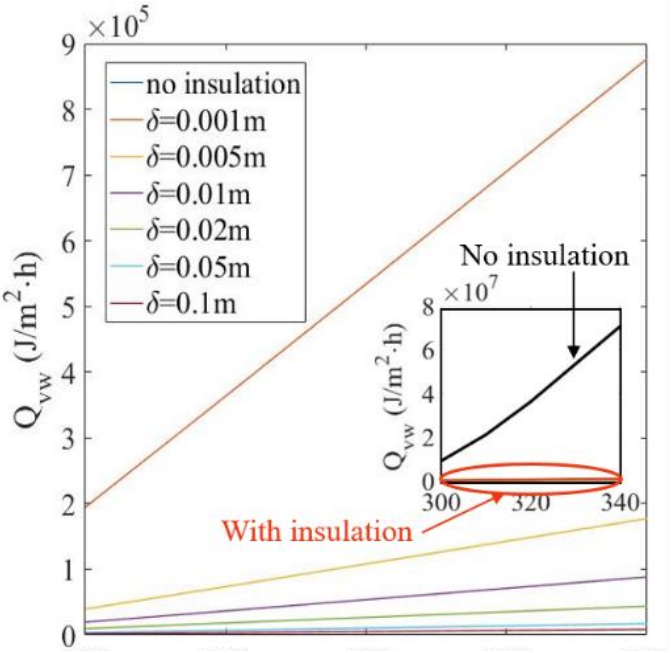

Figure 3-5 Convective heat losses to the bulk of water versus T_f in configuration 2 using a photo-thermal film (L = 0.3 m) and insulation layers with different thicknesses (δ = 0.001, 0.005, 0.01, 0.05 and 0.1 m). The inset shows the huge difference between the convective losses to the bulk of water of two configurations.

considered in this chapter, δ = 0.1 m, convective loss to the bulk water decreases to < 9,000 J/m^2·h, even lower than Q_{ra} and Q_{va}. Thermal energy dissipations to the air, namely Q_{ra} and Q_{va}, stay unchanged because they are decided by T_f and T_a regardless of the presence of the insulation layer.

3.5. Summary of the analysis

In short, the numerical analysis of the thermal energy losses in air-water interfacial solar heating systems indicates that free convection to the underlying water body is the dominant loss mechanism, wasting up to over 80 % of the available thermal energy. However, these heat losses to the underlying water can be reduced dramatically by inserting an insulation layer with a low thermal conductivity below the solar receiver. Generally, for the range of values of L and T_f considered in this heat transfer analysis, the heat transfer coefficient of the natural convection to the bulk of water, $\overline{h_w}$, is reduced from 120 – 500 W/m^2·K to a much lower level of 50 – 210 W/m^2·K after adding a 0.001 m insulation layer (see Figure 3-6), and thus the photo-thermal

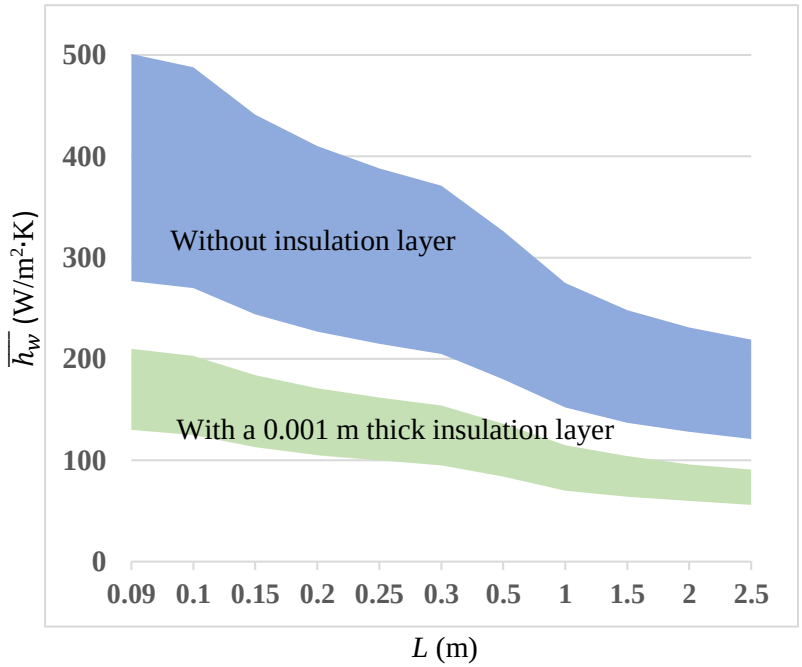

Figure 3-6 the calculated heat transfer coefficient from the photo-thermal film to the underlying bulk of water for the two configurations (L = 0.09 – 2.5 m, T_f = 300 – 340 K, δ = 0.001 m).

conversion efficiency can be enhanced. The natural convection to the air $\overline{h_a}$ for all cases is less than 9 $W/m^2 \cdot K$ and not sensitive to the insulation structure. In practical interfacial solar desalination systems, the application of thermally insulated structures, or using photo-thermal structures with low thermal conductivity is recommended to effectively suppress heat losses to the bulk of the reservoir and improve the overall performance.

The key findings from this chapter are considered in the design and fabrication of a carbon-PDMS composite for enhanced interfacial solar water evaporation. As will be described in Chapter 4, the composite exhibits the desired properties including high solar absorptivity, good photo-thermal conversion ability, floatability and lower thermal conductivity than water. In addition, open-porous structures are introduced to the material, providing for water replenishment during the evaporation process.

4. Synthesis of PVA-CNP/PDMS Composite Foams

This chapter presents the fabrication (shown in Figure 4-1) of polyvinyl alcohol **(**PVA)-modified flexible carbon nanoparticle (CNP)/polydimethylsiloxane (PDMS) composite foams with macroscopic open-porous structures and improved wettability. Notably, structure and composition modification of PDMS polymer were both adopted in this work by combining the reported salt-leaching technique [261], [262] and CNP doping method [270], [272] for the first time, together with a PVA-based surface modification to obtain a material with desirable photo-thermal properties, effective heat localization, good floatability, and chemical stability to support efficient interfacial solar heating.

4.1. Chemicals and reagents

Commercially available clear polydimethylsiloxane (PDMS, SYLGARD^{TM} 184 silicone elastomer) was purchased from Dow Corning Corporation in the form of a two-part kit consisting of the base pre-polymer and the curing agent. Carbon nanoparticles (CNP, amorphous, particle size < 100 nm, molecular weight = 12.01 g/mol) from Sigma-Aldrich was used as a filler. Polyvinyl alcohol (PVA, 87 – 90 % hydrolyzed, average molecular weight = 30,000 – 70,000 g/mol) was purchased from Sigma-Aldrich and was used to render the PDMS hydrophilic. All materials were used as received without further modification.

4.2. Preparation of PVA-CNP/PDMS composite foams

Step 1. Preparation of CNP/PDMS slurry

The open-cell foams were fabricated via a facile leaching method using salt particles as the template. The CNP/PDMS mixture was first prepared by adding CNP to PDMS pre-polymer at a

10:1 weight ratio to form a clear liquid blend of the base and the curing agent. The CNP concentration was tunable simply by varying the mixing ratio of CNP and PDMS in this step. A black, viscous slurry was obtained after blending with a glass stick and 15 min of sonication (40 kHz, 110 W) in an ultrasonic cleaning bath (CPX3800, Fisherband).

Step 2. Preparation of CNP/PDMS foams

Table salt was sieved in advance to separate particles bigger than 500 μm in diameter, to be used as the sacrificial template, which were added to the CNP/PDMS slurry immediately after the sonication in Step 1. The salt/CNP/PDMS system was thoroughly stirred before being subjected to vacuum desiccation for about 1.5 hours to remove trapped air bubbles. Longer degassing time reported in the literature (for example 2 hours [264], [277]) is not necessary since the working time of SYLGARD^{TM} 184 is only 90 min under room temperature according to the manufacturer, after which the cross-linking reaction between the base and curing agent will take place [330].

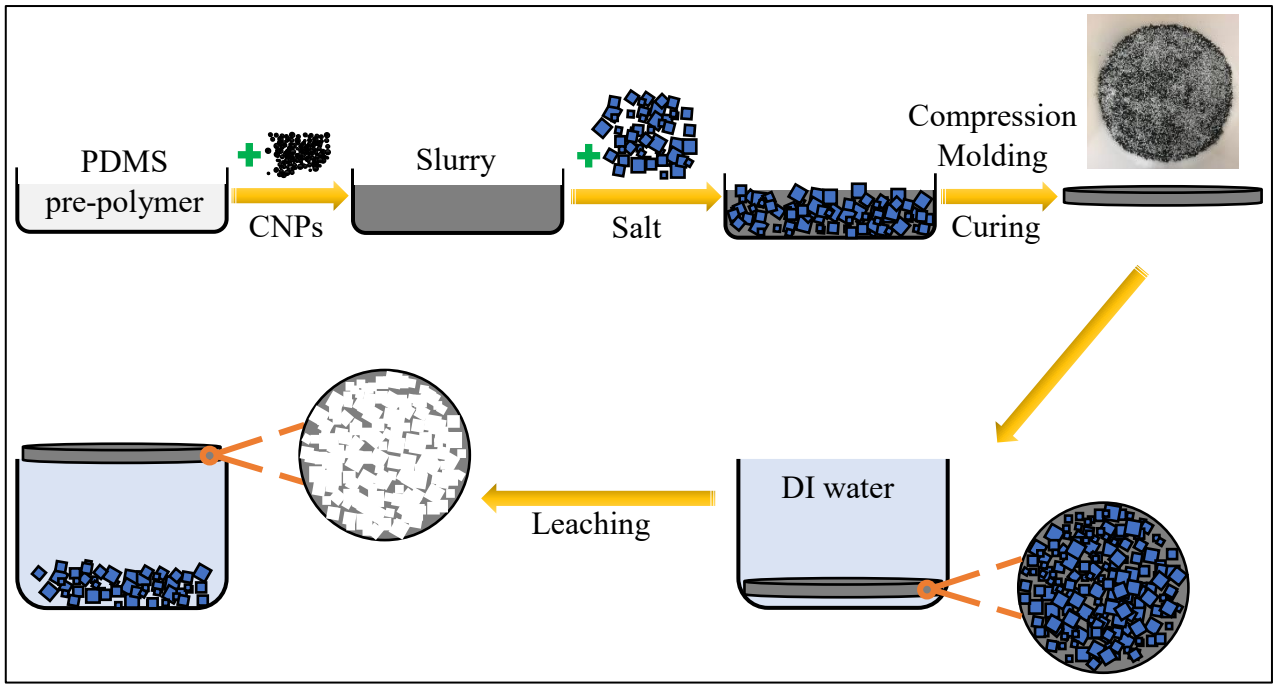

Figure 4-1 Schematic illustration of the salt-leaching fabrication of the CNP/PDMS composite foams.

Subsequently, the mixture was put into a cylindrical, 3D-printed PLA mold and loaded into the compression molding machine (4386 CH, Craver Press) which was used to apply a constant external pressure of 2,000 psi at room temperature for a duration of 120 s to obtain salt/CNP/PDMS discs with a diameter of 70 mm. After overnight curing at 50 ^{o}C in the oven, the solidified discs were transferred to the freezer right away and cooled at a temperature of -10°C for 3 min to detach the PDMS scaffold from the template. Subsequently, the salt crystals were dissolved in DI water on a hotplate heated to 60 ^{o}C for more than 6 hrs, with the water being refreshed multiple times as needed. Due to the low foam density and the inherent surface hydrophobicity of PDMS, the samples gradually rose from the bottom of the container and floated at the air-water interface as the salt template was washed away. The CNP/PDMS open-cell foams were finally attained after drying in air at 50 ^{o}C.

Step 3. Preparation of PVA aqueous solution

To prevent gelation, 5 g of PVA powder was slowly added to 495 g of DI water at room temperature with magnetic stirring for 40 min until the polymer powder was dispersed in the liquid phase and formed a whitish solution. Then the mixture was heated to 80 ^{o}C on a hot plate for another 40 min, maintained at a lower temperature of 65 ^{o}C overnight and cooled down to 25 ^{o}C naturally. The setup was equipped with a reflux unit while being heated to prevent water loss and retain the expected PVA concentration. Constant stirring was applied throughout the entire process. A clear, stable 1 wt% PVA solution was then ready for later use. Original hydrophobic CNP/PDMS foams were obtained when this step was completed.

Step 4: Hydrophilic modification of CNP/PDMS foams.

The resultant PDMS/CNP foams from Step 2 were treated by oxygen plasma (PDC-001-HP, Harrick Plasma) for 60 s. The as-prepared PVA solution was poured onto the surface of the activated foams immediately after the oxygen plasma treatment. The PDMS foams were left immersed in the PVA solution for 15 min, blown with air to remove unattached PVA and dried at 50 ^{o}C to deposit the hydrophilic PVA coating on the wall of the porous structure. Due to the plasma exposure, the inert chemical groups in the side chains of PDMS temporarily became polar, enhancing the subsequent chemical coating process wherein PDMS was soaked in PVA, as discussed in Chapter 2. This coating step was repeated 5 times and PVA was immobilized at 115 ^{o}C for 15 min to finish the modification. PVA-CNP/PDMS foams with hydrophilic coatings were obtained.

4.3. Experimental variations

The main parameters of the PVA-CNP/PDMS foams were tunable through the adjustments of the synthetic conditions including:

- CNP concentration (CNP %) – controlled by the weight ratio of CNP and PDMS pre-polymer in Step 1;
- porosity (ϵ) – determined by the ratio of salt and PDMS pre-polymer in Step 2 (estimated volumetric percentage using the formula: $\epsilon = \frac{m_{salt}/\rho_{salt}}{m_{PDMS}/\rho_{PDMS}+m_{salt}/\rho_{salt}} \times 100\ \%$);
- thickness (τ) – controlled by the absolute amount of salt/CNP/PDMS mixture used in the compression molding in Step 2;
- hydrophilic coating – coated or not coated with PVA (conduct or skip Step 4).

For the purpose of variation control, the porosity was set the same for all foams (theoretically 85 % according to the calculation). The other three parameters were explored for their effect on foam properties and photo-thermal performance.

The fabricated samples are listed in below in Table 4-1. For sample identification:

- pristine PDMS structures with no pores (sample 1 and 2) are marked by "p-". The rest of the samples are all foams
- CNP content and thickness of the samples are tagged as prefix and suffix in the following chapters respectively. Samples without CNP fillers (0 wt%) do not have "CNP" in their names
- samples with and without a PVA coating are labelled "PVA-CNP/PDMS" and "CNP/PDMS"

Sample 9, for example, is a PDMS foam doped with 0.5 wt% CNPs with a thickness of 1 mm. Thus, it is called "0.5CNP/PMDS-1.5" and "PVA-0.5CNP/PDMS-1.5" before and after PVA treatment.

Relative studies are shown in Table 4-2, where the influence of the hydrophilic coating, foam thickness and doping level of CNP on sample properties and photo-thermal performance are investigated and compared in the following chapters. Sample 1 – 5 are the control samples used in different characterization and studies.

Table 4-1 List of the as-prepared CNP/PDMS composite foams.

Sample No.	**Sample label**	**τ (mm)**	**CNP content (wt%)**	**Theoretical porosity**
1	p-PDMS-2	2	0	0
2	p-5CNP/PDMS-2	2	5	0
3	PDMS-1	1	0	85 %
4	PDMS-1.5	1.5		
5	PDMS-2	2		
6	5CNP/PDMS-1	1	5	

7	5CNP/PDMS-1.5	1.5		
8	5CNP/PDMS-2	2		
9	0.5CNP/PDMS-1	1	0.5	
10	1CNP/PDMS-1	1	1	
11	2.5CNP/PDMS-1	1	2.5	
12	7CNP/PDMS-1	1	7	
13	10CNP/PDMS-1	1	10	
14	13CNP/PDMS-1	1	13	
15	15CNP/PDMS-1	1	15	
16	20CNP/PDMS-1	1	20	
17	30CNP/PDMS-1	1	30	

Table 4-2 Samples involved in studies of the effect of three different factors: wettability, sample thickness and CNP doping concentration.

Study	**Samples involved**	**Hydrophilic modification**
Wettability	6 – 8	Tested both with and without PVA coating
Thickness	3 – 8	Tested with PVA coating
CNP concentration	3, 6, 9 – 17	Tested with PVA coating

5. Characterization of CNP/PDMS Composite Foams

The as-prepared pristine PDMS film and CNP/PDMS foams were characterized by their morphologies, optical and thermal properties.

5.1. Macroscopic appearance and mechanical flexibility

Digital images of the as-fabricated samples are shown in Figure 5-1 (a), which have a diameter of about 45 mm (except for the pristine PDMS) and thickness ranging from 1 to 2 mm. The pristine PDMS is a transparent and colorless elastomer but loses its transparency after the introduction of a large number of pores in the salt-leaching process. The foams were pigmented because of the inclusion of CNPs with a greyscale varying according to the doping level. CNP/PDMS foams are grey when the amount of CNP is lower than 1 wt% and become completely black beyond this concentration. No difference can be observed with the naked eye before and after PVA modification.

The PVA-CNP/PDMS and CNP/PDMS foams exhibit excellent bendability, which can be seen in Figure 5-1 (b), due to the inborn elasticity of the PDMS matrix. However, this flexibility does cause a contraction of around 10 % of both the diameter and thickness of the sample during the incubation after leaching. To overcome this volume change, the mold was designed to be Ø70 mm, big enough to compensate for the shrinkage and the foams were resized to the suitable dimension. In addition, it is noticed that the CNP/PDMS foams are more resistive to external forces than the white foams without CNP fillers, showing better mechanical strength which is broadly stated in the literature on carbon-reinforced polymers [283], [331]. Figure 5-1 (c) shows the light weight

(0.4 – 1 g with the given sample size) of the CNP/PDMS composite foam with a low density of 0.2 – 0.3 g/cm^3.

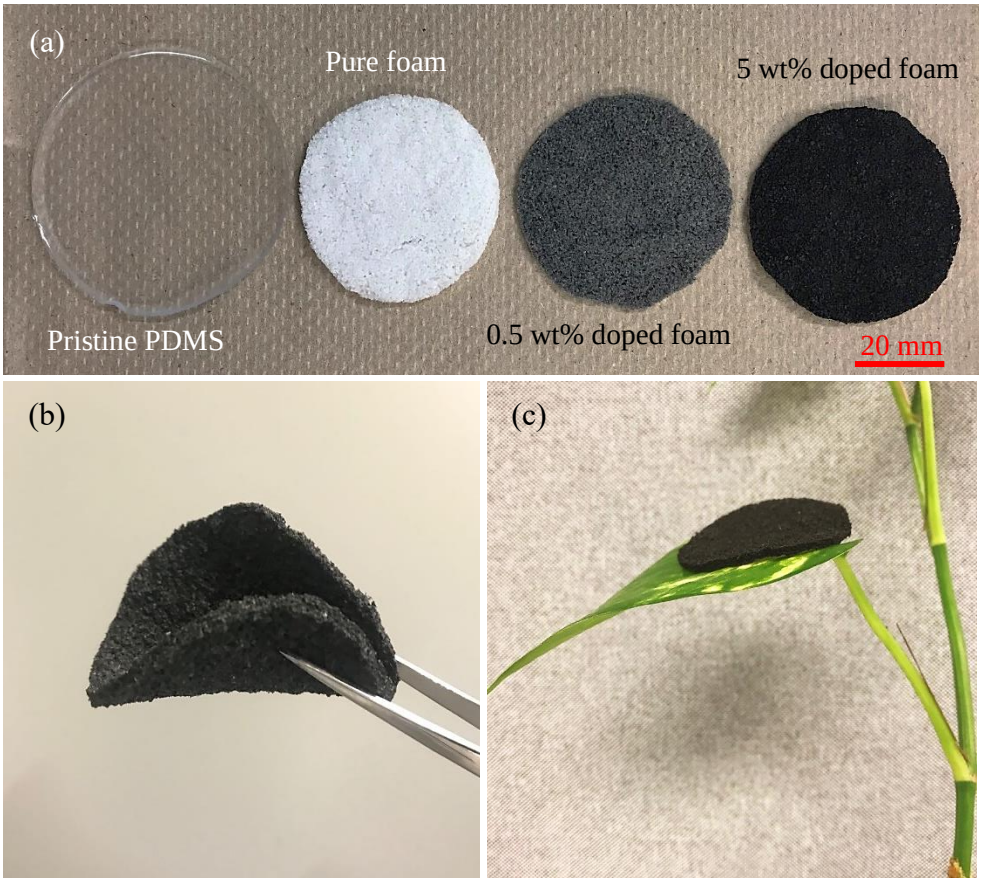

Figure 5-1 Digital images of the samples. (a) From left to right: sample 1(p-PDMS-2), sample 5 (PDMS-2), sample 9 (0.5CNP/PDMS-1), sample 8 (5CNP/PDMS-2). (b) Sample 8 was bended using a tweezer showing excellent flexibility. (c) Sample 8 was placed on a leaf and only supported only by the stem.

5.2. Scanning electron microscopy (SEM)

The surface morphology of the samples was characterized using a scanning electron microscope (SEM, Thermofisher Quanta 3D FEG, FEI Company). The SEM was operated at an accelerating voltage of 5 – 20 kV and a low vacuum mode (chamber pressure between 50 and 90 Pa) was employed to image the non-conductive CNP/PDMS foams with a secondary electron detector.

The porous structures in the foams is examined. Figure 5-2 (a) shows the cross section of the 5CNP/PDMS-2 foam where pores can be seen with a regular cubic shape, the same as the salt templates. The side lengths of the pores are around 400 μm, which is smaller than the salt particles (around 500 μm) due to the shrinking problem occurred in the leaching process.

Images were also taken to see the CNP distribution in the composites. Figure 5-2 (b) shows the cross section of sample 2 (p-5CNP/PMDS-2), that is, pristine PDMS film doped with 5 wt% CNP with a non-porous structure. To expose a cross section to perceive the CNP distribution inside the bulk of the polymer substrate the film was broken in liquid nitrogen, which minimized damage and reconfiguration at the cross-sectional surface. Due to aggregation, a common issue for nanoparticle dispersions, small CNP clusters with sizes ranging from several to tens of microns appear in the SEM image instead of the ~ 100 nm individual particles. For example, in Figure 5-2 (b), there is a large aggregated clump of CNP with a size of 20 – 30 μm at the upper-left corner, but most of the clusters are ~ 3 μm along their longest dimension. The CNP clusters are embedded in the PDMS and separated from each other such that they form a discrete distribution in the PDMS matrix regardless of the cluster sizes according to images of multiple spots taken across the entire cross section. Due to structural complexity, it is difficult to spot the CNPs in the foam samples. Considering that merely mechanical blending was applied during the synthetic process, it is estimated that there might be more agglomeration in the composite foam than the composite film with the same CNP concentration, for examples the CNP cluster shown in Figure 5-3 (a). Also, interconnected networks of the CNPs or CNP clusters were not found, indicating that the distribution of the dopant in the foams should be analogous to that of the bulk in Figure 5-2 (b).

Residual salt particles were noticed during the imaging, appearing as regular cubic crystals in the material (see Figure 5-3 (b)). This is attributed to the inevitable existence of closed pores in the

PDMS fabrication process. These completely encapsulated particles are not removed during the leaching process and are uncovered at the cryo-fractured cross-sectional surface prepared for SEM imaging. Interestingly, the residual particles are all less than 10 μm, indicating the incomplete sieving process.

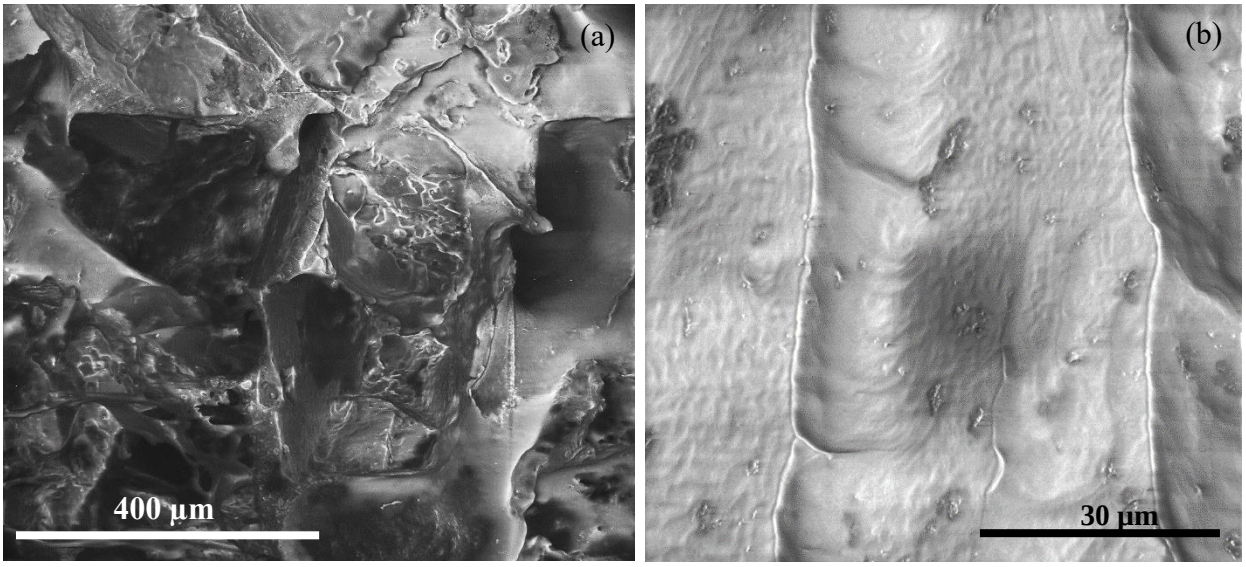

Figure 5-2 SEM image of the cross section of (a) the 5CNP/PDMS-2 foam showing the cubic pores inside; (b) the pristine PDMS with 5 wt% CNP (sample 2, p-5CNP/PMDS-2) showing the CNP distribution at the cross section of the film prepared by a cyro-fracture method.

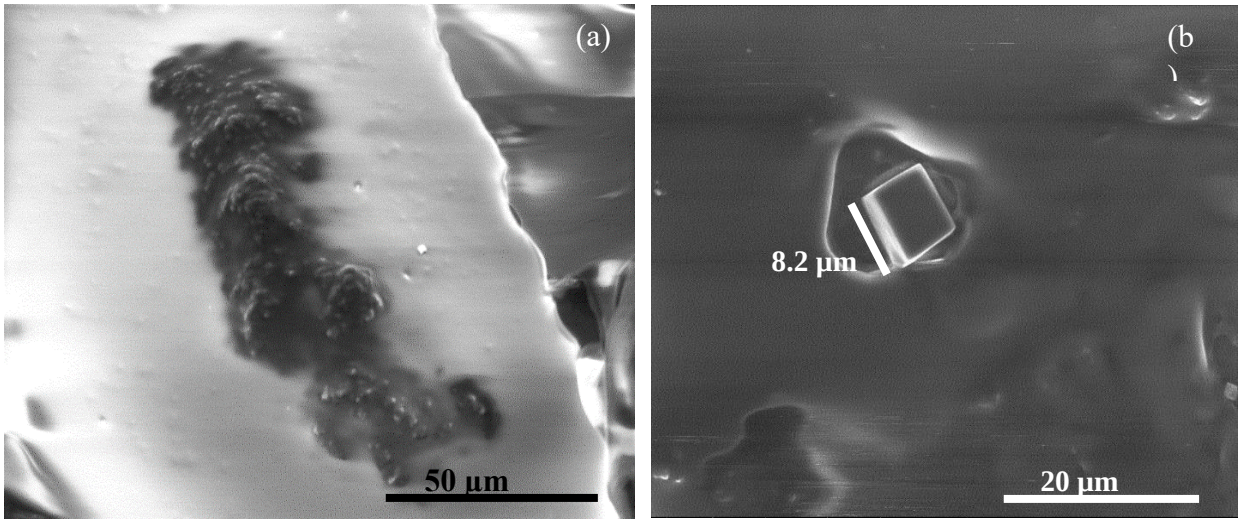

Figure 5-3 SEM image of (a) an isolated CNP cluster in a CNP/PDMS composite foam with a doping concentration of 5 wt% (sample 8, 5CNP/PDMS-2); (b) a single salt crystal remained in the CNP/PDMS foam with an approximate size of 8.2 μm.

5.3. Micro-CT

The CNP/PDMS foams were cut into small pieces (about 4 mm × 4 mm × 2 mm) and scanned with a high-resolution micro-CT system (SKYSCAN 12723D X-ray Microscopy, Bruker) at a voltage of 40 kV and a current of 180 μA with no filter. The sample was rotated over 180 ^{o} in rotation steps of 0.15 ^{o} with an 8 μm voxel size resolution. The micro-CT images are shown in Figure 5-4. The open porosity of the PVA-5CNP/PDMS-2 foam is measured to be 70.73 % rather than the theoretical value (85 %). This is attributed to main two reasons. Firstly, it is expected that the foams contain some closed pores, induced by the complete encapsulation of the salt particles by the CNP/PDMS slurry. Secondly, shrinkage of the foams occurred during the leaching and drying processes which further contributed to the reduction in the volume percentage of the open pores. Residue of salt particles were found in the micro-CT images, although CNPs were not detected due to the small sizes of the CNP clusters.

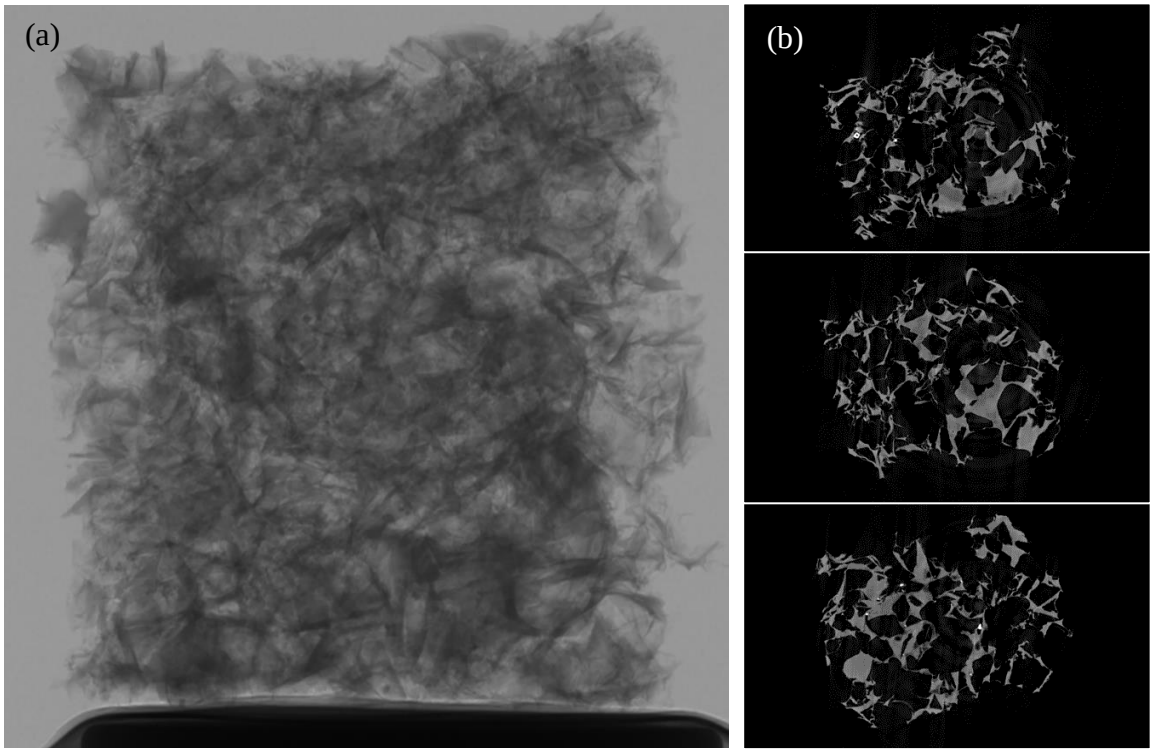

Figure 5-4 Micro-CT images of a small piece of the PVA-5CNP/PDMS-2. (a) Side view of the whole specimen; (b) three example images of cross section.

5.4. Ultraviolet-visible-near infrared Spectrophotometer (UV/Vis/NIR)

The impact of the CNP doping level on the optical properties was investigated by the measurement of the transmissivity and reflectivity of the samples using a UV/Vis/NIR spectrophotometer (Lambda 1050, PerkinElmer Inc., USA) with a 150 mm integrating sphere reflectance accessory at room temperature. The device is equipped with a 3-detector module to cover the entire UV/Vis/NIR range. The integrating sphere collects both the specular and diffuse components of the transmitted and reflected light regardless of the incident angle, ensuring all transmitted and reflected light is accounted for. Reliable data for the total reflectance and transmittance spectra was obtained in the Vis-NIR range (380 – 1600 nm) using a scanning step of 5 nm. The absorption spectra were derived using the relation that the sum of the absorptivity, transmissivity and reflectivity of an objective is 1.

5.4.1. Validation

To validate the reliability of the spectrophotometer used in this work, a pristine PDMS bulk film (sample 1, p-PDMS-2) with a thickness of 2 mm was firstly tested in the range of 380 nm – 1600 nm after baseline correction (Figure 5-5 (a)), and compared with the results reported by Zeranska-Chudek *et al.* using a 0.8 mm-thick pristine PDMS film (see Figure 5-5 (b)) [332]. The resultant spectra of sample 1 indicates almost zero absorption from 380 nm to 1100 nm, in alignment with the generally accepted transparency of pristine PDMS over this spectral range [333]–[335]. Despite slight differences in normalized values caused by thickness variations, three characteristic absorption peaks (or transmittance troughs), mainly due to the higher harmonics of fundamental symmetrical stretching of C-H bonds and their synergy with bending vibration [335], [336], are

observed in the spectra of sample 1 at around 1180 nm, 1395 nm and 1530 nm, which matches perfectly with the results reported by Zeranska-Chudek *et al.* [332].

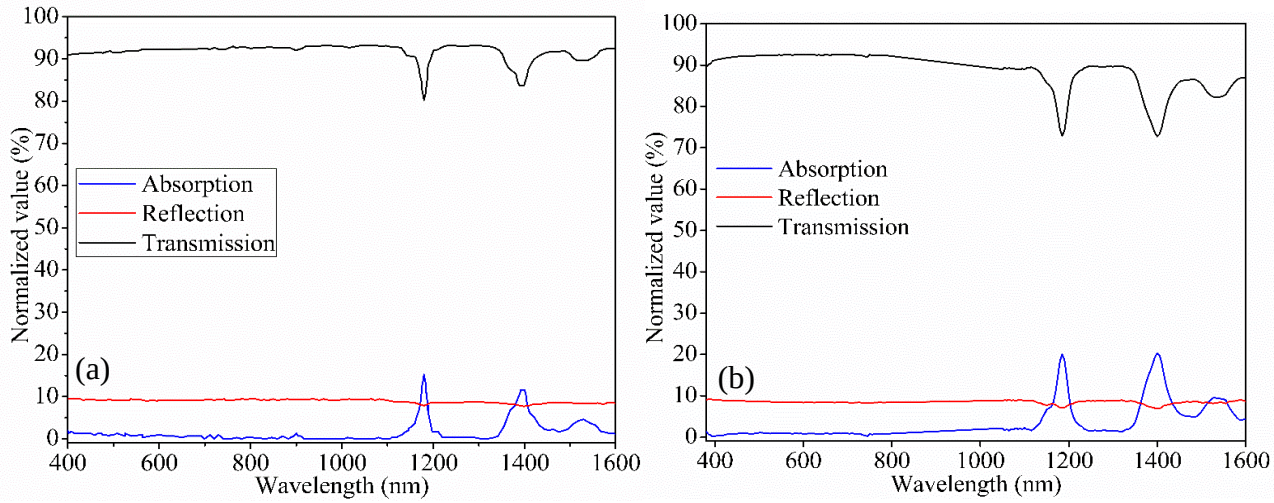

Figure 5-5 The absorbance, reflectance and transmittance spectra of (a) a pristine PDMS film with a thickness of 0.8 mm [332] and (b) sample 1 (p-PDMS-2), a pristine PDMS film fabricated in this work with a thickness of 2 mm.

5.4.2. Influence of porous structures

In this section the influence of the macrostructure on reflectance, transmittance and absorbance is studied by the comparison of the measured spectra of sample 1 and sample 5 (pure PDMS sponge and PDMS-2) as shown in Figure 5-6. The introduction of a large portion of air voids in PDMS does affect its optical properties, which is expressed as a huge reduction of ~ 70 % of its transmittance together with an increase in reflectance by ~ 42 % over the Vis-NIR region. The calculated absorption of incident light is thus enhanced by ~ 28 %, and the sample appearance switches from a transparent bulk film to a white foam. However, the shape and peak locations of the foam spectra are almost identical to those of the pristine bulk, indicating that the bonding status in PDMS polymer is impervious to the introduction of the porous structures via the leaching technique.

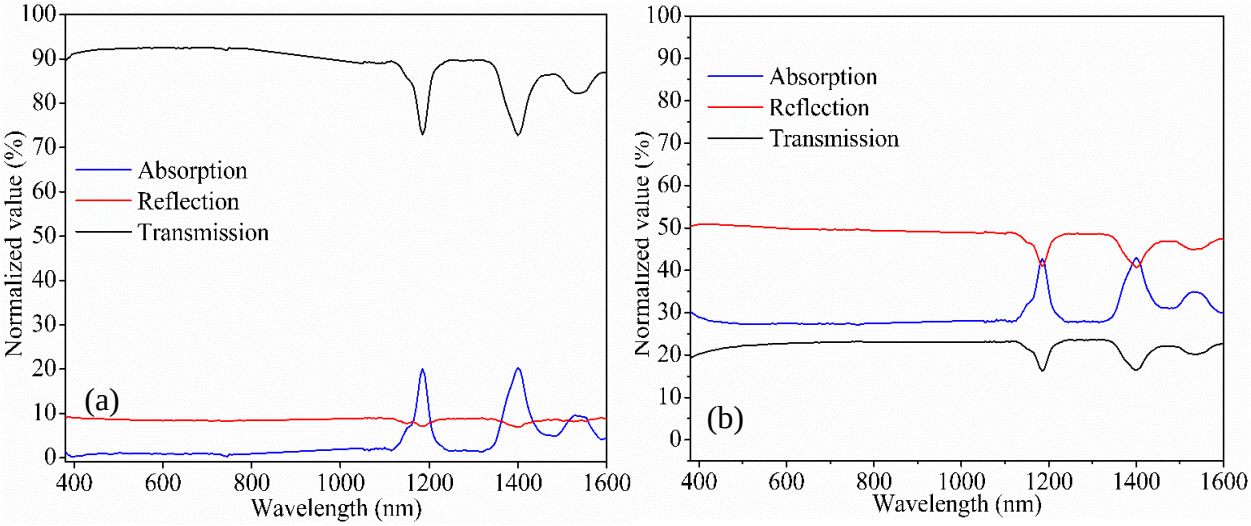

Figure 5-6 The absorbance, reflectance and transmittance spectra of (a) sample 1 (p-PDMS-2, pristine) and (b) sample 5 (PMDS-2, white foam).

5.4.3. CNP concentration study

As for the effect of CNP doping on the optical properties, apparently the addition of the black nanoparticles lowers material clarity. Furthermore, it is expected that higher doping concentrations lead to darker coloring levels. A set of CNP/PDMS foams with differing CNP content were characterized in this section for a quantified description. Figure 5-7 demonstrates the spectra obtained for the involved samples (3, 9, 10, 12, 14 and 17) prepared with different CNP concentrations of 0 wt%, 0.5 wt%, 1 wt%, 5 wt%, 10 wt% and 20 wt%. All samples characterized here are 1 mm thick and were treated with PVA to form a hydrophilic coating. Sample 9 (PVA-0.5CNP/PDMS-1) appears a grey color with the smallest doping content of 0.5 wt%, transmitting over 40 % less light compared with the white PDMS foam (PVA-PDMS-1) while reflecting 30 % less. The decreased transmittance and reflectance is resultant of a significant increase in absorptivity. That is, the absorptivity of Sample 9 (PVA-0.5CNP/PDMS-1) increases to an approximate average value of 87 % in the spectral regime from 380 nm – 1600 nm with a slightly descending value of the absorptivity with increasing wavelength. For CNP loading percentages in

excess of 1 wt%, the absorptivity of these heavily doped samples has little space for further improvement and reaches an absorptive saturation of 96 – 98 % (see Figure 5-8). This high absorptivity value is more than 4 times better than that of the undoped sample (~ 18 %) and is very desirable for photo-thermal applications. Notably, the signature peaks of pure PDMS disappear for all doped samples, showing relatively flat profiles despite insignificant fluctuations.

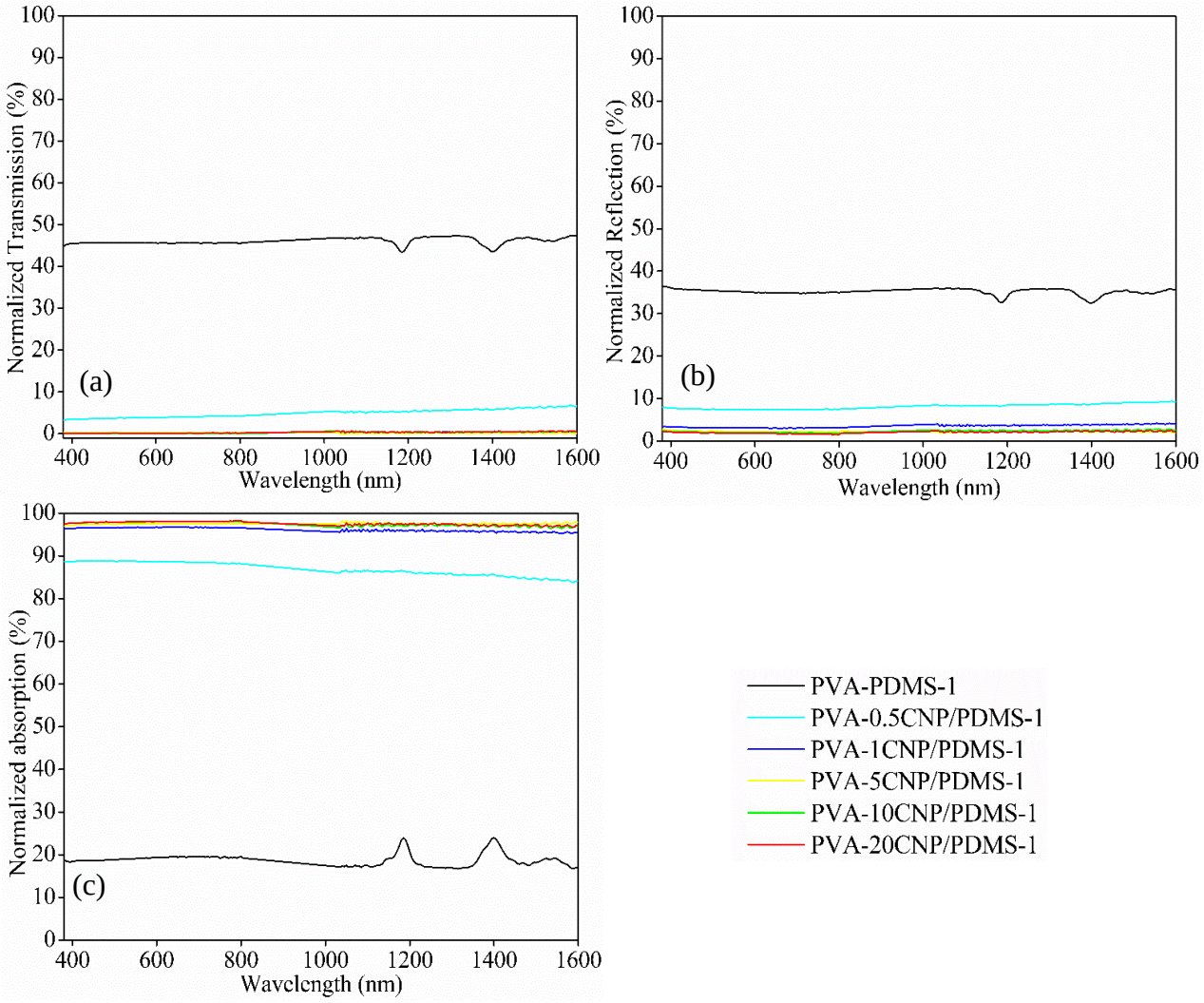

Figure 5-7 The transmittance, reflectance and absorbance spectra of PVA-modified foams with different CNP content of 0 wt% (sample 3, PVA-PDMS-1), 0.5 wt% (sample 9, PVA-0.5CNP/PDMS-1), 1 wt% (sample 10, PVA-1CNP/PDMS-1), 5 wt% (sample 12, PVA-5CNP/PDMS-1), 10 wt% (sample 14, PVA-10CNP/PDMS-1) and 20 wt% (sample 17, PVA-20CNP/PDMS-1). All the samples are of the same thickness of 1 mm.

Since the pristine PDMS is roughly transparent showing extremely low absorbance over the 380 – 1600 nm spectral region, the mechanism with which the PDMS foams interact with incident light is considered to be a joint phenomenon of (1) reflective trapping in the air cavities and (2) Mie scattering within the CNP/PDMS scaffold since the sizes of the clusters are much bigger than the related electromagnetic wavelengths. It can also be concluded that the absorptivity of PDMS polymer can be tuned greatly with only a small amount of CNP inclusions, while the reflectivity is more sensitive to the structural change, that is, the incorporation of the air voids in this work.

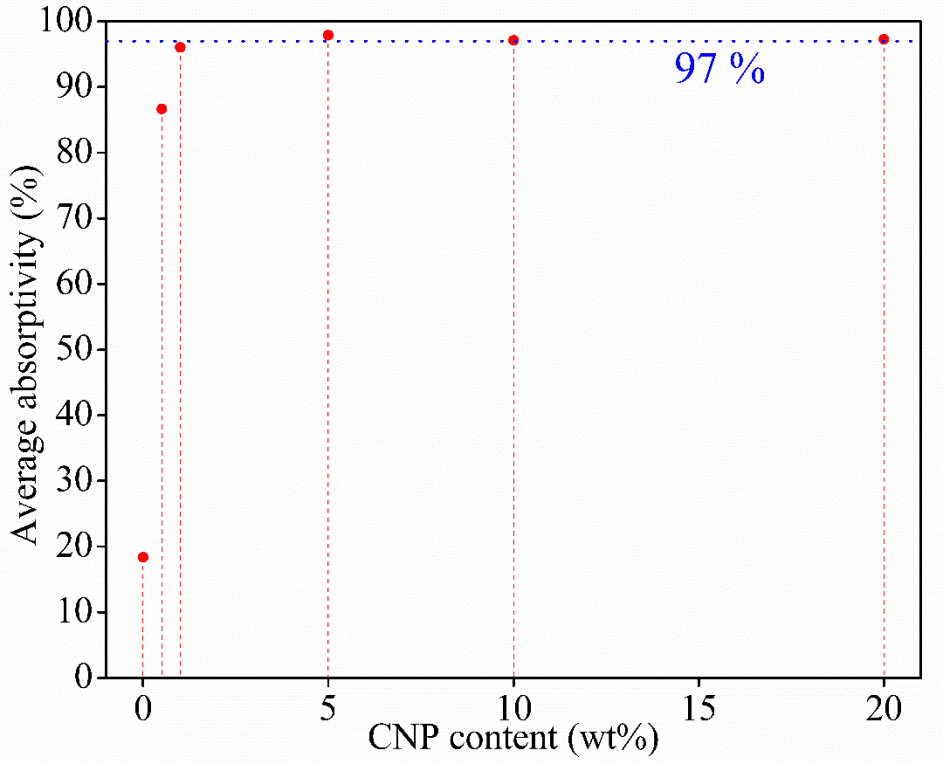

Figure 5-8 The average light absorptivity of the PVA-modified samples with different CNP doping level (0 wt%, 0.5 wt%, 1 wt%, 5 wt%, 10 wt%, and 20 wt%) over the range of 380 nm – 1600 nm. The blue dash line represents an approximate saturation value of the absorptivity.

5.4.4. Thickness study

The effect of the thickness of the foams on their optical properties was also investigated. Explicitly, sample 6 – 8 with different thicknesses (1 mm, 1.5 mm and 2 mm) are characterized in this section. Other sample parameters are controlled to be the same including 5 wt% CNP dopants with 5-layer PVA deposition. As shown in Figure 5-9, the absorption of incident light, which is the most important optical property of the samples, turns out to be comparable for all three samples, which is the plateau value around 97 % mentioned in the previous section. The CNP concentration of 5

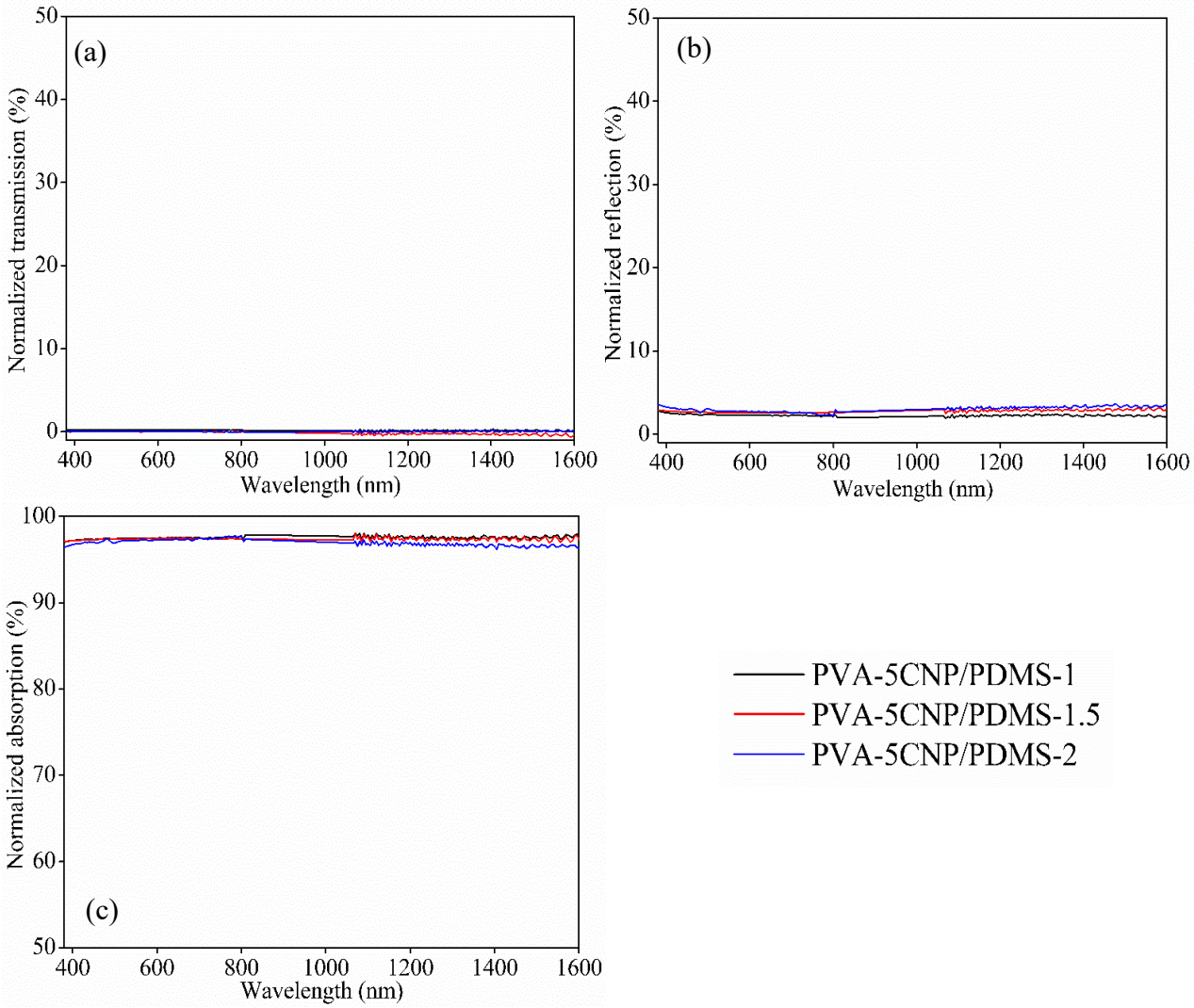

Figure 5-9 The transmittance, reflectance and absorbance spectra of PVA-modified foams with different thicknesses: (a) sample 6 (PVA-5CNP/PDMS-1), 1 mm; (b) sample 7 (PVA-5CNP/PDMS-1.5), 1.5 mm; (c) sample 8 (PVA-5CNP/PDMS-2), 2 mm.

wt% is sufficiently high for the 1 mm-thick composite foam to reach its saturation point for absorption, such that further increasing the thickness does not noticeably further increase absorptivity. Notably, it is possible that an increase in absorptivity with increasing doping concentrations may be observed for samples with lower doping levels (such as < 0.5 wt%) or for samples significantly thinner than 1 mm.

5.4.5. Influence of PVA modification

To check for any alteration in the optical properties that may have been induced by the hydrophilic surface modification of the composite foams, the reflectance and transmittance of sample 8 was measured before and after being subjected to the PVA coating treatment (PVA-5CNP/PDMS-2 and 5CNP/PDMS-2). The results show that after the 5-layers of PVA were deposited, the foam absorptivity increases by only a trivial amount of < 1 %. Since the spectra are relatively flat, the average of the absorptivity is calculated to be 97.1 % and 97.9 % for the coated and uncoated foams, respectively. There is nearly no light transmitted through both black samples, and only a tiny fluctuation in reflection. Thus, it is safe to conclude that the PVA coating does not cause any significant changes in the optical properties of the CNP/PDMS foams despite the bonding relation between the chemical components at the foam surface.

Based on the analysis in this section, the absorptivity of samples containing 1 wt% CNP dopant or more exhibit an average absorptivity between 96 % and 98 % over the 380 – 1600 nm spectral region. Moreover, the small influence of PVA treatment on the optical parameters are insignificant and not considered.

5.5. Thermal conductivity

The thermal conductivity of the PDMS, PVA-CNP/PDMS and CNP/PDMS foams were measured using a TCi Thermal Conductivity Analyzer from C-Therm Technologies with a modified transient plane source (MTPS) accessory sensor. The sensor contains a spiral heating element with a diameter of about 12.3 mm, which produces a small amount of thermal energy over a short duration (~ 1 – 3 s) with a known current and is transferred towards the sample on the top through a one-dimensional path. The interface between the sample and the sensor is thus heated up, causing voltage alternation of the sensor coil. Then the thermal conductivity of the samples is calculable using the applied current and the collected voltage signal. A small weight of 30.72 g was put on the top of the foams to ensure good contact between the foams and the sensor. The test was conducted by measuring three positions on the foam surface under ambient temperature (24.4 – 24.6 ^{o}C). Interestingly, the readings show that the thermal conductivity of all foams falls in a narrow range of 0.039 – 0.045 W/m·K, which is one order of magnitude lower than that of the pristine PDMS (0.27 W/m·K) and close to that of ambient air (0.026 W/m·K). Furthermore, this also shows that the foams are much more thermally resistive than water (~ 0.6 W/m·K) when measured in the air. However, when these foams were placed at the water surface in the evaporation tests, water filled part of the pores inside the foams especially those with hydrophilic coatings. This caused a change in thermal conductivity of the structure and will be discussed in Chapter 6.

Although carbon nanofillers have been used a lot in polymers to enhance their thermal and electrical conductivity, only selected types have proven to be effective such as SWCNTs, MWCNTs and carbon nanofibers [331], [337], [338]. One crucial feature of these fillers is their large aspect ratio, which is preferable in network construction to create continuous pathways. In

this work the cemented CNP agglomerates are dispersed in the PDMS substrates and do not form interconnected structures, as revealed by the filler distribution in the SEM images. Even the composite foams are very thermally resistive because the incoming heat flow is likely to be cut off either by the polymer matrix or the air voids inside the material. This means that the as-measured thermal conductivity of the samples is greatly dependent on the properties of PDMS and the air. Consequently, the addition of CNP has little or no effect on the thermal conductivity and neither does the PVA surface treatment. Only the structural modification where the pores are introduced determines the thermal conductivity.

5.6. Wettability

The wettability of a solid surface depends strongly on free surface energy, and is usually estimated by the contact angle (CA) which refers to the angle between the solid-liquid contact line (baseline) and the tangent of the droplet [202], [339]. The pristine PDMS is reported to be very hydrophobic and to have poor wettability with a 100 – 112 ^{o} static CA with water in the literature [294]. However, the CA of a practical solid surface is often a range rather than an exact value, especially for rough and heterogeneous surfaces such as that of the highly porous samples in this work. In this case the upper and lower limit of this range, namely the advancing and receding contact angle (ACA and RCA), will be used to describe the wettability and can be determined by a dynamic process of adding and removing a fluid droplet on the surface [340].

Samples consisting of 5 wt% CNP with and without PVA modification (PVA-5CNP/PDMS and 5CNP/PDMS) were tested for their ACAs and RCAs by a drop shape analyzer (KRÜSS, DSA 100E, Germany) in ambient air to characterize the influence of PVA treatment on the wetting behavior of these foams. Since wettability depends on surface properties and is not related to the

bulk, the thicknesses of the samples are not specified in this section. After fabrication, the samples were stored in vacuum to isolate contamination/humidity and blown with compressed refrigerant cleaner (Dust-off, containing difluoroethane) before the experiments. A sessile drop method was applied for all measurements, where a deionized (DI) water drop with a fixed volume of 15 µL was carefully deposited onto the foam surface using an I-shape needle at a constant rate of 2 µL/s. The angle grew to a maximum and was recorded as the ACA. Then as the droplet was removed, a point was reached when the water-foam contact line, a line observed from the side view representing the contact area of the liquid and the solid, started shrinking and the RCA was measured. The whole process was completed within 15 s to prevent inaccuracy caused by water evaporation. Measurements were performed at three different spots on each sample surface to minimize experimental uncertainty. All the experiments were conducted within a short period of time to eliminate variation caused by the environmental factors (room temperature 26 ^{o}C ± 0.2 ^{o}C, relative humidity 20 % ± 5 %). The CAs were calculated from the acquired images by the KRÜSS ADVANCE software.

Examples of tests taken at one location of both PVA-5CNP/PDMS and 5CNP/PDMS foams are given in Figure 5-10. The composite foam without PVA modification (5CNP/PDMS) shows an ACA ranging from 129.4 ^{o} to 133 ^{o} and an RCA between 78 ^{o} and 79.8 ^{o} (Figure 5-10 (a-d)). On the other hand, the ACA of the same foam coated with PVA is measured to be 99.9 ^{o} – 109.3 ^{o}, which does not differ much from the former one (see Figure 5-10 (f)). However, by comparing the receding stage, it is apparent that the air-water-foam triple-phase contact points (the end points of the contact lines marked by the yellow circles in Figure 5-10 (e) and (f)) were pinned at the interface during the removal of the droplet revealing a fixed length of L_2 of the contact line (red line), unlike the reduction of L_1 observed for the other sample (Figure 5-10 (c) and (d)). As a result,

it was very difficult to determine the RCA. This means that the RCA is very small (< 10 °) and is a manifestation of the strong adhesion of the PVA-CNP/PDMS foam surface to water.

The measured CA values differ from spot to spot but are within 10 ° for the same sample, which can be explained with the high surface roughness and heterogeneity of the foams induced by the porous structures. The wettability of the CNP/PDMS foams are improved with no doubt after the 5-layer PVA deposition which is supported by the fact that the CAs decreased after the treatment was applied, especially the RCAs. It was also observed that when placed at the air-water interface, the surface of 5CNP/PDMS-2 stayed completely dry for a long time (> 1 hour), while the upper

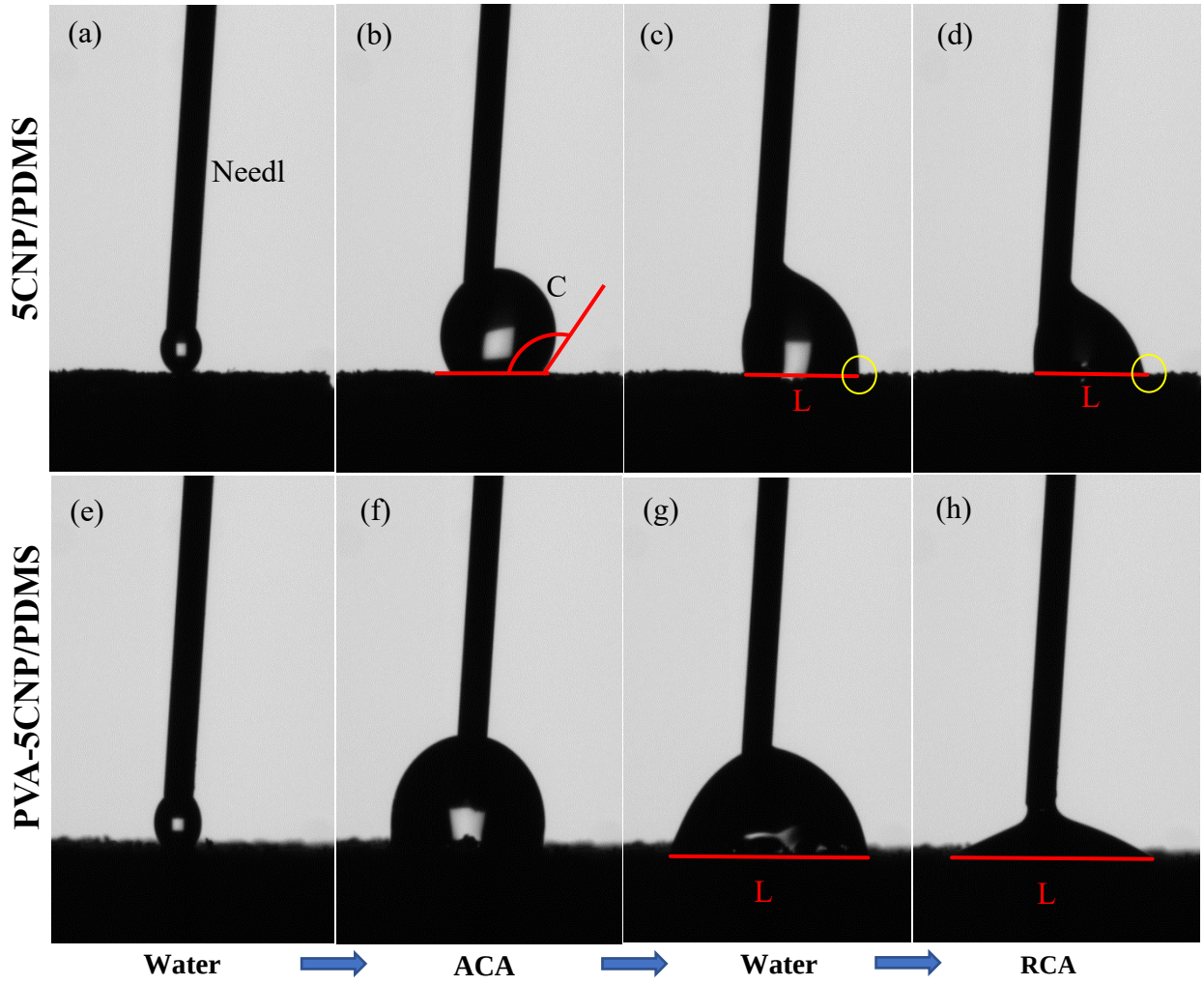

Figure 5-10 Dynamic contact angle measurement of 5CNP/PDMS-2 (a-d) and PVA-5CNP/PDMS-2 (e-h).

surface of the PVA-5CNP/PDMS-2 wetted quickly but the foam still floated on the water (see Figure 5-11).

From the results of the material characterization, it can be clearly seen that the as-fabricated PVA-CNP/PDMS composite foams had all the designed properties as an interfacial solat receiver: high absortivity of solar radiation (~ 97 %), low thermal-conducivity (0.04 W/m·K measured in air), reliable floatability and high open-porosity (70 %) for water repenishment. Their photo-thermal perfoamance was then measured in solar evaporation tests and the results are presented in Chapter 6.

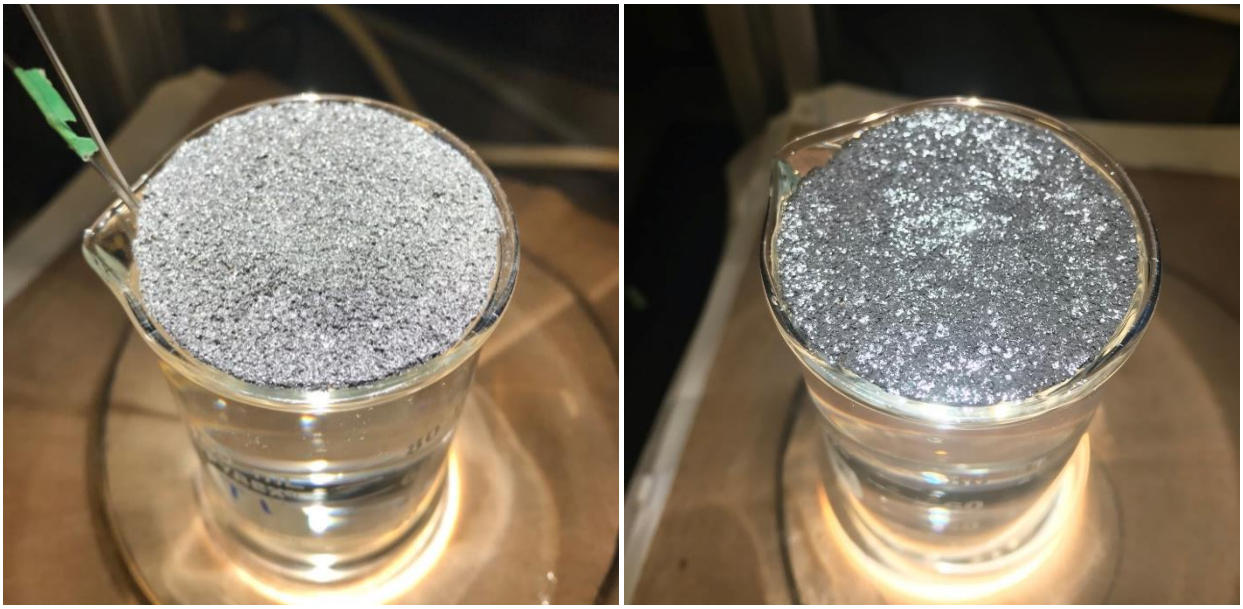

Figure 5-11 Digital images of sample 8 (5CNP/PDMS-2) when tested at the air-water interface. (a) Original hydrophobic foam without PVA coatings, showing a dry surface; (b) the same foam deposited with 5 layers of PVA which was totally wetted by the water underneath.

6. Solar-Heating Application of CNP/PDMS Foams - Evaporation Tests

The as-fabricated foams were tested in an evaporation system under simulated solar irradiance to evaluate their photo-thermal performance by comparing measured evaporation rates achieved using samples with different wettability (with or without a hydrophilic coating), thicknesses and doping concentrations.

6.1. Experimental setup

The schematic illustration and digital images of the solar evaporation system is in the drawing in Figure 6-1 and Figure 6-2, which comprises the following parts:

(1) Water reservoir

A glass beaker with a volume of 100 mL was used as a small-scale water reservoir. The diameter of its opening area is about 45 mm.

(2) Solar simulator – light source

A solar simulator (Sciencetech SF300-C) provides simulated solar radiation from a xenon arc lamp directly above the beaker as the only energy source in the system. The device is equipped with an air mass 1.5G filter and offers aligned radiation with a spectrum analogous to natural sunlight. The beam is circular in shape with a diameter of 50.8 mm, enough to cover the whole beaker surface.

(3) Weighing scale – weight loss

An Adventurer® Precision scale (model AX423, Ohaus) was used to continuously monitor mass change during the experiments. The maximum capacity of the scale is 420 g, which is enough to carry the relatively heavy beaker/water/foam system. The accuracy of the scale

goes down to 1 mg to ensure adequate precision of the mass measurements. The scale can communicate to the computer via a USB connection.

(4) K-type thermal couple (TC) – temperature

Two K-type thermocouples from OMEGA were bent as necessary and placed at two positions in the water: right at the lower surface of the open-cellular foams and 6.5 cm below that lower surface to measure and record the temperature change over the duration of the experiment (see Figure 6-1 (b)).

(5) Data logger

An eight-channel OctTemp data logger (MagdeTech) was used for data acquisition with a resolution of 0.1 ^{o}C and an accuracy of ± 0.5 ^{o}C. The device was mated with the K-type TCs and connected with the computer for real-time data monitoring.

(6) Infrared (IR) camera – temperature

A high-resolution infrared camera (A6751sc, FLIR) with an excellent sensitivity (< 20 mK) was employed to record the temperature profile of the top surface of the samples during the evaporation tests. The infrared camera can detect light radiation with wavelengths from 3 to 5 μm using a cooled Indium Antimonide detector and can measure temperature ranges of -20 – 350 ^{o}C. The recoding resolution was set as 640 × 512 pixels with an image frame rate of 20/s. The temperatures were analyzed and exported using FLIR ResearchIR software, and the ambient temperature and humidity was logged to account for environmental effects.

Considering space restrictions (position of the solar simulator and volume of the camera itself), the IR camera had to be placed at a tilted angle instead of vertically above the surface being measured. Furthermore, for the purpose of noise control, signals of direct reflection

should be avoided, which imposed further limitation on the possible position of the IR camera. After a couple of trials, the IR camera was eventually set 610 mm away from the sample surface at an angle of about 45 ^{o} on a tripod and the camera remained in this position for all the evaporation tests. Before initiating the actual experiments, the camera was also calibrated using an OMEGA K-type TC.

For the accuracy of the temperature readings from the IR analysis, the emissivity of the open-cellular foams needs to be determined before the experiments. A blackbody (accessory of the IR camera) was used as an external correction reference with an emissivity of around 1. Specifically, a black open-cellular foam sample and the blackbody reference were heated in an oven to the same temperature of 45 ^{o}C for more than 10 min, and then immediately measured together using the IR camera at a 45 ^{o} angle. The emissivity of the black open-cellular foams could be calculated with the FLIR ResearchIR software using the known blackbody emissivity and the actual object temperature based on the Stefan-Boltzmann theory stating that the radiant power of any object is proportional to its emissivity and the fourth power of its temperature. The measured emissivity of all the CNP/PDMS foams is around 0.7 regardless of the foam thickness and different treatments that were applied to the foams. It is assumed that the emissivity of the sample stays constant within the operating temperature (up to 80 ^{o}C) and measured spectral range (3 – 5 μm).

(7) Power meter – light intensity

A power meter was purchased from Thorlabs (model PM100D) with a thermopile-based sensor (S401C). The sensor detects the power or irradiance of the incident light with an input aperture of Ø9 mm with a fast response time of 1.1 s. It shows high absorbance

(around 99 %) over a broad spectral range from 0.19 to 10.6 μm, independent of the incident angle. The resolution can reach as low as 1 μW with an uncertainty of ± 5 %.

(8) Humidity meter – relative humidity

A digital hygrometer (TP-55, ThermoPro) was used to log relative humidity of the ambient environment.

For the solar evaporation experiments, each open-cellular foam sample was placed at the top surface of the DI water and floated perfectly at the air-water interface, 110 mm underneath the solar simulator. Then the simulator was turned on for a duration of 30 min to provide simulated solar energy, during which time the TCs and IR camera were engaged to record the corresponding temperature change. The balance was set to monitor the weight loss of the beaker/water/foam automatically by taking one reading per minute as the water evaporated to the air. Every involved sample underwent at least three experiments and the average of the collected data was calculated

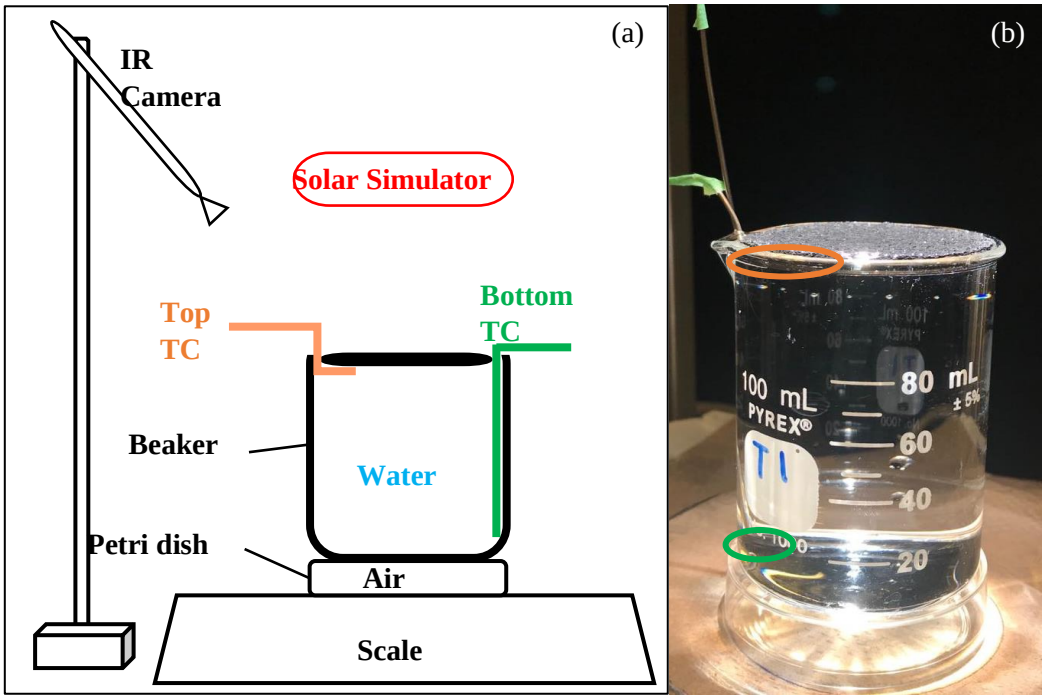

Figure 6-1 (a) Schematic illustration of the setup of the solar evaporation system. (b) Digital image of the beaker part in the system marked with the positions of the TCs (orange and green circles).

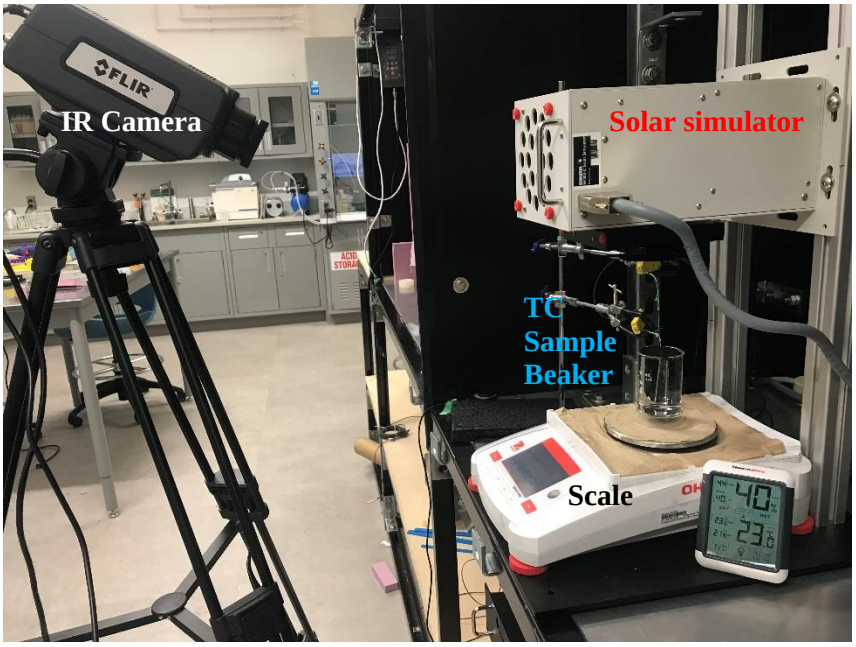

Figure 6-2 Digital image of the setup of the evaporation system.

and used in the analysis. The samples were thoroughly dried at 50 ^{o}C after the experiments. Dark experiments were also conducted with the same conditions in the absence of the simulated solar radiation.

To achieve a fixed energy input for all experiments, the distance between the upper surface of the foams and the lens of the solar simulator should be unchanged. This was done by adjusting the amount of water filled to the beaker to locate the upper surface at the same position regardless of the thicknesses of the samples. Since the foams have relatively small volumes, this adjustment of the water amount (< 2 mL) is too minor to cause a difference in the vaporization processes. Furthermore, to minimize the evaporation-induced position change of the foams, the experiments were conducted for a limited duration of 30 min to control the water loss (< 1.2 g), so that the drop of the foam surface was negligible. The foams were sized into a circular shape with a diameter of 45 mm to cover the entire water surface at the top of the beaker. A plastic petri dish was inserted between the beaker and the weighing scale to create a thermal-resistive air layer for heat loss

minimization. The metal plate of the scale was covered with brown paper towel for two main purposes: to reduce light reflection that contributes to noise in the IR camera measurements, and to prevent the metallic plate from generating heat that could transfer to the water in the beaker during experiments. The TCs were not in physical contact with the beaker or the samples to avoid erroneous weight measurements that could contribute to false measurements of evaporative weight losses.

6.2. Data analysis

The average evaporation rate ($\dot{m}$) achieved by the system was calculated by the following equation:

$$\dot{m} = \frac{\Delta m_t}{t} \tag{12}$$

where Δm_t denotes the total weight loss, that is, the difference between the weight measured once the solar simulator was turned on at the beginning of the test and 30 min later when it was turned off, and t represents the lighting duration, which is 30 min for all experiments.

The overall energy conversion efficiency (η) was estimated as the ratio of the thermal energy harvested for the evaporation and the total solar energy input. The formula is:

$$\eta = \frac{\Delta m_n h_{fg} + \Delta m_n C \Delta T}{a\, I\, t} \tag{13}$$

where Δm_n is calculated by subtracting the weight change of the dark tests from Δm_t using the same sample and is thus called the net weight loss. ΔT denotes the temperature rise of the liquid water from its initial temperature (20 ^{o}C) to the assumed vaporization point (45 ^{o}C). h_{fg} (2,400 kJ/kg) is the latent heat of water at 45 ^{o}C, representing the amount of energy required for the liquid-gas phase change. C (4.2 kJ/kg·K) is the heat capacity of water. a refers to the surface area of the

foam samples and can be calculated using the constant diameter (45 mm). *I* is the intensity of the simulated solar radiation, which was determined by taking 30-minute light intensity measurements with the powermeter everyday. As shown in Figure 6-3, the actual intensity fluctuated over the 50-day period ranging from 800 to 900 W/m^2 showing no obvious descending or ascending trend. Hence, the average light intensity measured over the 50-day period (≈ 850 W/m^2) was used as the solar intensity in the efficiency calculation.

For each sample, the evaporation test was repeated at least three times with the same experimental settings and so was the control test in order to remove contingency. The standard deviations of all the experiments is less than 5 %, revealing good reproducibility and reliability of the results.

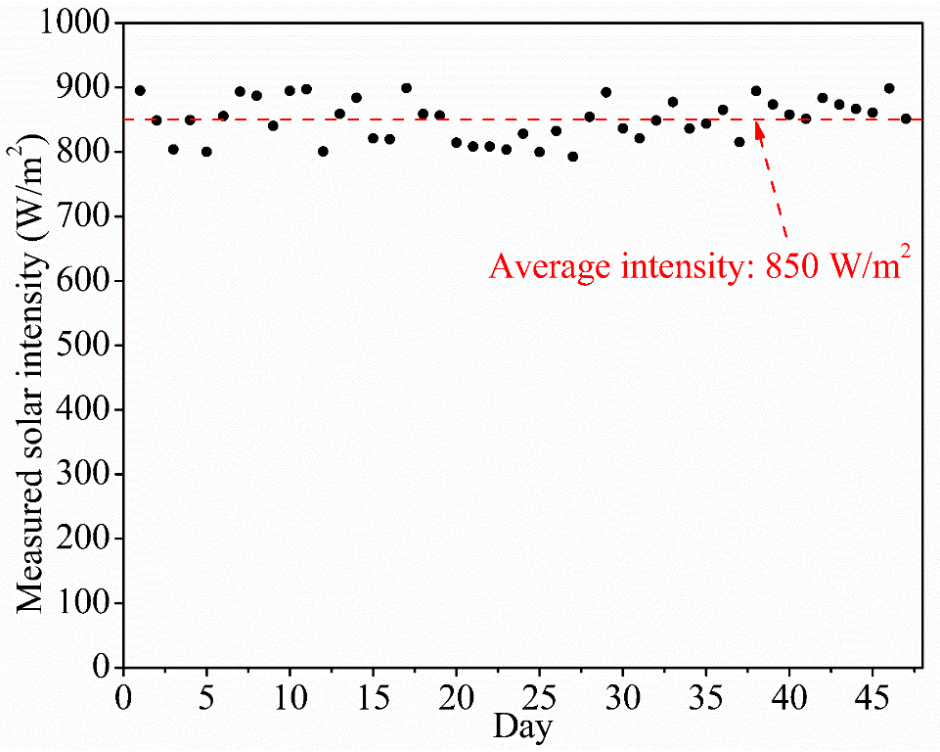

Figure 6-3 Actual intensity of the simulated solar radiation measured using the powermeter in 50 days.

6.3. Effect of foam thickness and wettability

To examine the influence of the thickness and the wettability of the open-cellular foam samples on their photo-thermal performance, samples 6 – 8 with and without PVA coating were tested in the evaporation system and are listed in Table 6-1 for comparison. Control tests were performed in the absence of the CNP/PDMS composite foams. Two kinds of experiments were carried out for all samples – in the dark and under the simulated solar radiation.

Table 6-1 Samples involved in the study of the effect of the foam thickness and wettability on their photo-thermal properties.

Sample name	Thickness (mm)	PVA modification	CNP content
PVA-5CNP/PDMS-1	1	Yes	5 wt%
PVA-5CNP/PDMS-1.5	1.5		
PVA-5CNP/PDMS-2	2		
5CNP/PDMS-1	1	No	
5CNP/PDMS-1.5	1.5		
5CNP/PDMS-2	2		

6.3.1. Evaporation rate and efficiency

The mass change of the water was obtained directly from the scale measurement and plotted versus time in Figure 6-4. The weight loss curves exhibit a similar convex shape in all cases, indicating that the water evaporation in the system gradually accelerated as incoming light energy accumulated. The difference of the slope becomes obvious shortly after the exposure to the radiation, which is a sign of varied rates of vaporization. The measured mass change is rather small (mostly less than 1 g) due to the dimension of the system and the short illumination duration.

The average evaporation rate per unit surface area was derived as discussed in the previous section and shown below. Figure 6-5 (a) demonstrates the average rates of the evaporation experiments

conducted without light. In the dark environment, DI water evaporated more slowly when 5CNP/PDMS foams (thickness = 1, 1.5 and 2 mm) were placed on top of the air water interface as compared to the control test wherein no samples were involved at the water surface (blue line, 0.26 kg/m^2·h). All the 5CNP/PDMS foams repelled water and its upper surface was dry during the evaporation tests because of the non-wettable property of PDMS and air voids formed and blocked the diffusive movement of water molecules towards the air. The thicker the foam is, the greater the obstacle for the evaporation process. As can be seen in Figure 6-5 (a), a 2 mm-thick composite foam in the evaporation system leads to an average measured evaporation rate of 0.15 kg/m^2·h, which is almost comparable with the evaporation rate measured for the 1.5 mm thick sample but is 28 % lower than the evaporation rate measured using the 1 mm thick foam.

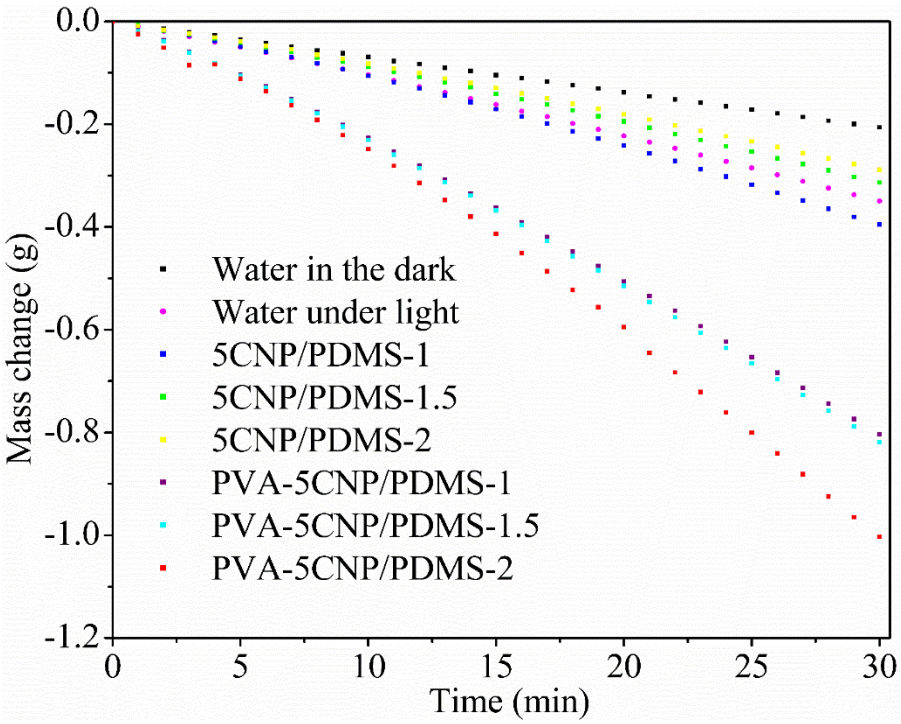

Figure 6-4 Mass change of the water during the 30 min evaporation experiments with samples listed in Table 4 as well as the control test without any samples.

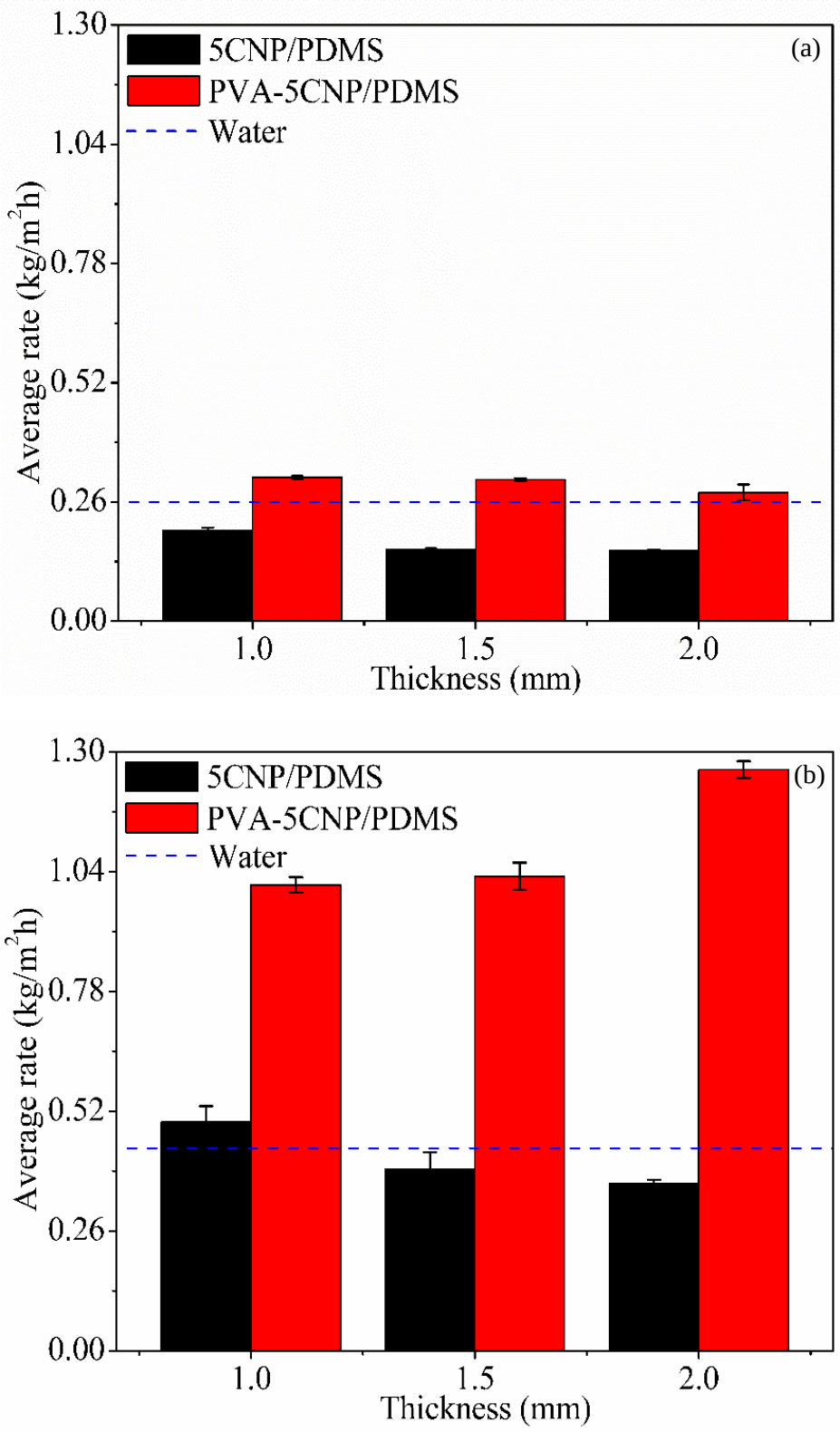

Figure 6-5 The average evaporation rate of 5CNP/PDMS and PVA-5CNP/PDMS foams with thicknesses of 1 mm, 1.5 mm and 2 mm conducted (a) in the dark and (b) under 850 W/m^2 illumination within 30 min.

Unlike the hydrophobic foams, the PVA-5CNP/PDMS samples with PVA modification exhibit good wettability and were completely wetted while floating at the air-water interface. A thin liquid layer formed on the upper surface of the foam, allowing direct diffusion of the vapor to the atmosphere. Thus, the average evaporation rate over PVA-5CNP/PDMS-1 surpasses the control test by about 20 % due to the PVA treatment, although the evaporation rate over PVA-5CNP/PDMS-2 (0.28 $kg/m^2 \cdot h$) is just slightly over the control test. This trend wherein the evaporation rates over the PVA treated samples decreases with increasing thickness is attributed to the non-uniformity of the PVA coating. Although the whole foam is immersed in the PVA solution during the modification procedure, only the surface exposed to the oxygen plasma and several nanometers below is able to bond tightly with the polar groups on PVA chains, whereas the other parts of the foam were not as hydrophilic as the upper surface (but still have some degree of increased wettability). In addition, during the plasmonic treatment, the upper and lower surfaces were more exposed to the plasma which made them more activated than the wall of the pores inside the foams and formed stronger bonds with PVA. Hence, it is assumed that the body of the foams are less hydrophilic than the surfaces, which provides a weaker force to drive water upwards through the foams. Thus, the evaporation will slow once the transfer pathway of water is lengthened by larger foam thickness.

Generally, the water evaporates slowly in the dark. But this situation is changed when the simulated solar radiation is included in the system. As shown in Figure 6-5 (b), the hydrophobic foams work better when subjected to the solar-simulated radiation and the vaporization process is accelerated by more than 100 % compared to when these samples are tested in the dark. The negative correlation between evaporation rate and sample thickness for the 5CNP/PDMS samples remains unchanged and the evaporation rates for the two thicker foams is still less than that of the

control test, wherein the water surface is bare, due to the poor water transportation. On the contrary, the PVA-5CNP/PDMS samples exhibit a reversed tendency in comparison to their hydrophobic counterpart, and the larger thickness becomes an advantage, which is attributed to a collective effect of the wettability and the thermal conductivity of these foams. The improved interaction with water provides continuous supply to the upper surface where most of the heat energy is generated from the absorbed light. Although the thermal conductivity of the foams is subjected to changes in water which will be further discussed in Section 6.3.2, it is still supposed to be lower than water and will confine the heat in a limited volume near the air-water interface, and this confinement is strengthened with the expanded depth of the thermal-resistive structure, or the increasing thickness of the foams. Notably, an average vaporization rate of 1.26 $kg/m^2 \cdot h$ is achieved through the employment of the thickest PVA-5CNP/PDMS-2 foam at the air-water interface, showing an enhancement of nearly 24 % in comparison to the evaporation rates achieved while testing PVA-5CNP/PDMS-1. Notably, these results are in good consistency with the numerical analysis result in Chapter 3. This remarkable evaporation rate is also 87 % higher than the control test where the water surface is bare and nearly 2.5 times as fast as the evaporation rate measured for the same foam but without PVA treatment (5CNP/PDMS-2).

The overall evaporation efficiency is calculated for the tests with simulated solar radiation and shown in Figure 6-6. The evaporation rates for the dark tests were subtracted from the rates measured in the light, and the resultant efficiencies are not proportional to the evaporation rate, although they do follow a similar inclination. The thickness of the hydrophobic samples has a negative effect on the overall efficiency which is suppressed below 18 % for the 2 mm thick sample. On the other hand, the system can make use of the received radiation and generate water vapor more efficiently when the PVA treatment had been applied to the black foams to increase their

wettability. The overall efficiency is greatly enhanced from 58 % to 81 % as the thickness of the PVA-treated films is increased from the thinnest 1 mm-thick foam to the thickest one of 2 mm.

6.3.2. Temperature analysis

Temperature is one of the decisive factors of the evaporation process. In this proposed evaporation system, the temperature at certain locations is even more important than others for the evaluation of the thermal processes. For instance, the temperature of the composite foams is related to its photo-thermal energy conversion ability. The temperature of the evaporative layer, normally refers to the layer located at the liquid-gas interface, is apparently linked to the water vaporization rate with the knowledge that hot surfaces are beneficial for driving the liquid-to-vapour phase change.

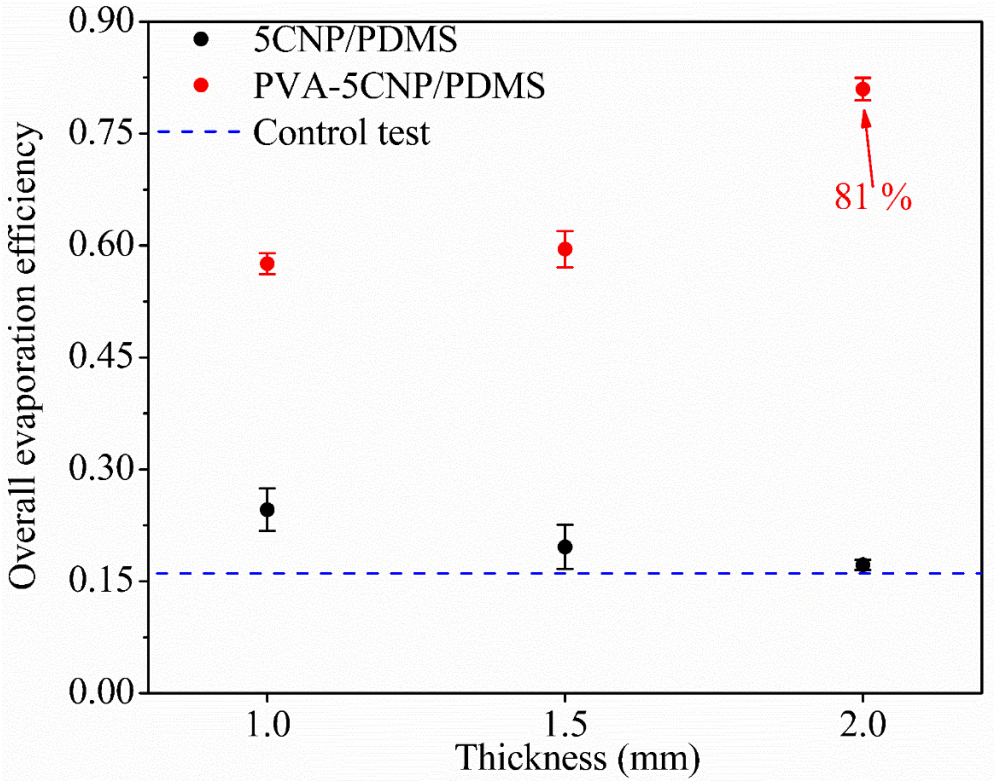

Figure 6-6 The calculated overall efficiency of the evaporation tests using the 5 wt% CNP-doped composite foams with different thickness of 1, 1.5 and 2 mm, both before and after PVA deposition (5CNP/PDMS and PVA-5CNP/PDMS namely). The dash line represents the control test where no sample was in the system.

However, with regards to efficiency, a hotter surface may cause excessive heat losses as well. The temperature difference between the upper and lower surfaces of the composite foams are also crucial as it reflects the heat-confinement ability of these films. Moreover, the temperature difference between the lower surface of the foam and the bulk of the water beneath the film represents the driving factor for the convective heat losses to the bottom of the water reservoir as discussed in the numerical analysis in Chapter 3. From this standpoint, the temperature at the upper and lower surface of the foams along with that in the bulk of water (at the bottom of the beaker) was monitored by the IR camera and TCs for further analysis.

The corresponding infrared images of the system (see Figure 6-7) were captured by the IR camera at several instances over the 0 – 1800 s duration of the evaporation tests. Although the IR thermal analysis was done for all samples listed at the beginning of this section, the 2 mm-thick foam with and without PVA deposition (namely PVA-5CNP/PDMS-2 and 5CNP/PDMS-2) are taken as the representing cases sufficiently embodying all the valuable, common features for explicit description. The quantified surface temperature profiles were extracted for the three PVA-modified foams with variant thicknesses and then plotted together with the readings from the TCs, that is, temperature measured at the lower surface of the foams and 65 mm below the lower surface in the bulk water (see Figure 6-8). Again, the same process was also completed for the three hydrophilic samples, but only one of them (5CNP/PDMS) is shown here as an example due to the great resemblance of these curves. The as-mentioned results were labeled as T_t, T_l and T_b representing the temperature at the top surface of the foam, the lower surface of the foam and bulk of the water, respectively, as shown in Figure 6-8.

The IR images demonstrate the change of T_t, T_l and T_b in the system over the 30 min testing duration and the temperature rise can be seen for both samples due to the exposure to light. The

hydrophobic 5CNP/PDMS-2 foam became hot very fast and stabilized at a temperature of about 72 ^{o}C (red regions in Figure 6-7 (a)) from the original 20 ^{o}C in less than 50 s. The temperature of the PVA-5CNP/PDMS-2 sample rose fast in the first 5 min and then gradually increased at a slower rate, reaching a temperature of about 45 ^{o}C at the last stage of the lighting period. The affected domain, or the heat-up zone, in the water expanded as time elapsed with akin depths, which is evident from the color development in the upper part of the beaker. Both samples are able to utilize the electromagnetic radiation to produce thermal energy due to their photo-thermal property.

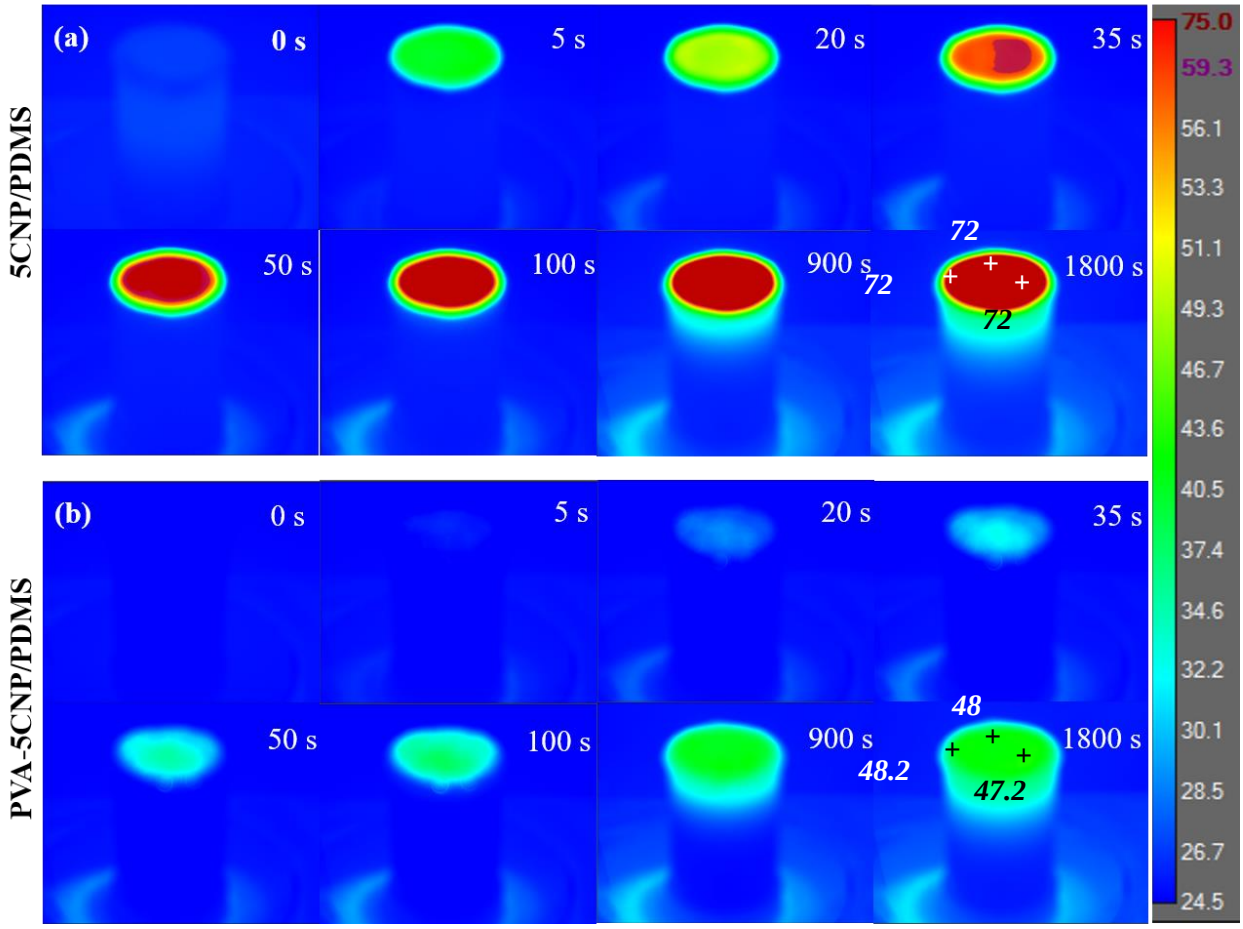

Figure 6-7 The IR images captured through the 30 min evaporation tests using (a) the hydrophobic 5CNP/PDMS-2 and (b) the hydrophilic PVA-5CNP/PDMS-2 composite foam. Three spots were marked with the values of temperature and the end of the tests just before the light was turned off (unit: ^{o}C).

Although the T_t profile of the 5CNP/PDMS-2 and PVA-5CNP/PDMS-2 samples differs a lot, the measured value of T_b for tests conducted on these two samples share similar shape and value; a trivial temperature rise (< 2 ^oC) was observed at the bottom of the beaker within 1800 s. T_l curves for all tests also turn out to be similar, showing a smooth increase of up to 12 ^oC compared with the value of T_l at the beginning of the tests. The absolute values of T_l for the case of the hydrophobic sample (gray area in Figure 6-8) is much lower than T_t, demonstrating a steep temperature drop (> 50 ^oC) across the sample vertically. This is attributed to the low thermal conductivity of the composite foam, which helps trap most of the thermal energy inside the foam. However, since the upper surface of the foam is assumed to float above the water without being wetted, the evaporative layer is not located at the upper surface of the foam, so that the temperature of the evaporative layer surface was cooler than 72 ^oC which was measured at the upper surface. The portion of the foam residing above the air-water interface is also expected to create a blocking effect that hinders vapor escape. Consequently, the water evaporation in the tests with hydrophobic foams are slow.

In the tests of the PVA modified foams, the difference between T_t and T_l remained roughly constant with a moderate value of about 15 ^oC (except for the first several minutes) which resulted from the active water vaporization. Meanwhile a small rise of < 2 ^oC was seen in T_b, showing that the bulk of water was cool throughout the tests. The thinnest foam (1 mm) shows the highest T_l, leading to extra heat losses to the underlying bulk water and thus a lower evaporation rate compared with the 1.5 mm and 2 mm foams. T_b was almost the same for all the tests. The unclear trend of the influence of thickness on T_l and T_b is attributed to the change of the thermal conductivity of the PVA-treated foams when wetted by water. As discussed in Chapter 2, the hydrophilic treatment is applied to the top surface, and the internal surfaces of the foams are less hydrophilic. The perfect floatability

of the PVA-coated foams suggests that a large portion of the pores are not filled with water during the evaporation tests, even though the surfaces are completely wetted. Meanwhile, water can be wicked into some of the open pores to different levels and thus raises the thermal conductivity of the whole structure. A rough estimation of the effective thermal conductivity of this CNP/PDMS/air/water combination can be made using the measured T_l and T_b, the thickness of the foams and equation (11), which indicates that the conduction through the foam (Q_{ci}) equals the sum of the convective and radiative heat losses from the lower surface of the foam down to the water. The results from the estimation predict the conductivity of the foams to be around 0.4 W/m·K when immersed in water, which is higher than the conductivity of dry foams (0.04 W/m·K) and lower than that of water (0.6 W/m·K), and this is reasonable considering the mixed structure.

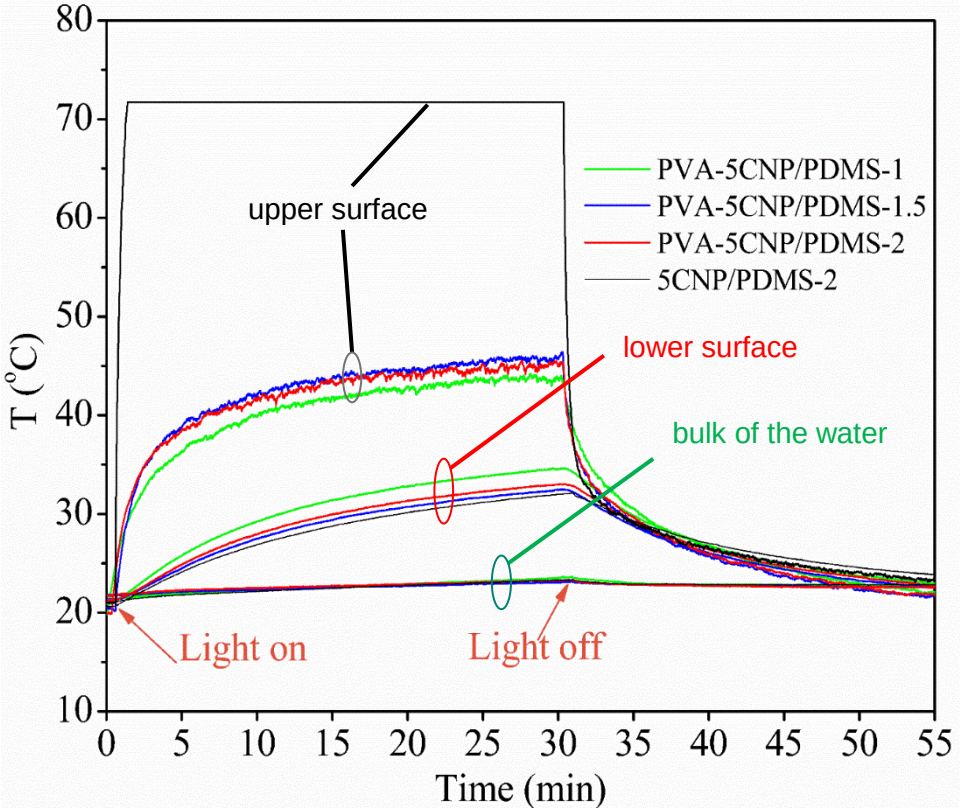

Figure 6-8 Temperature profiles at the upper surface of the composite foams (T_t), at the lower surface of the foams (T_l) and in the bulk water at the bottom of the beaker (T_b). Data were collected using the IR camera and TCs respectively.

In short, the large temperature gradient from the illuminated foam surface all the way down to the bulk of the water is evidence of the effective heat localization induced by the implantation of the composite foams. However, for the hydrophobic foams, despite this impressive temperature difference between the top and the bottom of the samples, evaporation is not properly enhanced due to insufficient diffusion of water to the upper surface of the foams caused by their poor wettability. On the other hand, the temperature of the PVA-treated foams during the evaporation tests is lower than that of their hydrophobic counterparts, but an evaporative layer is created at their top surface where the generated thermal energy is concentrated and the PVA-treated foams wins the competition in terms of water evaporation rate and overall efficiency. It can be concluded that good wettability and continuous water replenishment are very influential for the performance of the CNP/PDMS foams in this proposed study.

6.4. Effect of CNP content

In addition to the study on the foam wettability and thickness, the concentration of embedded CNPs is also explored for its effect on the efficiency of the solar evaporation tests. Samples fabricated with a series of CNP content ranging from 0 wt% to 20 wt% were tested in the same evaporation experiment and their performance was compared. As discussed in Section 6.3, it is important for the foams to be subjected to PVA treatment to increase their wettability, and all foam samples considered in this section underwent PVA treatment to facilitate water evaporation. Furthermore, the thicknesses of the samples considered in this section was controlled to be 1 mm during their synthesis.

The results are shown in Figure 6-9. Firstly, the average evaporation rates outperform the control tests (only water in the system) greatly for all the experiments with composite foams due to the

hydrophilic coating. Interestingly, the undoped pure PDMS sample (PVA-PDMS-1) also brings about a slight improvement in the evaporation rate of about 0.04 kg/m^2·h. Apparently a top evaporative layer is formed at the foam-air interface which is advantageous for vapor diffusion, yet the polymer itself is not a photo-thermal material and suffers from optical energy loss of over 80 % due to significant amounts of transmission and reflection of the incident light. The water evaporates faster for the tests with composite foams with higher doping level, but only within a low concentration range. For example, an enhancement of 0.32 kg/m^2·h is achieved when the CNP content increases from 0 wt% to 0.5 wt% (PVA-0.5CNP/PDMS-1) and the rate can be improved by another 0.31 kg/m^2·h using the foam containing 1 wt% CNP (PVA-1CNP/PDMS-1), which adds up to be an acceleration of 130 % as compared to the undoped sample. However, for CNP concentrations beyond 1 wt%, the solar absorbance of the composite foams becomes saturated according to the optical properties discussed in Chapter 5 such that the additional amount of the carbon dopant has little influence on heat generation. The solar evaporation rate stabilized at approximately 1.05 kg/m^2·h, with a small fluctuation of < 10 %, for samples with CNP concentrations increasing beyond 1 wt%, converting 60.7 % of the solar input into latent heat of water on average. As for the temperature analysis, great similarity is found between the current content study and the former thickness study in Section 6.3 despite of the difference in foam parameters, where the top surface of the composite foams reached around 45 ^{o}C within 30 min of light exposure and the bulk water stayed chill exhibiting an increment of < 1 ^{o}C in good agreement with the heat localization analysis.

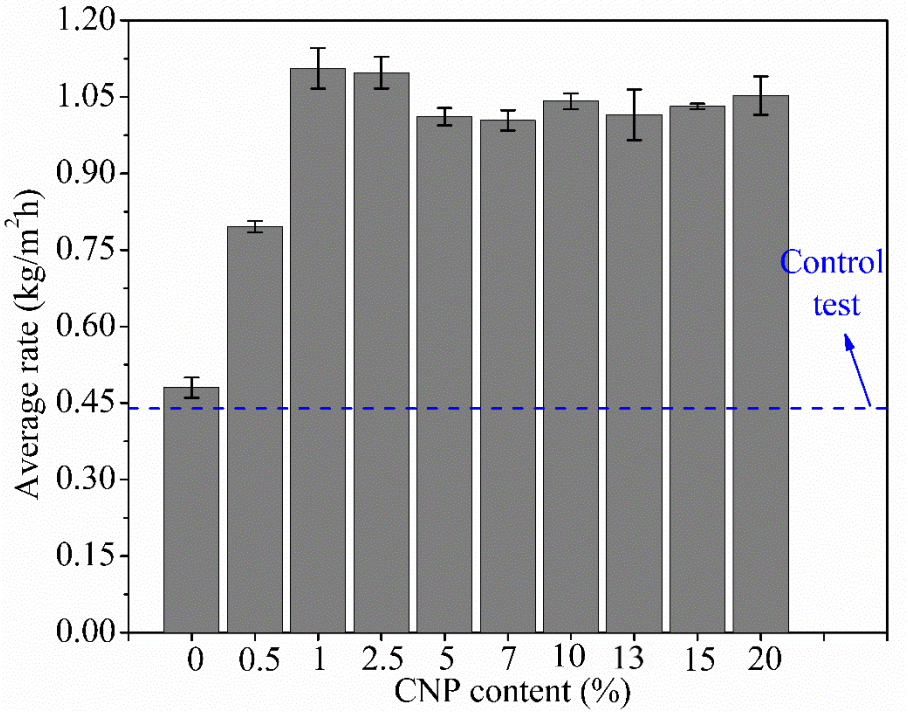

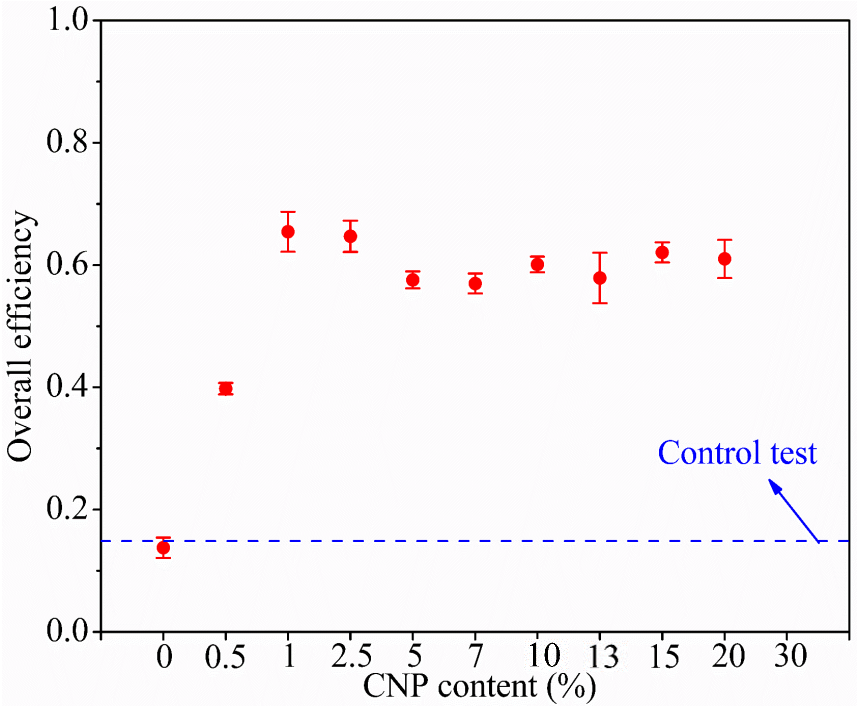

Figure 6-9 The calculated average evaporation rate and corresponding overall efficiency of the experiments using the PVA-treated samples with different CNP content (0, 0.5, 1, 2.5, 5, 7, 10, 13, 15 and 20 wt%).

7. Conclusion and Future Directions

Focusing on the enhancement of the current solar desalination devices, theoretical heat transfer analysis was combined with experimental design and fabrication of CNP/PDMS composite foams to act as an interfacial solar receiver to capture solar energy and accelerate the evaporation process efficiently. The main findings of this work include:

(1) A heat transfer analysis of the effect of an insulation layer in the interfacial solar heating systems

An interfacial solar heating system was modelled to quantify the various heat loss mechanisms occurring during the evaporation process. The results indicate the excellent performance of a hybrid photo-thermal material/insulation structure by reducing the convective heat losses by nearly two orders of magnitudes. Although ideal conditions were considered in the analysis rather than the complicated conditions that may be present in practical cases, this numerical analysis provides strong theoretical results supporting the recommendation to integrate a small insulating structure beneath the interfacial photothermal film to effectively suppress sensible heating in the bulk water. Of course, this insulating layer must be able to provide proper water supply to the evaporative layer, which can be achieved by making it porous.

(2) A facile, reliable process to fabricate open-porous CNP/PDMS composite foams CNP/PDMS composite foams were fabricated by a leaching technique. Both the chemical component and structure of the PDMS were adjusted with bulk and surface modification strategies to tailor the material with desired attributes:

- CNPs were dispersed in the polymer matrix to endow the composite with excellent photo-thermal properties;

- interconnected macro porous structures were introduced into the bulk using salt crystals (> 500 μm) as sacrificial templates for reliable floatability and to provide pathways for water replenishment;
- hydrophilic PVA coatings were deposited onto the composites to improve surface wettability.

Various CNP/PDMS foams with different parameters were obtained by slightly adjusting the synthetic recipe. The sustainable design of the composites was based on bio-compatible and inert materials without causing damage to the environment. The employment of the facile, ecofriendly and low-cost salt-leaching technique in this study is a big advantage over the common methods such as freeze-drying (requiring extreme temperature), supercritical CO_2 foaming (requiring high pressure), carbonization (requiring high temperatures of ~ 1000 ^oC) and lithography (which requires advanced equipment) to create open-pore networks for the solar desalination purposes but still achieve good photo-thermal performance (see Table 9).

(3) Photo-thermal application of carbon-PDMS composite foams

Although carbon-cemented PDMS composites have been widely used for their mechanical flexibility and electrical conductivity, the current work in this thesis focused on their rarely explored photo-thermal properties. Numerous samples were characterized and tested in evaporation experiments with DI water to study the effect of dopant content, thickness and wettability on material properties and performance in solar heating applications.

Only a small amount (no more than 1 wt%) of CNP is needed to saturate the optical absorption to > 96 % across a broad spectral region from 380 to 1600 nm. A vaporization rate of 1.26 $kg/m^2 \cdot h$ was achieved under 0.85 sun (850 W/m^2) irradiance using a 2 mm-thick PVA-modified PDMS foam

containing 5 wt% of CNPs (PVA-5CNP/PDMS-2), featuring an enhancement of 87 % compared with the control test (no samples) as a proof of the excellent photo-thermal performance of the composite foam. Around 81 % of the solar energy input was utilized by the photo-thermal composite foam to contribute to liquid-gas phase change of the water, 65 % higher than the overall energy conversion efficiency of the control test.

In addition, effective heat localization at the air-water interface can be demonstrated by the vertical temperature drop from the illuminated foam surface all the way down to the bulk of the water (> 50 ^{o}C with the hydrophobic foams and > 23 ^{o}C for the hydrophilic ones) which was induced by the lower thermal conductivity of the composite foams compared with water. Good wettability is also essential in terms of lifting the evaporative layer above the upper surface of the foams, such that the foams are not blocking the evaporation process, to allow for continuous water supply. Results from the evaporation tests clearly showed that the PVA-treated foams worked a lot better than the original hydrophobic samples.

Future work should be directed towards optimizing other influential factors to promote energy conversion efficiency. For example, the pore size distribution of the foam is an interesting parameter to investigate because it brings about the analysis of the balance between the diffusive behavior of the water and thermal losses from the photo-thermal material to its surroundings. The effective thermal conductivity throughout the solar receiver when it is immersed in water should also be studied for further optimization to achieve even more effective heat localization. This can be explored by changing the geometry and arrangement of the fillers and pores, or by using more thermal-resistive polymer substrates. Another important factor to consider is the concentration of the incident solar radiation, which is closely related to the temperature of the system and can be studied by the integration of Fresnel lenses to alter solar radiation intensity. Moreover, DI water

should be replaced by seawater, of varying representative compositions, to conduct actual desalination evaluation.

It might be hard to scale-up the as-fabricated CNP/PDMS composite foams to a commercial level with the current research outcome due to the cost of the raw materials. However, what is important is that this work can provide general recommendations for the design of an all-in-one interfacial photo-thermal composite including hydrophilicity, thermal insulation and low density, which can be adapted for other cheaper materials such as recycled paper and cotton fibres for cost-effective manufacture of interfacial solar receivers.

To conclude, the work presented in this thesis demonstrates a feasible method to fabricate an open-pore composite of CNPs and PDMS providing excellent photo-thermal performance and heat conservation to achieve efficient solar-powered evaporation. This study will impose guidance for the design of the next-generation solar distill technologies with high production rates and low energy consumption to pursue the goal of providing clean, sustainable water supply to all in the future.

References

[1] J. Liu *et al.*, “Earth’ s Future Water scarcity assessments in the past , present , and future Earth ’ s Future,” no. July, 2017.

[2] P. BUREK *et al.*, “Water Futures and Solution,” 2016.

[3] UNESCO, *Nature-Based solutions for water: WWDR 2018*. 2018.

[4] W. and W. FAO, IFAD, UNICEF, *The State of Food Security and Nutrition in the World 2018. Building climate resilience for food security and nutrition. Rome, FAO. Licence: CC BY-NC-SA 3.0 IGO*. 2018.

[5] J. Schewe *et al.*, “Multimodel assessment of water scarcity under climate change,” *Proc. Natl. Acad. Sci.*, vol. 111, no. 9, pp. 3245–3250, 2014.

[6] M. M. Mekonnen and A. Y. Hoekstra, “Sustainability: Four billion people facing severe water scarcity,” *Sci. Adv.*, vol. 2, no. 2, pp. 1–4, 2016.

[7] FAO, IFAD, UNICEF, WFP, and WHO, *The State of Food Security and Nutrition in the World 2017: Building Resilience for Peace and Food Security*. 2017.

[8] P. Karimi, W. G. M. Bastiaanssen, and D. Molden, “Water Accounting Plus (WA+) - A water accounting procedure for complex river basins based on satellite measurements,” *Hydrol. Earth Syst. Sci.*, vol. 17, no. 7, pp. 2459–2472, 2013.

[9] K. Onda, J. Lobuglio, and J. Bartram, “Global access to safe water: Accounting for water quality and the resulting impact on MDG progress,” *Int. J. Environ. Res. Public Health*, vol. 9, no. 3, pp. 880–894, 2012.

[10] D. Molden and R. Sakthivadivel, “Water accounting to assess use and productivity of water,” *Int. J. Water Resour. Dev.*, vol. 15, no. 1–2, pp. 55–71, 1999.

[11] M. M. Aldaya, “The Water Footprint Assessment Manual,” *Water Footpr. Assess. Man.*, 2014.

[12] J. L. and C. W. Falkenmark, M, “Macro-scale water scarcity requires micro-scale approaches: Aspects of vulnerability in semi-arid development,” *Nat. Resour. Forum*, no. September 1989, 1989.

[13] A. Leif Ohlsson, B. Appelgren PADRIGU, FAO, “Water and Social Resource Scarcity,” *The Water Page*, 1998. [Online]. Available: https://www.africanwater.org/SoicalResourceScarcity.htm. [Accessed: 27-Apr-2019].

[14] M. S. Islam, T. Oki, S. Kanae, N. Hanasaki, Y. Agata, and K. Yoshimura, “A grid-based assessment of global water scarcity including virtual water trading,” *Integr. Assess. Water Resour. Glob. Chang. A North-South Anal.*, pp. 19–33, 2007.

[15] Food and Agriculture Organization of the United Nations, “Water Stress,” *AQUASTAT*, 2016. [Online]. Available: http://www.fao.org/nr/water/aquastat/didyouknow/index2.stm. [Accessed: 27-Apr-2019].

[16] J. Alcamo, T. Henrichs, T. Rösch, J. Alcamo, T. Henrichs, and T. Rösch, “World Water in 2025: Global modeling and scenario analysis for the World Commission on Water for the 21st Century,” 2000.

[17] I. a. Shiklomanov, “Comprehensive assessment of the freshwater resources of the world,” 1997.

[18] A. K. Gain and C. Giupponi, “A dynamic assessment of water scarcity risk in the Lower Brahmaputra River Basin: An integrated approach,” *Ecol. Indic.*, vol. 48, pp. 120–131, 2015.

[19] J. Alcamo, M. Flörke, and M. Märker, “Future long-term changes in global water resources driven by socio-economic and climatic changes,” *Hydrol. Sci. J.*, vol. 52, no. 2, pp. 247–275, 2007.

[20] M. Pedro-Monzonís, A. Solera, J. Ferrer, T. Estrela, and J. Paredes-Arquiola, “A review of water scarcity and drought indexes in water resources planning and management,” *J. Hydrol.*, vol. 527, pp. 482–493, 2015.

[21] and R. B. David Seckler, Upali Amarasinghe, David Molden, Radhika de Silva, “World Water Demand and Supply, 1990 to 2025 : Scenarios and Issues. International Water Management Institute,” 1990.

[22] C. Sullivan, “‘Calculating a water poverty index.’ World Development, 30: 1195– 1210.,” vol. 30, no. 7, pp. 1195–1210, 2002.

[23] and A. M. G. C.A. Sullivan, J.R. Meigh, “The Water Poverty Index: Development and application at the community scale no. 3 (August 2003): 189-199,” *Nat. Resour. Forum 27,* vol. 27, no. 3, pp. 189–199, 2003.

[24] M. Kummu, P. J. Ward, H. De Moel, and O. Varis, “Is physical water scarcity a new phenomenon? Global assessment of water shortage over the last two millennia,” *Environ. Res. Lett.*, vol. 5, no. 3, 2010.

[25] J. Alcamo *et al.*, “Development and testing of the WaterGAP 2 global model of water use and availability,” *Hydrol. Sci. J.*, vol. 48, no. 3, pp. 317–338, 2003.

[26] X. Cai and M. W. Rosegrant, “Global Water Demand and Supply Projections: Part 1. A Modeling Approach,” *Water Int.*, vol. 27, no. 2, pp. 159–169, 2002.

[27] M. W. Rosegrant, X. Cai, and S. a Cline, “Global Water Outlook to 2025:Averting an Impending Crisis,” vol. 14, no. 2, 2002.

[28] S. Oki, Taikan; Kanae, “Global Hydrological Cycles and World Water Resources,” vol. 313, pp. 1068–1072, 2006.

[29] T. Oki, Y. Agata, S. Kanae, T. Saruhashi, D. Yang, and K. Musiake, “Global Assessment of Current Water Resources Using Total Runoff Integrating Pathways,” *Hydrol. Sci. J.*, vol. 46, no. 6, pp. 983–995, 2001.

[30] M. Falkenmark, “Meeting water requirements of an expanding world population,” *Philos. Trans. R. Soc. B Biol. Sci.*, vol. 352, no. 1356, pp. 929–936, 1997.

[31] M. Falkenmark and J. Rockström, “The New Blue and Green Water Paradigm: Breaking New Ground for Water Resources Planning and Management,” *J. Water Resour. Plan. Manag.*, vol. 132, no. 3, pp. 129–132, 2006.

[32] J. Rockström, M. Falkenmark, L. Karlberg, H. Hoff, S. Rost, and D. Gerten, “Future water availability for global food production: The potential of green water for increasing resilience to global change,” *Water Resour. Res.*, vol. 45, no. 7, pp. 1–16, 2009.

[33] M. M. Mekonnen and A. Y. Hoekstra, “National Water Footprint Accounts the Green, Blue and Grey Water Footprint of Production and Consumption,” vol. 2, no. 47, 2011.

[34] B. M. Fekete, M. Meybeck, R. B. Lammers, and C. J. Vo, “Geomorphometric attributes of the global system of rivers at 30-minute spatial resolution,” *J. Hydrol.*, vol. 237, pp. 17–39, 2000.

[35] A. Y. Hoekstra and M. M. Mekonnen, “The water footprint of humanity,” *Proc. Natl. Acad. Sci.*, vol. 109, no. 9, pp. 3232–3237, 2012.

[36] X. Liang, J. Guo, and L. R. Leung, “Assessment of the effects of spatial resolutions on daily water flux simulations,” *J. Hydrol.*, vol. 298, no. 1–4, pp. 287–310, 2004.

[37] Z. Zeng, J. Liu, and H. H. G. Savenije, “A simple approach to assess water scarcity integrating water quantity and quality,” *Ecol. Indic.*, vol. 34, pp. 441–449, 2013.

[38] Y. Wada, L. P. H. Van Beek, D. Viviroli, H. H. Drr, R. Weingartner, and M. F. P. Bierkens, “Global monthly water stress: 2. Water demand and severity of water stress,” *Water Resour. Res.*, vol. 47, no. 7, pp. 1–17, 2011.

[39] Food and Agriculture Organization of the United Nations, “Water Withdrawal,” *AQUASTAT*, 2016. [Online]. Available: http://www.fao.org/nr/water/aquastat/didyouknow/index2.stm. [Accessed: 27-Apr-2019].

[40] UNECSO, *The United Nations World Water Development Report 4: Managing Water under Uncertainty and Risk*, vol. 1, no. 5. 2012.

[41] UNESCO, *Leaving No One Behind: WWDR 2019*. the United Nations Educational (UNESCO), 2019.

[42] “Beyond Scarcity: Power and Global Water Crices, Human Development Report 2006.PDF,” 2006.

[43] M. Falkenmark and J. Lundqvist, “Towards water security: Political determination and human adaptation crucial,” *Nat. Resour. Forum*, vol. 22, no. 1, pp. 37–51, 1998.

[44] G. Caputo and A. Giaconia, *Membrane technologies for solar-desalination plants*. Woodhead Publishing Limited, 2013.

[45] K. Voss *et al.*, “Quantifying renewable groundwater stress with GRACE,” *Water Resour. Res.*, vol. 51, no. 7, pp. 1–22, 2015.

[46] UNESCO, *Managing Water under Uncertainty and Risk*, vol. 1, no. 4. 2012.

[47] FAO, *Coping with Water Scarcity an Action Framework for Agriculture and Food Security*. 2012.

[48] UNESCO, *The United Nations World Water Development Report 2016: Water and Jobs*. 2016.

[49] OECD, “Development Co-Operation Report 2012: Summary Lessons in linking sustainability and development,” 2012.

[50] IEA, “Energy efficiency Market Report 2016,” 2019.

[51] UNESCO, “The United Nations World Water Development Report 2014: Water and Energy,” 2014.

[52] IPCC, “Global Warming of 1.5 ^{o}C,” 2018.

[53] “Oil Squeeze,” *TIME*, 1979.

[54] U.S. Energy Information Institution, “Annual Energy Outlook 2018 with Projections to 2050,” 2018.

[55] U.S. Energy Information Administration, “International Energy Statistics,” 2019. [Online]. Available: https://www.eia.gov/beta/international/data/browser/#/?c=4100000002000060000000000000g000200000000000000001&vs=INTL.44-1-AFRC-QBTU.A&vo=0&v=H&end=2016. [Accessed: 27-Apr-2019].

[56] P. Nema, S. Nema, and P. Roy, “An overview of global climate changing in current scenario and mitigation action,” *Renew. Sustain. Energy Rev.*, vol. 16, no. 4, pp. 2329–2336, 2012.

[57] P. A. Kharecha and J. E. Hansen, “Prevented mortality and greenhouse gas emissions from historical and projected nuclear power,” *Environ. Sci. Technol.*, vol. 47, no. 9, pp. 4889–4895, 2013.

[58] International Panel on Climate Change, *Summary for Policymakers: Special Report on Renewable Energy Sources and Climate Change Mitigation*. 2011.

[59] U.S. Energy Information Institution, “Annual Energy Outlook 2019 with projections to 2050,” 2018.

[60] Y. Izumi, “Recent advances in the photocatalytic conversion of carbon dioxide to fuels,” *Coord. Chem. Rev.*, vol. 257, pp. 171–186, 2013.

[61] N. Ghaffour, T. M. Missimer, and G. L. Amy, “Technical review and evaluation of the economics of water desalination: Current and future challenges for better water supply sustainability,” *Desalination*, vol. 309, no. 2013, pp. 197–207, 2013.

[62] A. Seamonds, “Global Desalination Markets Continues to Grow, Adding 4.2 Million Cubic Meters Per Day in Contracted Capacity - International Desalination Association and Global Water Intelligence Release New Data in 30 th Worldwide Desalting Inventory.” 2017.

[63] R. Das, S. Bee, A. Hamid, S. Ramakrishna, and Z. Z. Chowdhury, “Quenching the world ’ s thirst for seawater Engineered carbon nanotube membranes may help solve our growing demand for,” *Elsevier*, vol. 336, no. March 2014, pp. 1–5, 2015.

[64] P. Rao, R. Kostecki, L. Dale, and A. Gadgil, “Technology and Engineering of the Water-Energy Nexus,” *Annu. Rev. Environ. Resour.*, vol. 42, no. 1, pp. 407–437, 2017.

[65] E. Curcio, G. Di Profio, E. Fontananova, and E. Drioli, “Membrane technologies for seawater desalination and brackish water treatment,” *Adv. Membr. Technol. Water Treat.*, pp. 411–441, Jan. 2015.

[66] A. Al-Karaghouli and L. L. Kazmerski, “Energy consumption and water production cost of conventional and renewable-energy-powered desalination processes,” *Renew. Sustain. Energy Rev.*, vol. 24, pp. 343–356, 2013.

[67] S. Bhojwani, K. Topolski, R. Mukherjee, D. Sengupta, and M. M. El-Halwagi, “Technology review and data analysis for cost assessment of water treatment systems,” *Sci. Total Environ.*, vol. 651, pp. 2749–2761, 2019.

[68] D. M. Warsinger, E. W. Tow, K. G. Nayar, L. A. Maswadeh, and J. H. Lienhard V, “Energy efficiency of batch and semi-batch (CCRO) reverse osmosis desalination,” *Water Res.*, vol. 106, pp. 272–282, 2016.

[69] A. B. Mindler and A. C. Epstein, “Measurements and control in reverse osmosis desalination,” in *Desalination*, vol. 59, no. C, 1986, pp. 343–379.

[70] U. Lachish, “Osmosis and thermodynamics,” *Am. J. Phys.*, vol. 75, no. 11, pp. 997–998, 2007.

[71] M. Abdel-Jawad, “Energy sources for coupling with desalination plants in the GCC countries,” 2001.

[72] S. A. Avlonitis, K. Kouroumbas, and N. Vlachakis, “Energy consumption and membrane replacement cost for seawater RO desalination plants,” *Desalination*, vol. 157, no. 1–3, pp. 151–158, 2003.

[73] C. G. Hernández-gaona and S. Hernández, “Comparison of Energy Consumptions and Total Annual Costs Between Heat Integrated and Thermally Linked Distillation Sequences,” vol. 18, no. 2, pp. 137–143, 2004.

[74] S. P. Agashichev, “Analysis of integrated co-generative schemes including MSF, RO and power generating systems (present value of expenses and ‘levelised’ cost of water),” *Desalination*, vol. 164, no. 3, pp. 281–302, 2004.

[75] S. AGASHICHEV, “Systemic approach for techno-economic evaluation of triple hybrid (RO, MSF and power generation) scheme including accounting of CO2 emission,” *Energy*, vol. 30, no. 8, pp. 1283–1303, 2004.

[76] R. Semiat, “Energy issues in desalination processes,” *Environ. Sci. Technol.*, vol. 42, no. 22, pp. 8193–8201, 2008.

[77] I. C. Karagiannis and P. G. Soldatos, “Water desalination cost literature: review and assessment,” *Desalination*, vol. 223, no. 1–3, pp. 448–456, 2008.

[78] K. N. O. Kuroda, S. Takahashi, K. Wakamatsu, S. Itoh, S. Kubota, K. Kikushi, Y. Eguchi, Y. Ikenaga, N. Sohma, “An Electrodialysis Sea Water Desalination System Powered by Photovoltaic Cells,” *Deslination*, vol. 65, pp. 161–169, 1987.

[79] K. P. G. Mahabala R. Adiga, S.K. Adhikary, P.K. Narayanan, W.P. Harkare, S.D. Gomkale, “Performance Analysis of Photovoltaic Electrodialysis Desalination Plant at Tanote in Thar Desert,” *Desalination*, vol. 67, pp. 59–66, 1987.

[80] S. Dasgupta, B. S. Brunschwig, J. R. Winkler, and H. B. Gray, “Chem Soc Rev-Solar Fuels Editorial,” pp. 2213–2214, 2013.

[81] D. G. Nocera and M. P. Nash, “Powering the planet: Chemical challenges in solar energy utilization,” *Proc. Natl. Acad. Sci. United States Am.*, vol. 103, no. 43, 2006.

[82] The World Bank, “Solar resource maps of World,” *SOLARGIS*, 2017. [Online]. Available: https://solargis.com/maps-and-gis-data/download/world.

[83] V. Velmurugan and K. Srithar, “Performance analysis of solar stills based on various factors affecting the productivity - A review,” *Renew. Sustain. Energy Rev.*, vol. 15, no. 2, pp. 1294–1304, 2011.

[84] A. Kaushal and Varun, “Solar stills: A review,” *Renew. Sustain. Energy Rev.*, vol. 14, no. 1, pp. 446–453, 2010.

[85] C. M. and A. Yadav, “Water desalination system using solar heat: A review,” *Renew. Sustain. Energy Rev.*, vol. 67, pp. 1308–1330, 2017.

[86] J. Perlin and J. N. Gordes, *An Historical and Prospective Review of Solar Water Purification*. Riverton, Santa Barbara: ASES, 2005.

[87] M. T. Ali, H. E. S. Fath, and P. R. Armstrong, "A comprehensive techno-economical review of indirect solar desalination," *Renew. Sustain. Energy Rev.*, vol. 15, no. 8, pp. 4187–4199, 2011.

[88] E. Deniz, "Solar-Powered Desalination," in *Desalination Updates*, R. Y. Ning, Ed. IntechOpen, 2015.

[89] T. AnfasMukram and P. U. Suneesh, "EXPERIMENTAL ANALYSIS OF ACTIVE SOLAR STILL WITH AIR PUMP AND EXTERNAL BOOSTING MIRRORS," *Int. J. Innov. Res. Sci. Eng. Technol.*, vol. 2, no. 7, pp. 3084–3094, 2013.

[90] G. Mink, M. M. Aboabboud, and É. Karmazsin, "Air-blown solar still with heat recycling," *Sol. Energy*, vol. 62, no. 4, pp. 309–317, 1998.

[91] C. L. Ong, W. Escher, S. Paredes, A. S. G. Khalil, and B. Michel, "A novel concept of energy reuse from high concentration photovoltaic thermal (HCPVT) system for desalination," *Desalination*, vol. 295, no. June, pp. 70–81, 2012.

[92] S. Abdallah, O. Badran, and M. M. Abu-Khader, "Performance evaluation of a modified design of a single slope solar still," *Desalination*, vol. 219, no. 1–3, pp. 222–230, 2008.

[93] J. B. Al-Hinai H, Al-Nassri MS, "Effect of climatic, design and operational parameters on the yield of a simple solar still Al-Hinai, H. et al. Energy Conversion and Management, 2002, 43, (13), 1639–1650," *Energy Convers. Manag.*, vol. 43, no. 13, pp. 1639–1650, 2003.

[94] A. S. Nafey, M. Abdelkader, A. Abdelmotalip, and A. A. Mabrouk, “Solar still productivity enhancement,” *Energy Convers. Manag.*, vol. 42, no. 11, pp. 1401–1408, 2001.

[95] S. Nijmeh, S. Odeh, and B. Akash, “Experimental and theoretical study of a single-basin solar sill in Jordan,” *Int. Commun. Heat Mass Transf.*, vol. 32, no. 3–4, pp. 565–572, 2005.

[96] O. O. Badran, “Experimental study of the enhancement parameters on a single slope solar still productivity,” *Desalination*, vol. 209, no. 1-3 SPEC. ISS., pp. 136–143, 2007.

[97] C. M. and A. Yadav, “Water desalination system using solar heat: A review,” *Renew. Sustain. Energy Rev.*, vol. 67, pp. 1308–1330, 2017.

[98] A. A. El-Sebaii and E. El-Bialy, “Advanced designs of solar desalination systems: A review,” *Renew. Sustain. Energy Rev.*, vol. 49, pp. 1198–1212, 2015.

[99] S. A. Kalogirou, “Seawater desalination using renewable energy sources,” *Prog. Energy Combust. Sci.*, vol. 31, no. 3, pp. 242–281, 2005.

[100] M. A. Green, K. Emery, Y. Hishikawa, W. Warta, and E. D. Dunlop, “Solar cell efficiency table (version 46),” *Prog. Photovolt Res. Appl.*, vol. 23, pp. 805–812, 2015.

[101] M. Fathy, H. Hassan, and M. Salem Ahmed, “Experimental study on the effect of coupling parabolic trough collector with double slope solar still on its performance,” *Sol. Energy*, vol. 163, no. January, pp. 54–61, 2018.

[102] Z. M. Omara and M. A. Eltawil, “Hybrid of solar dish concentrator, new boiler and simple solar collector for brackish water desalination,” *Desalination*, vol. 326, pp. 62–68, 2013.

[103] B. Chaouchi, A. Zrelli, and S. Gabsi, “Desalination of brackish water by means of a parabolic solar concentrator,” *Desalination*, vol. 217, no. 1–3, pp. 118–126, 2007.

[104] S. Riffat and A. Mayere, “Performance evaluation of v-trough solar concentrator for water desalination applications,” *Appl. Therm. Eng.*, vol. 50, no. 1, pp. 234–244, 2013.

[105] T. Arunkumar, D. Denkenberger, R. Velraj, R. Sathyamurthy, H. Tanaka, and K. Vinothkumar, “Experimental study on a parabolic concentrator assisted solar desalting system,” *Energy Convers. Manag.*, vol. 105, pp. 665–674, 2015.

[106] S. Pauletta, “A Solar Fresnel Collector Based on an Evacuated Flat Receiver,” *Energy Procedia*, vol. 101, no. September, pp. 480–487, 2016.

[107] W. T. Xie, Y. J. Dai, R. Z. Wang, and K. Sumathy, “Concentrated solar energy applications using Fresnel lenses: A review,” *Renew. Sustain. Energy Rev.*, vol. 15, no. 6, pp. 2588–2606, 2011.

[108] G. Morin, J. Dersch, W. Platzer, M. Eck, and A. Häberle, “Comparison of Linear Fresnel and Parabolic Trough Collector power plants,” *Sol. Energy*, vol. 86, no. 1, pp. 1–12, 2012.

[109] P. Tao *et al.*, “Solar-driven interfacial evaporation,” *Nat. Energy*, vol. 3, no. 12, pp. 1031–1041, 2018.

[110] G. N. Tiwari and L. Sahota, *Advanced Solar-Distillation Systems*. 2017.

[111] A. H. Elsheikh *et al.*, “Thin film technology for solar steam generation: A new dawn,” *Sol. Energy*, vol. 177, no. August 2018, pp. 561–575, 2019.

[112] F. Cao, K. McEnaney, G. Chen, and Z. Ren, “A review of cermet-based spectrally selective solar absorbers,” *Energy Environ. Sci.*, vol. 7, no. 5, pp. 1615–1627, 2014.

[113] R. Feng, Y. Qiao, and C. Song, “A perspective on bio-inspired interfacial systems for solar clean-water generation,” *MRS Commun.*, vol. 9, no. 01, pp. 3–13, 2019.

[114] L. Zhu, M. Gao, C. K. N. Peh, and G. W. Ho, “Recent progress in solar-driven interfacial water evaporation: Advanced designs and applications,” *Nano Energy*, vol. 57, pp. 507–518, 2019.

[115] B. O. Seraphin, “Spectraily Selective Surfaces and Their Impact on Photothermal Solar Energy Conversion,” *Top. Appl. Phys.*, vol. 31, pp. 5–55, 1979.

[116] H. Müller, *Optical Properties of Metal Clusters*, vol. 194, no. Part_2. 2011.

[117] L. Scarabelli, A. Sánchez-Iglesias, J. Pérez-Juste, and L. M. Liz-Marzán, “A ‘Tips and Tricks’ Practical Guide to the Synthesis of Gold Nanorods,” *J. Phys. Chem. Lett.*, vol. 6, no. 21, pp. 4270–4279, 2015.

[118] J. A. Webb and R. Bardhan, “Emerging advances in nanomedicine with engineered gold nanostructures,” *Nanoscale*, vol. 6, no. 5, pp. 2502–2530, 2014.

[119] K. Manthiram and A. P. Alivisatos, “Tunable Localized Surface Plasmon Resonances in Tungsten Oxide Nanocrystals,” *J. Am. Chem. Soc.*, vol. 8, pp. 8–11, 2012.

[120] H. P. Dye-sensitized and P. Chen, “Tunable Localized Surface Plasmon-Enabled Broadband Light-Harvesting Enhancement for Solar Cells NIH Public Access,” *Nano Lett.*, no. September 2016, 2013.

[121] F. K. Soong and B.-H. Juang, “Optimal quantization of LSP parameters using delayed decisions,” *IEEE Trans. Speech Audio Process.*, vol. I, no. I, pp. 185–188, 1993.

[122] X. E. Guerrero-Dib, U. Ortiz-Méndez, D. Ferrer, S. Sepúlveda, M. Jose-Yacaman, and O. V. Kharissova, “Synthesis and properties of monometallic and bimetallic silver and gold nanoparticles,” *Int. J. Green Nanotechnol. Phys. Chem.*, vol. 1, no. 1, pp. 32–39, 2009.

[123] R. Long, Y. Li, L. Song, and Y. Xiong, “Coupling Solar Energy into Reactions: Materials Design for Surface Plasmon-Mediated Catalysis,” *Small*, vol. 11, no. 32, pp. 3873–3889, 2015.

[124] M. S. Zielinski *et al.*, “Hollow Mesoporous Plasmonic Nanoshells for Enhanced Solar Vapor Generation,” *Nano Lett.*, vol. 16, no. 4, pp. 2159–2167, 2016.

[125] H. Jin, G. Lin, L. Bai, A. Zeiny, and D. Wen, “Steam generation in a nanoparticle-based solar receiver,” *Nano Energy*, vol. 28, pp. 397–406, 2016.

[126] S. Yu *et al.*, “The impact of surface chemistry on the performance of localized solar-driven evaporation system,” *Sci. Rep.*, vol. 5, no. 1, p. 13600, 2015.

[127] D. Zhao *et al.*, “Enhancing Localized Evaporation through Separated Light Absorbing Centers and Scattering Centers,” *Sci. Rep.*, vol. 5, no. October, pp. 1–10, 2015.

[128] K. Bae, G. Kang, S. K. Cho, W. Park, K. Kim, and W. J. Padilla, “Flexible thin-film black gold membranes with ultrabroadband plasmonic nanofocusing for efficient solar vapour generation,” *Nat. Commun.*, vol. 6, pp. 1–9, 2015.

[129] L. Zhou, S. Zhuang, C. He, Y. Tan, Z. Wang, and J. Zhu, “Self-assembled spectrum selective plasmonic absorbers with tunable bandwidth for solar energy conversion,” *Nano Energy*, vol. 32, no. December 2016, pp. 195–200, 2017.

[130] X. Wang, Y. He, X. Liu, G. Cheng, and J. Zhu, “Solar steam generation through bio-inspired interface heating of broadband-absorbing plasmonic membranes,” *Appl. Energy*, vol. 195, pp. 414–425, 2017.

[131] H. Jin, G. Lin, A. Zeiny, L. Bai, and D. Wen, “Nanoparticle-based solar vapor generation: An experimental and numerical study,” *Energy*, vol. 178, pp. 447–459, 2019.

[132] G. M. Akselrod *et al.*, “Large-Area Metasurface Perfect Absorbers from Visible to Near-Infrared,” *Adv. Mater.*, vol. 27, no. 48, pp. 8028–8034, 2015.

[133] A. Politano *et al.*, “Photothermal Membrane Distillation for Seawater Desalination,” *Adv. Mater.*, vol. 29, no. 2, pp. 1–6, 2017.

[134] A. Alsaati and A. M. Marconnet, “Energy efficient membrane distillation through localized heating,” *Desalination*, vol. 442, no. May, pp. 99–107, 2018.

[135] L. Zhou *et al.*, “3D self-assembly of aluminium nanoparticles for plasmon-enhanced solar desalination,” *Nat. Photonics*, vol. 10, no. April, 2016.

[136] G. E. J. Poinern, “Can Anodic Aluminium Oxide Nanomembranes Treated with Nanometre Scale Hydroxyapatite be Used as a Cell Culture Substrate,” *Int. J. Mater. Sci. Appl.*, vol. 3, no. 6, p. 331, 2015.

[137] M. Fujiwara and T. Imura, “Photo Induced Membrane Separation Using Azobenzene Modified Anodized for Water Purification and Desalination Alumina Membranes,” *ACS Nano*, vol. 9, no. 6, pp. 5705–5712, 2015.

[138] C. Zhang, C. Yan, Z. Xue, W. Yu, Y. Xie, and T. Wang, “Shape-Controlled Synthesis of High-Quality Cu7S4 Nanocrystals for Efficient Light-Induced Water Evaporation,” *Small*, no. 38, pp. 5320–5328, 2016.

[139] P. Fan, H. Wu, M. Zhong, H. Zhang, B. Bai, and G. Jin, “Large-scale cauliflower-shaped hierarchical copper nanostructures for efficient photothermal conversion,” *Nanoscale*, vol. 8, no. August, pp. 14617–14624, 2016.

[140] X. Wang, Y. He, Y. Hu, G. Jin, B. Jiang, and Y. Huang, “Photothermal-conversion-enhanced photocatalytic activity of flower-like CuS superparticles under solar light irradiation,” *Sol. Energy*, vol. 170, no. June, pp. 586–593, 2018.

[141] M. Kaur, S. Ishii, S. L. Shinde, and T. Nagao, “All-Ceramic Microfibrous Solar Steam Generator: TiN Plasmonic Nanoparticle-Loaded Transparent Microfibers,” *ACS Sustain. Chem. Eng.*, vol. 5, no. 10, pp. 8523–8528, 2017.

[142] H. Yu *et al.*, “Alkali-Assisted Synthesis of Nitrogen Deficient Graphitic Carbon Nitride with Tunable Band Structures for Efficient Visible-Light-Driven Hydrogen Evolution,” *Adv. Mater.*, vol. 29, no. 16, p. 1605148, 2017.

[143] A. Lalisse, G. Tessier, J. Plain, and G. Baffou, “Quantifying the Efficiency of Plasmonic Materials for Near-Field Enhancement and Photothermal Conversion,” *J. Phys. Chem. C*, vol. 119, no. 45, pp. 25518–25528, 2015.

[144] N. Han *et al.*, “Highly efficient and stable solar-powered desalination by tungsten carbide nanoarray film with sandwich wettability,” *Sci. Bull.*, vol. 64, no. 6, pp. 391–399, 2019.

[145] L. Zhu, M. Gao, C. K. N. Peh, and G. W. Ho, “Solar-driven photothermal nanostructured materials designs and prerequisites for evaporation and catalysis applications,” *Mater. Horizons*, vol. 5, no. 3, pp. 323–343, 2018.

[146] M. W. Higgins, A. R. Shakeel Rahmaan, R. R. Devarapalli, M. V. Shelke, and N. Jha, "Carbon fabric based solar steam generation for waste water treatment," *Sol. Energy*, vol. 159, no. December 2017, pp. 800–810, 2018.

[147] J. Wang *et al.*, "High-Performance Photothermal Conversion of Narrow-Bandgap Ti2O3Nanoparticles," *Adv. Mater.*, vol. 29, no. 3, pp. 1–6, 2017.

[148] M. Ye *et al.*, "Synthesis of Black TiOx Nanoparticles by Mg Reduction of TiO2 Nanocrystals and their Application for Solar Water Evaporation," *Adv. Energy Mater.*, vol. 7, no. 4, pp. 1–7, 2017.

[149] G. Zhu, J. Xu, W. Zhao, and F. Huang, "Constructing black titania with unique nanocage structure for solar desalination," *ACS Appl. Mater. Interfaces*, vol. 8, no. 46, pp. 31716–31721, 2016.

[150] A. Alkhudhiri, N. Darwish, and N. Hilal, "Membrane distillation: A comprehensive review," *Desalination*, vol. 287, pp. 2–18, 2012.

[151] S. Ishii, R. P. Sugavaneshwar, K. Chen, T. D. Dao, and T. Nagao, "Solar water heating and vaporization with silicon nanoparticles at mie resonances," *Opt. Mater. Express*, vol. 6, no. 2, pp. 640–648, 2016.

[152] B. E. Deal and A. S. Grove, "General relationship for the thermal oxidation of silicon," *J. Appl. Phys.*, vol. 36, no. 12, pp. 3770–3778, 1965.

[153] L. L. Baranowski, G. J. Snyder, and E. S. Toberer, "Concentrated solar thermoelectric generators," *Energy Environ. Sci.*, vol. 5, no. 10, pp. 9055–9067, 2012.

[154] H. S. Kim, W. Liu, and Z. Ren, “The bridge between the materials and devices of thermoelectric power generators,” *Energy Environ. Sci.*, vol. 10, no. 1, pp. 69–85, 2017.

[155] D. Kraemer *et al.*, “High-performance flat-panel solar thermoelectric generators with high thermal concentration,” *Nat. Mater.*, vol. 10, no. 7, pp. 532–538, 2011.

[156] T. K. Kim *et al.*, “Si boride-coated Si nanoparticles with improved thermal oxidation resistance,” *Nano Energy*, vol. 9, pp. 32–40, 2014.

[157] M. F. L. De Volder, S. H. Tawfick, R. H. Baughman, and A. J. Hart, “Carbon nanotubes: present and future commercial applications - Supplemental Information,” *Science (80-.).*, vol. 339, no. 6119, pp. 535–539, 2013.

[158] E. T. Thostenson, Z. Ren, and T. Chou, “Advances in the science and technology of carbon nanotubes and their composites: a review,” *Compos. Sci. Technol.*, vol. 61, pp. 1899–1912, 2001.

[159] Z. Han and A. Fina, “Thermal conductivity of carbon nanotubes and their polymer nanocomposites: A review,” *Prog. Polym. Sci.*, vol. 36, no. 7, pp. 914–944, 2011.

[160] M. J. Allen, V. C. Tung, and R. B. Kaner, “Honeycomb Carbon : A Review of Graphene,” *Chem. Rev.*, pp. 132–145, 2010.

[161] V. B. Mohan, K. tak Lau, D. Hui, and D. Bhattacharyya, “Graphene-based materials and their composites: A review on production, applications and product limitations,” *Compos. Part B Eng.*, vol. 142, no. January, pp. 200–220, 2018.

[162] S. Li, B. Jin, X. Zhai, H. Li, and Q. Jiang, “Review of Carbon Materials for Lithium-Sulfur Batteries,” *ChemistrySelect*, vol. 3, no. 8, pp. 2245–2260, 2018.

[163] M. A. Worsley *et al.*, "Toward macroscale, isotropic carbons with graphene-sheet-like electrical and mechanical properties," *Adv. Funct. Mater.*, vol. 24, no. 27, pp. 4259–4264, 2014.

[164] S. M. Sajadi, N. Farokhnia, P. Irajizad, M. Hasnain, and H. Ghasemi, "Flexible artificially-networked structure for ambient/high pressure solar steam generation," *J. Mater. Chem. A*, vol. 4, no. 13, pp. 4700–4705, 2016.

[165] G. Ni *et al.*, "Volumetric solar heating of nano fluids for direct vapor generation," *Nano Energy*, pp. 290–301, 2015.

[166] F. Tao *et al.*, "Graphite powder/semipermeable collodion membrane composite for water evaporation," *Sol. Energy Mater. Sol. Cells*, vol. 180, no. August 2017, pp. 34–45, 2018.

[167] V. Kashyap, A. Al-Bayati, S. M. Sajadi, P. Irajizad, S. H. Wang, and H. Ghasemi, "A flexible anti-clogging graphite film for scalable solar desalination by heat localization," *J. Mater. Chem. A*, vol. 5, no. 29, pp. 15227–15234, 2017.

[168] A. Guo, X. Ming, Y. Fu, G. Wang, and X. Wang, "Fiber-Based, Double-Sided, Reduced Graphene Oxide Films for Efficient Solar Vapor Generation," *ACS Appl. Mater. Interfaces*, vol. 9, no. 35, pp. 29958–29964, 2017.

[169] Y. Ito, Y. Tanabe, J. Han, T. Fujita, K. Tanigaki, and M. Chen, "Multifunctional Porous Graphene for High-Efficiency Steam Generation by Heat Localization," *Adv. Mater.*, vol. 27, no. 29, pp. 4302–4307, 2015.

[170] H. C. Yang *et al.*, "Chinese Ink: A Powerful Photothermal Material for Solar Steam Generation," *Adv. Mater. Interfaces*, vol. 6, no. 1, pp. 1–7, 2019.

[171] X. Gao *et al.*, “Synthesis of Hierarchical Graphdiyne-Based Architecture for Efficient Solar Steam Generation,” *Chem. Mater.*, vol. 29, no. 14, pp. 5777–5781, 2017.

[172] Y. Fu, G. Wang, T. Mei, J. Li, J. Wang, and X. Wang, “Accessible Graphene Aerogel for Efficiently Harvesting Solar Energy,” *ACS Sustain. Chem. Eng.*, vol. 5, no. 6, pp. 4665–4671, 2017.

[173] A. Guo, X. Ming, Y. Fu, G. Wang, and X. Wang, “Fiber-Based, Double-Sided, Reduced Graphene Oxide Films for Efficient Solar Vapor Generation,” *ACS Appl. Mater. Interfaces*, vol. 9, no. 35, pp. 29958–29964, 2017.

[174] X. Li *et al.*, “Graphene oxide-based efficient and scalable solar desalination under one sun with a confined 2D water path,” *Proc. Natl. Acad. Sci.*, vol. 113, no. 49, pp. 13953–13958, 2016.

[175] C. Finnerty, L. Zhang, D. L. Sedlak, K. L. Nelson, and B. Mi, “Synthetic Graphene Oxide Leaf for Solar Desalination with Zero Liquid Discharge,” *Environ. Sci. Technol.*, vol. 51, no. 20, pp. 11701–11709, 2017.

[176] J. Lou *et al.*, “Bioinspired Multifunctional Paper-Based rGO Composites for Solar- Driven Clean Water Generation,” 2016.

[177] X. Hu *et al.*, “Tailoring Graphene Oxide-Based Aerogels for Efficient Solar Steam Generation under One Sun,” *Adv. Mater.*, vol. 29, no. 5, 2017.

[178] Y. Li *et al.*, “Graphene oxide-based evaporator with one-dimensional water transport enabling high-efficiency solar desalination,” *Nano Energy*, vol. 41, no. August, pp. 201–209, 2017.

[179] Y. Fu *et al.*, “Oxygen plasma treated graphene aerogel as a solar absorber for rapid and efficient solar steam generation,” *Carbon N. Y.*, vol. 130, pp. 250–256, 2018.

[180] J. Zhou *et al.*, “Macroscopic and Mechanically Robust Hollow Carbon Spheres with Superior Oil Adsorption and Light-to-Heat Evaporation Properties,” *Adv. Funct. Mater.*, vol. 26, no. 29, pp. 5368–5375, 2016.

[181] F. Jiang *et al.*, “Lightweight, Mesoporous, and Highly Absorptive All-Nanofiber Aerogel for Efficient Solar Steam Generation,” *ACS Appl. Mater. Interfaces*, vol. 10, no. 1, pp. 1104–1112, 2018.

[182] Z. Yin *et al.*, “Extremely Black Vertically Aligned Carbon Nanotube Arrays for Solar Steam Generation,” *ACS Appl. Mater. Interfaces*, vol. 9, no. 34, pp. 28596–28603, 2017.

[183] X. Wang, Y. He, G. Cheng, L. Shi, X. Liu, and J. Zhu, “Direct vapor generation through localized solar heating via carbon-nanotube nanofluid,” *Energy Convers. Manag.*, vol. 130, pp. 176–183, 2016.

[184] X. Wang, Y. He, X. Liu, and J. Zhu, “Enhanced direct steam generation via a bio-inspired solar heating method using carbon nanotube films,” *Powder Technol.*, vol. 321, pp. 276–285, 2017.

[185] N. Xu *et al.*, “Mushrooms as Efficient Solar Steam-Generation Devices,” *Adv. Mater.*, vol. 29, no. 28, pp. 1–5, 2017.

[186] C. Chen *et al.*, “Highly Flexible and Efficient Solar Steam Generation Device,” *Adv. Mater.*, vol. 29, no. 30, pp. 1–8, 2017.

[187] C. Jia *et al.*, “Rich Mesostructures Derived from Natural Woods for Solar Steam Generation,” *Joule*, vol. 1, no. 3, pp. 588–599, 2017.

[188] H. Liu *et al.*, “Narrow bandgap semiconductor decorated wood membrane for high-efficiency solar-assisted water purification,” *J. Mater. Chem. A*, vol. 6, no. 39, pp. 18839–18846, 2018.

[189] R. Chen *et al.*, “Interfacial solar heating by self-assembled Fe3O4@C film for steam generation,” *Mater. Chem. Front.*, vol. 1, pp. 2620–2626, 2017.

[190] Y. Liu, X. Wang, and H. Wu, “High-performance wastewater treatment based on reusable functional photo-absorbers,” *Chem. Eng. J.*, vol. 309, pp. 787–794, 2017.

[191] Y. Yang *et al.*, “A Two-Dimensional Flexible Bilayer Janus Membrane for Advanced Photothermal Water Desalination,” *ACS Energy Lett.*, 2018.

[192] Q. Jiang *et al.*, “Bilayered Biofoam for Highly Efficient Solar Steam Generation,” *Adv. Mater.*, vol. 28, no. 42, pp. 9400–9407, 2016.

[193] L. Huang, J. Pei, H. Jiang, and X. Hu, “Water desalination under one sun using graphene-based material modified PTFE membrane,” *Desalination*, vol. 442, no. April, pp. 1–7, 2018.

[194] G. Wang, Y. Fu, X. Ma, W. Pi, D. Liu, and X. Wang, “Reusable reduced graphene oxide based double-layer system modified by polyethylenimine for solar steam generation,” *Carbon N. Y.*, vol. 114, pp. 117–124, 2017.

[195] G. Wang *et al.*, “Reduced Graphene Oxide-Polyurethane Nanocomposite Foam as a Reusable Photoreceiver for Efficient Solar Steam Generation,” *Chem. Mater.*, vol. 29, no. 13, pp. 5629–5635, 2017.

[196] T. Gao *et al.*, “Architecting a Floatable, Durable, and Scalable Steam Generator: Hydrophobic/Hydrophilic Bifunctional Structure for Solar Evaporation Enhancement,” *Small Methods*, vol. 3, no. 2, p. 1800176, 2018.

[197] J. Xu *et al.*, “Copper nanodot-embedded graphene urchins of nearly full-spectrum solar absorption and extraordinary solar desalination,” *Nano Energy*, vol. 53, pp. 425–431, 2018.

[198] J. Zhao, W. Ren, and H. M. Cheng, “Graphene sponge for efficient and repeatable adsorption and desorption of water contaminations,” *J. Mater. Chem.*, vol. 22, no. 38, pp. 20197–20202, 2012.

[199] J. Yang *et al.*, “Functionalized Graphene Enables Highly Efficient Solar Thermal Steam Generation,” *ACS Nano*, vol. 11, no. 6, pp. 5510–5518, 2017.

[200] J. E. Mark, H. R. Allcock, and W. Robert, *Inorganic polymers*, 2nd ed. Oxford University Press on Demand, 2005.

[201] A. Nag, S. C. Mukhopadhyay, and J. Kosel, “Wearable Flexible Sensors: A Review,” *IEEE Sens. J.*, vol. 17, no. 13, pp. 3949–3960, 2017.

[202] S. Bhatacharya, A. Datta, J. M. Berg, and S. Gangopadhyay, “Studies on Surface Wettability of Studies on Surface Wettability of Poly (Dimethyl) Siloxane (PDMS) and Glass Under Oxygen-Plasma Treatment and Correlation With Bond Strength,” *J. MICROELECTROMECHANICAL Syst.*, vol. 14, no. June, pp. 590–597, 2005.

[203] L. Libioulle, A. Bietsch, H. Schmid, B. Michel, and E. Delamarche, “Contact-Inking Stamps for Microcontact Printing of Alkanethiols on Gold,” *Langmuir*, vol. 15, no. 2, pp. 300–304, 2002.

[204] B. H. Ryu and D. E. Kim, “Development of highly durable and low friction micro-structured PDMS coating based on bio-inspired surface design,” *CIRP Ann. - Manuf. Technol.*, vol. 64, no. 1, pp. 519–522, 2015.

[205] U. Eduok, O. Faye, and J. Szpunar, “Progress in Organic Coatings Recent developments and applications of protective silicone coatings : A review of PDMS functional materials,” *Prog. Org. Coatings*, vol. 111, no. May, pp. 124–163, 2017.

[206] Y. R. Liu, Y. D. Huang, and L. Liu, “Effects of TriSilanolIsobutyl-POSS on thermal stability of methylsilicone resin,” *Polym. Degrad. Stab.*, vol. 91, no. 11, pp. 2731–2738, 2006.

[207] Q. Liu, W. Shi, F. Babonneau, and L. V. Interrante, “Synthesis of Polycarbosilane/Siloxane Hybrid Polymers and Their Pyrolytic Conversion to Silicon Oxycarbide Ceramics,” *Chem. Mater.*, vol. 9, no. 11, pp. 2434–2441, 1997.

[208] K. Hayashida, S. Tsuge, and H. Ohtani, “Flame retardant mechanism of polydimethylsiloxane material containing platinum compound studied by analytical pyrolysis techniques and alkaline hydrolysis gas chromatography,” *Polymer (Guildf).*, vol. 44, no. 19, pp. 5611–5616, 2003.

[209] J. Mansouri, R. P. Burford, Y. B. Cheng, and L. Hanu, “Formation of strong ceramified ash from silicone-based compositions,” *J. Mater. Sci.*, vol. 40, no. 21, pp. 5741–5749, 2005.

[210] A. Seth, W. J. Van Ooij, P. Puomi, T. Metroke, and A. Apblett, “Characterization of one-step , chromate-free , primer systems using liquid-state 29 Si and 13 C NMR,” *Prog. Org. Coatings*, vol. 60, pp. 170–177, 2007.

[211] P. Wang and D. W. Schaefer, “Why does Silane Enhance the Protective Properties of Epoxy Films?,” *Langmuir*, vol. 5, no. 15, pp. 13496–13501, 2008.

[212] M. Jiang, L. Wu, J. Hu, and J. Zhang, “Silane-incorporated epoxy coatings on aluminum alloy (AA2024). Part 1 : Improved corrosion performance,” *Corros. Sci.*, vol. 92, pp. 118–126, 2015.

[213] L. Wu, J. Zhang, J. Hu, and J. Zhang, “Improved corrosion performance of electrophoretic coatings by silane addition,” *Corros. Sci.*, vol. 56, pp. 58–66, 2012.

[214] M. Yu, F. Liu, and F. Du, “Synthesis and properties of a green and self-cleaning hard protective coating,” *Prog. Org. Coatings*, vol. 94, pp. 34–40, 2016.

[215] C. Kapridaki and P. Maravelaki-Kalaitzaki, “TiO2-SiO2-PDMS nano-composite hydrophobic coating with self-cleaning properties for marble protection,” *Prog. Org. Coatings*, vol. 76, no. 2–3, pp. 400–410, 2013.

[216] D. Yu, Y. Zhao, H. Li, H. Qi, B. Li, and X. Yuan, “Preparation and evaluation of hydrophobic surfaces of polyacrylate- polydimethylsiloxane copolymers for anti-icing,” *Prog. Org. Coatings*, vol. 76, no. 10, pp. 1435–1444, 2013.

[217] V. Bahadur, L. Mishchenko, B. Hatton, J. A. Taylor, J. Aizenberg, and T. Krupenkin, “Predictive model for ice formation on superhydrophobic surfaces,” *Langmuir*, vol. 27, no. 23, pp. 14143–14150, 2011.

[218] G. Davaasuren, C. V. Ngo, H. S. Oh, and D. M. Chun, “Geometric study of transparent superhydrophobic surfaces of molded and grid patterned polydimethylsiloxane (PDMS),” *Appl. Surf. Sci.*, vol. 314, pp. 530–536, 2014.

[219] F. Trespidi, G. Timò, F. Galeotti, and M. Pasini, “PDMS antireflection nano-coating for glass substrates,” *Microelectron. Eng.*, vol. 126, pp. 13–18, 2014.

[220] Y. Zhang, X. Zhang, H. Ye, B. Xiao, L. Yan, and B. Jiang, “A simple route to prepare crack-free thick antireflective silica coatings with improved antireflective stability,” *Mater. Lett.*, vol. 69, pp. 86–88, 2012.

[221] S. Yao and Y. Zhu, “Wearable multifunctional sensors using printed stretchable conductors made of silver nanowires,” *Nanoscale*, vol. 6, no. 4, pp. 2345–2352, 2014.

[222] S. T. Muntha, A. Kausar, and M. Siddiq, “A Review Featuring Fabrication , Properties , and Application of Polymeric Mixed Matrix Membrane Reinforced with Different Fillers,” *Polym. Plast. Technol. Eng.*, vol. 56, no. 18, pp. 2043–2064, 2017.

[223] S. H. Bae, Y. Lee, B. K. Sharma, H. J. Lee, J. H. Kim, and J. H. Ahn, “Graphene-based transparent strain sensor,” *Carbon N. Y.*, vol. 51, no. 1, pp. 236–242, 2013.

[224] C. Howell, A. Grinthal, S. Sunny, M. Aizenberg, and J. Aizenberg, “Designing Liquid-Infused Surfaces for Medical Applications : A Review,” *Adv. Mater.*, vol. 1802724, pp. 1–26, 2018.

[225] Z. Zhang, X. Feng, Q. Luo, and B. F. Liu, “Environmentally friendly surface modification of PDMS using PEG polymer brush,” *Electrophoresis*, vol. 30, no. 18, pp. 3174–3180, 2009.

[226] C. X. Liu and J. W. Choi, “Patterning conductive PDMS nanocomposite in an elastomer using microcontact printing,” *J. Micromechanics Microengineering*, vol. 19, no. 8, 2009.

[227] A. V. Alaferdov *et al.*, “A wearable, highly stable, strain and bending sensor based on high aspect ratio graphite nanobelts,” *Nanotechnology*, vol. 27, no. 37, 2016.

[228] K. S. Kim *et al.*, “Large-scale pattern growth of graphene films for stretchable transparent electrodes,” *Nature*, vol. 457, no. 7230, pp. 706–10, 2009.

[229] S. H. Lee, Y. Lee, and J. J. Yoh, “Reduced graphene oxide coated polydimethylsiloxane film as an optoacoustic transmitter for high pressure and high frequency ultrasound generation,” *Appl. Phys. Lett.*, vol. 081911, no. 2015, pp. 1–5, 2017.

[230] J. Shi *et al.*, “Graphene Reinforced Carbon Nanotube Networks for Wearable Strain Sensors,” *Adv. Funct. Mater.*, vol. 26, no. 13, pp. 2078–2084, 2016.

[231] Y. Song, J. I. Lee, S. Pyo, Y. Eun, J. Choi, and J. Kim, “A highly sensitive flexible strain sensor based on the contact resistance change of carbon nanotube bundles,” *Nanotechnology*, vol. 27, no. 20, 2016.

[232] H. Bao-Yu, K. Jinwook, Z. Jiadeng, L. Sibo, Z. Xiangwu, and J. Xiaoning, “A laser ultrasound transducer using carbon nanofibers – polydimethylsiloxane composite thin film,” *Appl. Phys. Lett.*, vol. 021902, no. September 2014, 2015.

[233] T. Buma, M. Spisar, and M. O’Donnell, “High-frequency ultrasound array element using thermoelastic expansion in an elastomeric film,” *Appl. Phys. Lett.*, vol. 548, no. July 2001, 2014.

[234] Y. Hou, J.-S. Kim, S. Ashkenazi, M. O’Donnell, and L. J. Guo, “Optical generation of high frequency ultrasound using two-dimensional gold nanostructure,” *Appl. Phys. Lett.*, vol. 093901, no. July 2006, 2015.

[235] M. Amjadi, A. Pichitpajongkit, S. Lee, S. Ryu, and I. Park, "Highly stretchable and sensitive strain sensor based on silver nanowire-elastomer nanocomposite," *ACS Nano*, vol. 8, no. 5, pp. 5154–5163, 2014.

[236] H. Lu *et al.*, "Highly uniform SERS-active microchannel on hydrophobic PDMS: a balance of high reproducibility and sensitivity for detection of proteins," *RSC Adv.*, vol. 7, no. 15, pp. 8771–8778, 2017.

[237] C. Lee, C. S. Robertson, A. H. Nguyen, M. Kahraman, and S. Wachsmann-Hogiu, "Thickness of a metallic film, in addition to its roughness, plays a significant role in SERS activity," *Sci. Rep.*, vol. 5, no. June, 2015.

[238] Y. R. Jeong *et al.*, "A skin-attachable, stretchable integrated system based on liquid GaInSn for wireless human motion monitoring with multi-site sensing capabilities," *NPG Asia Mater.*, vol. 9, no. 10, pp. 1–8, 2017.

[239] R. Seghir and S. Arscott, "Controlled mud-crack patterning and self-organized cracking of polydimethylsiloxane elastomer surfaces," *Sci. Rep.*, vol. 5, no. March, pp. 1–16, 2015.

[240] S. P. Lacour, S. Wagner, Z. Huang, and Z. Suo, "Stretchable gold conductors on elastomeric substrates," *Appl. Phys. Lett.*, vol. 82, no. 15, pp. 2404–2406, 2003.

[241] C. Y. Chen, C. L. Chang, T. F. Chien, and C. H. Luo, "Flexible PDMS electrode for one-point wearable wireless bio-potential acquisition," *Sensors Actuators, A Phys.*, vol. 203, pp. 20–28, 2013.

[242] T. Zhao, L. Su, and W. Xia, "Optical Ultrasound Generation and Detection for Intravascular Imaging: A Review," *J. Healthc. Eng.*, vol. 2018, pp. 1–14, 2018.

[243] Ha-Chul Jung *et al.*, “CNT/PDMS Composite Flexible Dry Electrodesfor Long-Term ECG Monitoring,” *IEEE Trans. Biomed. Eng.*, vol. 59, no. 5, pp. 1472–1479, 2012.

[244] S. R. Yadhuraj, B. G. Sudarshan, S. C. Prasanna Kumar, and D. Mahesh Kumar, “Study of PDMS material for ECG electrodes,” *Mater. Today Proc.*, vol. 5, no. 4, pp. 10635–10643, 2018.

[245] J. Hoon Lee, S. Min Lee, H. Jin Byeon, J. Sook Hong, K. Suk Park, and S.-H. Lee, “CNT/PDMS-based canal-typed ear electrodes for inconspicuous EEG recording,” *J. Neural Eng.*, vol. 11, no. 4, p. 046014, 2014.

[246] L. F. Wang, J. Q. Liu, B. Yang, and C. S. Yang, “PDMS-based low cost flexible dry electrode for long-term EEG measurement,” *IEEE Sens. J.*, vol. 12, no. 9, pp. 2898–2904, 2012.

[247] C. Y. Chen *et al.*, “A low-power bio-potential acquisition system with flexible PDMS dry electrodes for portable ubiquitous healthcare applications,” *Sensors (Switzerland)*, vol. 13, no. 3, pp. 3077–3091, 2013.

[248] S. Noimark *et al.*, “Polydimethylsiloxane Composites for Optical Ultrasound Generation and Multimodality Imaging,” *Adv. Funct. Mater.*, vol. 1704919, pp. 1–16, 2018.

[249] M. Amjadi, K. U. Kyung, I. Park, and M. Sitti, “Stretchable, Skin-Mountable, and Wearable Strain Sensors and Their Potential Applications: A Review,” *Adv. Funct. Mater.*, vol. 26, no. 11, pp. 1678–1698, 2016.

[250] R. Ramalingame *et al.*, “Flexible piezoresistive sensor matrix based on a carbon nanotube PDMS composite for dynamic pressure distribution measurement,” *J. Sensors Sens. Syst.*, vol. 8, no. 1, pp. 1–7, 2019.

[251] N. Lu, C. Lu, S. Yang, and J. Rogers, “Highly sensitive skin-mountable strain gauges based entirely on elastomers,” *Adv. Funct. Mater.*, vol. 22, no. 19, pp. 4044–4050, 2012.

[252] G. Schwartz *et al.*, “Flexible polymer transistors with high pressure sensitivity for application in electronic skin and health monitoring,” *Nat. Commun.*, vol. 4, no. May, pp. 1858–1859, 2013.

[253] S. Park *et al.*, “Stretchable Energy-Harvesting Tactile Electronic Skin Capable of Differentiating Multiple Mechanical Stimuli Modes,” *Adv. Mater.*, vol. 26, no. 43, pp. 7324–7332, 2014.

[254] S. Gong *et al.*, “A wearable and highly sensitive pressure sensor with ultrathin gold nanowires,” *Nat. Commun.*, vol. 5, p. 3132, 2014.

[255] H. W. Baac *et al.*, “Carbon nanotube composite optoacoustic transmitters for strong and high frequency ultrasound generation,” *Appl. Phys. Lett.*, vol. 234104, no. August 2010, pp. 1–4, 2015.

[256] R. J. Colchester *et al.*, “Laser-generated ultrasound with optical fibres using functionalised carbon nanotube composite coatings nanotube composite coatings,” *Appl. Phys. Lett.*, vol. 173502, no. February 2014, 2017.

[257] S. Noimark *et al.*, “Carbon-Nanotube – PDMS Composite Coatings on Optical Fibers for All-Optical Ultrasound Imaging,” *Adv. Funct. Mater.*, pp. 8390–8396, 2016.

[258] E. Biagi, F. Margheri, and D. Menichelli, “Efficient Laser-Ultrasound Generation by Using Heavily Absorbing Films as Targets,” *IEEE Trans. Ultrason. Ferroelectr. Freq. Control*, vol. 48, no. 6, pp. 1669–1680, 2001.

[259] D. Wu, F. Xu, B. Sun, R. Fu, H. He, and K. Matyjaszewski, “Design and Preparation of Porous Polymers,” *Chem. Rev.*, vol. 112, no. 7, pp. 3959–4015, 2012.

[260] A. G. Slater and A. I. Cooper, “Function-led design of new porous materials,” *Science (80-.).*, vol. 348, no. 6238, p. aaa8075, 2015.

[261] X. Zhou, “Recent progress in fabrication and application of polydimethylsiloxane sponges,” *J. Mater. Chem. A Mater. energy Sustain.*, vol. 5, no. 32, pp. 16467–16497, 2017.

[262] X. Zhao, L. Li, B. Li, J. Zhang, and A. Wang, “Durable superhydrophobic/superoleophilic PDMS sponges and their applications in selective oil absorption and in plugging oil leakages,” *J. Mater. Chem. A*, vol. 2, no. 43, pp. 18281–18287, 2014.

[263] S. J. Choi *et al.*, “A polydimethylsiloxane (PDMS) sponge for the selective absorption of oil from water,” *ACS Appl. Mater. Interfaces*, vol. 3, no. 12, pp. 4552–4556, 2011.

[264] K. J. Cha and D. S. Kim, “A portable pressure pump for microfluidic lab-on-a-chip systems using a porous polydimethylsiloxane (PDMS) sponge,” *Biomed. Microdevices*, vol. 13, no. 5, pp. 877–883, 2011.

[265] C. Yu *et al.*, “Facile Preparation of the Porous PDMS Oil-Absorbent for Oil/Water Separation,” *Adv. Mater. Interfaces*, vol. 4, no. 3, 2017.

[266] T. Zhang *et al.*, “Bifunctional organic sponge photocatalyst for efficient cross-dehydrogenative coupling of tertiary amines to ketones,” *Chem. Commun.*, vol. 53, no. 93, pp. 12536–12539, 2017.

[267] X. Li *et al.*, “Organic sponge photocatalysis,” *Green Chem.*, vol. 19, no. 13, pp. 2925–2930, 2017.

[268] R. K. Gupta, G. J. Dunderdale, M. W. England, and A. Hozumi, “Oil/water separation techniques: A review of recent progresses and future directions,” *J. Mater. Chem. A*, vol. 5, no. 31, pp. 16025–16058, 2017.

[269] M. Khosravi and S. Azizian, “Synthesis of a Novel Highly Oleophilic and Highly Hydrophobic Sponge for Rapid Oil Spill Cleanup,” *ACS Appl. Mater. Interfaces*, vol. 7, no. 45, pp. 25326–25333, 2015.

[270] D. D. Nguyen, N. H. Tai, S. B. Lee, and W. S. Kuo, “Superhydrophobic and superoleophilic properties of graphene-based sponges fabricated using a facile dip coating method,” *Energy Environ. Sci.*, vol. 5, no. 7, pp. 7908–7912, 2012.

[271] R. Iglio, S. Mariani, V. Robbiano, L. Strambini, and G. Barillaro, “Flexible Polydimethylsiloxane Foams Decorated with Multiwalled Carbon Nanotubes Enable Unprecedented Detection of Ultralow Strain and Pressure Coupled with a Large Working Range,” *ACS Appl. Mater. Interfaces*, vol. 10, no. 16, pp. 13877–13885, 2018.

[272] S. Wu *et al.*, “Novel Electrically Conductive Porous PDMS/Carbon Nanofiber Composites for Deformable Strain Sensors and Conductors,” *ACS Appl. Mater. Interfaces*, vol. 9, no. 16, pp. 14207–14215, 2017.

[273] R. Xu *et al.*, "Facile fabrication of three-dimensional graphene foam/ poly(dimethylsiloxane) composites and their potential application as strain sensor," *ACS Appl. Mater. Interfaces,* vol. 6, no. 16, pp. 13455–13460, 2014.

[274] L. Ding *et al.*, "Stress and Magnetic Field Bimode Detection Sensors Based on Flexible CI/CNTs-PDMS Sponges," *ACS Appl. Mater. Interfaces,* vol. 10, no. 36, pp. 30774–30784, 2018.

[275] S. Liang *et al.*, "Liquid metal sponges for mechanically durable, all-soft, electrical conductors," *J. Mater. Chem. C*, vol. 5, no. 7, pp. 1586–1590, 2017.

[276] J. Park *et al.*, "Three-dimensional nanonetworks for giant stretchability in dielectrics and conductors," *Nat. Commun.*, vol. 3, no. May, pp. 1–8, 2012.

[277] S. Liang *et al.*, "3D Stretchable, Compressible, and Highly Conductive Metal-Coated Polydimethylsiloxane Sponges," *Adv. Mater. Technol.*, vol. 1, no. 7, p. 1600117, 2016.

[278] M. Charara, W. Luo, M. C. Saha, and Y. Liu, "Investigation of Lightweight and Flexible Carbon Nanofiber/Poly Dimethylsiloxane Nanocomposite Sponge for Piezoresistive Sensor Application," *Adv. Eng. Mater.,* vol. 1801068, pp. 1–12, 2019.

[279] G. Zhou *et al.*, "A graphene foam electrode with high sulfur loading for flexible and high energy Li-S batteries," *Nano Energy*, vol. 11, pp. 356–365, 2015.

[280] W. Liu *et al.*, "3D Porous Sponge-Inspired Electrode for Stretchable Lithium-Ion Batteries," *Adv. Mater.*, vol. 28, no. 18, pp. 3578–3583, 2016.

[281] H. Li *et al.*, "An All-Stretchable-Component Sodium-Ion Full Battery," *Adv. Mater.*, vol. 29, no. 23, pp. 1–7, 2017.

[282] M. Taghavi, V. Mattoli, A. Sadeghi, B. Mazzolai, and L. Beccai, “A novel soft metal-polymer composite for multidirectional pressure energy harvesting,” *Adv. Energy Mater.*, vol. 4, no. 12, pp. 1–6, 2014.

[283] Q. Zhang, X. Xu, H. Li, G. Xiong, H. Hu, and T. S. Fisher, “Mechanically robust honeycomb graphene aerogel multifunctional polymer composites,” *Carbon N. Y.*, vol. 93, pp. 659–670, 2015.

[284] S. K. Reddy, D. B. Ferry, and A. Misra, “Highly compressible behavior of polymer mediated three-dimensional network of graphene foam,” *RSC Adv.*, vol. 4, no. 91, pp. 50074–50080, 2014.

[285] H. Li *et al.*, “Engineering of High-Density Thin-Layer Graphite Foam-Based Composite Architectures with Superior Compressibility and Excellent Electromagnetic Interference Shielding Performance,” *ACS Appl. Mater. Interfaces*, vol. 10, no. 48, pp. 41707–41716, 2018.

[286] Y. H. Zhao, Y. F. Zhang, and S. L. Bai, “High thermal conductivity of flexible polymer composites due to synergistic effect of multilayer graphene flakes and graphene foam,” *Compos. Part A Appl. Sci. Manuf.*, vol. 85, pp. 148–155, 2016.

[287] J. Bustillos, C. Zhang, B. Boesl, and A. Agarwal, “Three-Dimensional Graphene Foam-Polymer Composite with Superior Deicing Efficiency and Strength,” *ACS Appl. Mater. Interfaces*, vol. 10, no. 5, pp. 5022–5029, 2018.

[288] Y. S. Jun *et al.*, “Highly conductive interconnected graphene foam based polymer composite,” *Carbon N. Y.*, vol. 95, pp. 653–658, 2015.

[289] Y. Yu *et al.*, “Three-dimensional compressible and stretchable conductive composites,” *Adv. Mater.*, vol. 26, no. 5, pp. 810–815, 2014.

[290] Z. Chen, C. Xu, C. Ma, W. Ren, and H. M. Cheng, “Lightweight and flexible graphene foam composites for high-performance electromagnetic interference shielding,” *Adv. Mater.*, vol. 25, no. 9, pp. 1296–1300, 2013.

[291] M. Chen, L. Zhang, S. Duan, S. Jing, H. Jiang, and C. Li, “Highly stretchable conductors integrated with a conductive carbon nanotube/graphene network and 3D porous poly (dimethylsiloxane),” *Adv. Funct. Mater.*, vol. 24, no. 47, pp. 7548–7556, 2014.

[292] C. Zhang, W. W. Tjiu, W. Fan, S. Huang, and T. Liu, “A novel approach for transferring water-dispersible graphene nanosheets into organic media,” *J. Mater. Chem.*, vol. 22, no. 23, pp. 11748–11754, 2012.

[293] C. Zhang, L. Ren, X. Wang, and T. Liu, “Graphene oxide-assisted dispersion of pristine multiwalled carbon nanotubes in aqueous media,” *J. Phys. Chem. C*, vol. 114, no. 26, pp. 11435–11440, 2010.

[294] D. Bodas and C. Khan-Malek, “Formation of more stable hydrophilic surfaces of PDMS by plasma and chemical treatments,” *Microelectron. Eng.*, vol. 83, no. 4-9 SPEC. ISS., pp. 1277–1279, 2006.

[295] I. Wong and C. M. Ho, “Surface molecular property modifications for poly(dimethylsiloxane) (PDMS) based microfluidic devices,” *Microfluid. Nanofluidics*, vol. 7, no. 3, pp. 291–306, 2009.

[296] J. Zhou, A. V. Ellis, and N. H. Voelcker, “Recent developments in PDMS surface modification for microfluidic devices.,” *Electrophoresis*, vol. 31, no. 1, pp. 2–16, 2010.

[297] C. Howell *et al.*, “Self-Replenishing Vascularized Fouling-Release Surfaces,” *ACS Appl. Mater. Interfaces*, vol. 6, pp. 13299–13307, 2014.

[298] M. J. Owen and P. J. Smith, “Plasma treatment of polydimethylsiloxane,” *J. Adhes. Sci. Technol.*, vol. 8, no. 10, pp. 1063–1075, 1994.

[299] T. Murakami, S. ichi Kuroda, and Z. Osawa, “Dynamics of polymeric solid surfaces treated with oxygen plasma: Effect of aging media after plasma treatment,” *J. Colloid Interface Sci.*, vol. 202, no. 1, pp. 37–44, 1998.

[300] D. T. Eddington, J. P. Puccinelli, and D. J. Beebe, “Thermal aging and reduced hydrophobic recovery of polydimethylsiloxane,” *Sensors Actuators, B Chem.*, vol. 114, no. 1, pp. 170–172, 2006.

[301] H. Makamba, Y. Y. Hsieh, W. C. Sung, and S. H. Chen, “Stable permanently hydrophilic protein-resistant thin-film coatings on poly(dimethylsiloxane) substrates by electrostatic self-assembly and chemical cross-linking,” *Anal. Chem.*, vol. 77, no. 13, pp. 3971–3978, 2005.

[302] F. Poncin-Epaillard, B. Chevet, and J.-C. Brosse, “Modification of isotactic poly(propylene) with a nitrogen plasma; differences in comparison to the treatment with a carbon dioxide plasma,” *Die Makromol. Chemie*, vol. 192, no. 7, pp. 1589–1599, 1991.

[303] M. P. Wolf, G. B. Salieb-Beugelaar, and P. Hunziker, “PDMS with designer functionalities—Properties, modifications strategies, and applications,” *Prog. Polym. Sci.*, vol. 83, pp. 97–134, 2018.

[304] S. Lee and J. Vörös, “An aqueous-based surface modification of poly(dimethylsiloxane) with poly(ethylene glycol) to prevent biofouling,” *Langmuir*, vol. 21, no. 25, pp. 11957–11962, 2005.

[305] J. S. Chen, Y. S. Ting, H. M. Tsou, and T. Y. Liu, “Highly hydrophilic and antibiofouling surface of zwitterionic polymer immobilized on polydimethylsiloxane by initiator-free atmospheric plasma-induced polymerization,” *Surf. Coatings Technol.*, vol. 344, no. 2017, pp. 621–625, 2018.

[306] B. L. Leigh, E. Cheng, L. Xu, A. Derk, M. R. Hansen, and C. A. Guymon, “Antifouling Photograftable Zwitterionic Coatings on PDMS Substrates,” *Langmuir*, vol. 35, no. 5, pp. 1100–1110, 2019.

[307] S. B. Yeh, C. S. Chen, W. Y. Chen, and C. J. Huang, “Modification of silicone elastomer with zwitterionic silane for durable antifouling properties,” *Langmuir*, vol. 30, no. 38, pp. 11386–11393, 2014.

[308] Q. Tu *et al.*, “Antifouling properties of poly(dimethylsiloxane) surfaces modified with quaternized poly(dimethylaminoethyl methacrylate),” *Colloids Surfaces B Biointerfaces*, vol. 102, pp. 361–370, 2013.

[309] Y. Hu, B. Ma, Y. Zhang, and M. Wang, “Small molecule - Folic acid modification on nanopatterned PDMS and investigation on its surface property,” *Biomed. Microdevices*, vol. 16, no. 3, pp. 487–497, 2014.

[310] M. Morales-Hurtado, X. Zeng, P. Gonzalez-Rodriguez, J. E. Ten Elshof, and E. van der Heide, “A new water absorbable mechanical Epidermal skin equivalent: The combination of hydrophobic PDMS and hydrophilic PVA hydrogel,” *J. Mech. Behav. Biomed. Mater.*, vol. 46, pp. 305–317, 2015.

[311] M. Gilges, M. H. Kleemiss, and G. Schomburg, “Capillary Zone Electrophoresis Separations of Basic and Acidic Proteins Using Poly(vinyl alcohol) Coatings in Fused Silica Capillaries,” *Anal. Chem.*, vol. 66, no. 13, pp. 2038–2046, 1994.

[312] M. Kozlov, M. Quarmyne, W. Chen, and T. J. McCarthy, “Adsorption of poly(vinyl alcohol) onto hydrophobic substrates. A general approach for hydrophilizing and chemically activating surfaces,” *Macromolecules*, vol. 36, no. 16, pp. 6054–6059, 2003.

[313] D. A. Barrett, M. S. Hartshorne, M. A. Hussain, P. N. Shaw, and M. C. Davies, “Resistance to nonspecific protein adsorption by poly(vinyl alcohol) thin films adsorbed to a poly(styrene) support matrix studied using surface plasmon resonance,” *Anal. Chem.*, vol. 73, no. 21, pp. 5232–5239, 2001.

[314] D. Wu, Y. Luo, X. Zhou, Z. Dai, and B. Lin, “Multilayer poly(vinyl acohol)-adsorbed coating on poly(dimethylsiloxane) microfluidic chips for biopolymer separation,” *Electrophoresis*, vol. 26, no. 1, pp. 211–218, 2005.

[315] T. Zhou *et al.*, “Hydrophilic Sponges for Leaf-Inspired Continuous Pumping of Liquids,” *Adv. Sci.*, vol. 4, no. 6, 2017.

[316] C. Finnerty, L. Zhang, D. L. Sedlak, K. L. Nelson, and B. Mi, “Synthetic Graphene Oxide Leaf for Solar Desalination with Zero Liquid Discharge,” *Environ. Sci. Technol.*, vol. 51, no. 20, pp. 11701–11709, 2017.

[317] G. N. Tiwari, H. N. Singh, and R. Tripathi, “Present status of solar distillation,” *Sol. Energy*, vol. 75, no. 5, pp. 367–373, 2003.

[318] Y. H. Zurigat and M. K. Abu-Arabi, “Modelling and performance analysis of a regenerative solar desalination unit,” *Appl. Therm. Eng.*, vol. 24, no. 7, pp. 1061–1072, 2004.

[319] M. K. Phadatare and S. K. Verma, “Influence of water depth on internal heat and mass transfer in a plastic solar still,” *Desalination*, vol. 217, no. 1–3, pp. 267–275, 2007.

[320] R. Tripathi and G. N. Tiwari, “DESALINATION Effect of water depth on intemal heat and mass transfer for active solar distillation,” *Desalination*, vol. 173, pp. 187–200, 2005.

[321] J. W. Cary, “An evaporation experiment and its irreversible thermodynamics,” *Int. J. Heat Mass Transf.*, vol. 7, no. 5, pp. 531–538, 1964.

[322] A. V. Lykov, “Application of the Methods of Thermodynamics of Irreversible Processes to Investigation of the Heat and Mass Transfer,” *Inzhenerno Fiz. Zhurnal*, pp. 287–304, 1965.

[323] S. R. De Groot, “On the thermodynamics of irreversible heat and mass transfer,” *Int. J. Heat Mass Transf.*, vol. 4, no. C, pp. 63–70, 1961.

[324] G. Nagayama, M. Kawagoe, A. Tokunaga, and T. Tsuruta, “On the evaporation rate of ultra-thin liquid film at the nanostructured surface: A molecular dynamics study,” *Int. J. Therm. Sci.*, vol. 49, no. 1, pp. 59–66, 2010.

[325] H. R. Seyf and Y. Zhang, “Effect of nanotextured array of conical features on explosive boiling over a flat substrate: A nonequilibrium molecular dynamics study,” *Int. J. Heat Mass Transf.*, vol. 66, pp. 613–624, 2013.

[326] F. P. Incropera, D. P. Dewitt, T. L. Bergman, and A. S. Lavine, *Fundamentals of Heat and Mass Transfer*, 6th ed. Hoboken: John Wiley & Sons, Inc., 2007.

[327] L. Zhang, B. Tang, J. Wu, R. Li, and P. Wang, "Hydrophobic Light-to-Heat Conversion Membranes with Self-Healing Ability for Interfacial Solar Heating," *Adv. Mater.*, vol. 27, no. 33, pp. 4889–4894, 2015.

[328] G. Xue *et al.*, "Robust and Low-Cost Flame-Treated Wood for High-Performance Solar Steam Generation," *ACS Appl. Mater. Interfaces*, vol. 9, no. 17, pp. 15052–15057, 2017.

[329] V. Kashyap, A. Al-Bayati, S. M. Sajadi, P. Irajizad, S. H. Wang, and H. Ghasemi, "Flexible Anti-Clogging Graphite Film for Scalable Solar Desalination by Heat Localization," *J. Mater. Chem. A*, pp. 15227–15234, 2017.

[330] The Dow Chemical Company, "SYLGARD 184 Silicone Elastomer Technical Data Sheet," 2017. [Online]. Available: https://consumer.dow.com/content/dam/dcc/documents/en-us/productdatasheet/11/11-31/11-3184-sylgard-184-elastomer.pdf?iframe=true.

[331] M. Antunes and J. I. Velasco, "Multifunctional polymer foams with carbon nanoparticles," *Prog. Polym. Sci.*, vol. 39, no. 3, pp. 486–509, 2014.

[332] K. Zeranska-Chudek *et al.*, "Study of the absorption coefficient of graphene-polymer composites," *Sci. Rep.*, vol. 8, no. 1, pp. 1–8, 2018.

[333] N. E. Stankova *et al.*, "Optical properties of polydimethylsiloxane (PDMS) during nanosecond laser processing," *Appl. Surf. Sci.*, vol. 374, pp. 96–103, 2016.

[334] J. C. McDonald and G. M. Whitesides, "Poly(dimethylsiloxane) as a material for fabricating microfluidic devices," *Acc. Chem. Res.*, vol. 35, no. 7, pp. 491–499, 2002.

[335] D. K. Cai, A. Neyer, R. Kuckuk, and H. M. Heise, “Optical absorption in transparent PDMS materials applied for multimode waveguides fabrication,” *Opt. Mater. (Amst).*, vol. 30, no. 7, pp. 1157–1161, 2008.

[336] D. K. Cai, A. Neyer, R. Kuckuk, and H. M. Heise, “Estimation of absorption loss in siloxane-based materials implemented as passive optical interconnects,” *OFC/NFOEC 2007 - Opt. Fiber Commun. Natl. Fiber Opt. Eng. Conf. 2007*, pp. 5–7, 2007.

[337] X. Tan, M. Li, P. Cai, L. Luo, and X. Zou, “An amperometric cholesterol biosensor based on multiwalled carbon nanotubes and organically modified sol-gel/chitosan hybrid composite film,” *Anal. Biochem.*, vol. 337, no. 1, pp. 111–120, 2005.

[338] W. Liu, M. S. Song, B. Kong, and Y. Cui, “Flexible and Stretchable Energy Storage: Recent Advances and Future Perspectives,” *Adv. Mater.*, vol. 29, no. 1, 2017.

[339] M. Morra, E. Occhiello, R. Marola, F. Garbassi, P. Humphrey, and D. Johnson, “On the aging of oxygen plasma-treated polydimethylsiloxane surfaces,” *J. Colloid Interface Sci.*, vol. 137, no. 1, pp. 11–24, 1990.

[340] Z. Shi, Y. Zhang, M. Liu, D. A. H. Hanaor, and Y. Gan, “Dynamic contact angle hysteresis in liquid bridges,” *Colloids Surfaces A Physicochem. Eng. Asp.*, vol. 555, no. June, pp. 365–371, 2018.

[341] U.S. Energy Information Administration, “Enegy Units and Calculators Explained,” 2019. [Online]. Available: https://www.eia.gov/energyexplained/index.php?page=about_btu.

Appendices

Appendix A: Fitting of the UV/Vis/NIR measurement

Due to the systematic design of the Lambda 1050 UV/Vis/NIR spectrophotometer, two detectors, namely the Photomultiplier R6872 (PMT) and a wide band InGaAs detector, are employed to separately measure over the UV-visible and near infrared range. During the measurement, switching detectors created an artifact in the measured signal, which was apparent in the measurement over an extended spectral region from about 825 nm to 1050 nm. In this study this defect is treated using a fitting method. The comparison of the transmittance spectrum of PVA-treated sample 8 (PVA-5CNP/PDMS-2) before and after fitting is shown in Figure 1 as an example. The affected region is removed, and the resultant interval is extrapolated by a linear fitting using 50 data from both ends (data within the green circles).

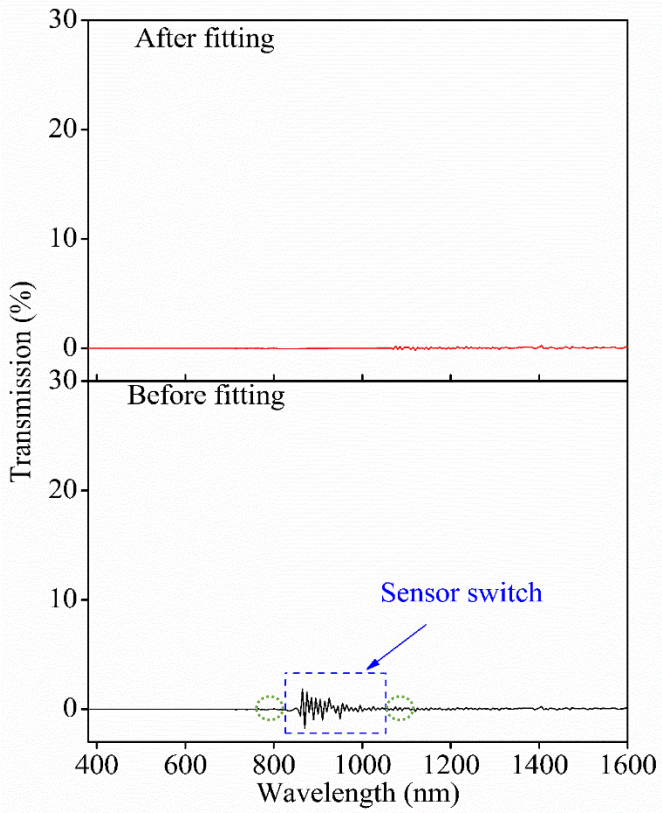

Figure 1 Fitting of the transmittance spectrum of sample 8 (PVA-5CNP/PDMS-2).